Manipulation of Light *via* Subwavelength Nanostructures

Gu Yinghong

(*B. Sci., Fudan Univ., China*)

A THESIS SUBMITTED FOR THE DEGREE OF

DOCTOR OF PHILOSOPHY

DEPARTMENT OF ELECTRICAL AND COMPUTER ENGINEERING

NATIONAL UNIVERSITY OF SINGAPORE

2015

Declaration

I hereby declare that this thesis is my original work and it has been written by me in its entirety. I have duly acknowledged all the sources of information which have been used in the thesis.

This thesis has also not been submitted for any degree in any university previously.

Gu Yinghong

24/12/2015

Acknowledgements

It is my great pleasure to express my sincere appreciation to all those who have guided, advised and helped me during the period of my Ph.D. study. First and foremost, I would like to show my deepest gratitude to my supervisor, Prof. Qiu Cheng Wei, for his enlightening guidance, persistent support and kindest encouragement. His talent and enthusiasm in research gave me confidence and motivation to persist working hard and broadening my mind. Without his great help and contribution this dissertation would not have been possible.

I would like to thank my co-supervisors, Prof. Joel Yang and Prof. Yeo Swee Ping, for their constant support and guidance. Particularly, Prof. Yang has provided me a great many valuable ideas and suggestions, inspiring me to explore new research areas and assisting me to improve my research skills. I am grateful for their indispensable contribution in my research work.

In addition, I also like to thank my colleagues and cooperators from NUS and IMRE. Sincere thanks goes to Dr. Dong Zhaogang, Wang Zhuo and Wang Dacheng, who have bring most advanced experimental resources and done excellently in fabrication and measurement, their outstanding experimental works promoted the academic and practical value of our research; also to Dr. Zhang Lei and Dr. Qin Fei, who gave me precious advising and revised my papers, they have helped me solve numerous problems in technical details. Besides the direct cooperators I mentioned above, I am also grateful to Dr. Huang Kun, Prof. Han Tiancheng, Prof. Ding Weiqiang, Dr. Gao Dongliang, Dr. Ye Huapeng, Dr. Muhammad Qasim Mehmood, Mei Shengtao, Dr. Karthik Kumar and Prof.

Duan Huigao. In many aspects, they have patiently discussed with me and I learnt quite a lot from them. Furthermore, I sincerely appreciate our precious friendship and unforgettable memory together.

Last but not least, I would like to thank my beloved parents for their constant encouragement, selfless support and irreplaceable love throughout my lifetime. It is their love supports me overcome all the difficulties.

Table of Contents

Summary

Subwavelength nanostructures have exhibited different and controllable optical characteristics from their original material, leading a way to artificial metamaterials and metasurfaces. These nanostructures interact with light with surface plasmon resonances, cavity and waveguide modes, scattering and diffractions and etc., so they can realize the manipulation of light, which has attracted enduring and fanatic research interest, ranging from visible light, infrared light, THz to microwaves. Nanostructures, which are well-designed and patterned to control and engineer the resonances, have realized and improved the performance of numerous optical applications such as color printing, perfect absorption, waveplates, planar lens, holograms, cloaking, optical trapping and sensing.

This thesis has presents several works on manipulating light with subwavelength nanostructures, which can be generalized into two main parts. In the first part our works are manipulating far-field characteristics of light by meta-surfaces, including the high resolution color printing and imaging with spectra manipulation, and quarter wave plate (QWP) with the phase and polarization manipulation. For the color generation applications, we have presented a comprehensive literature review on the recent developments of plasmonic colors, and then we reported our ultra-high resolution non-plasmonic color printing with ultra-narrow Si fin nanostructures and an efficient TMM calculation. For the quarter wave plate, we present a series works of plasmonic QWPs

including active hybrid QWPs working at multi-wavelength in visible/near-infrared light, and in THz range based on similar mechanism.

The other main part is the near-field manipulation of light by nanostructures including two aspects. One is the direct excited dark modes, and the other is the photoluminescence (PL) enhancement by nanostructures. We have proposed a new mechanism to directly excite dark modes by using an electrical shorting approach with a continuous metal cover on a periodic HSQ pillar template without any asymmetry in geometry, environment and incidence. And we will also present a cooperative work on giant PL enhancement of WSe_2-Au plasmonic hybrid nanostructures. In simulation, we have explained how a squared trenched Au nanostructure with gap plasmon enhances the PL of monolayer WSe_2 on top of it, in both excitation process and emission process.

List of Figures

List of Symbols

Alphabet and Greek Symbols

λ	Wavelength of operating light in free space
k	The wavenumber
ω	The angular frequency
c	The speed of light in vacuum
α	Polarizability
ε	Permittivity
χ	Geometrical factor
φ	Polarization angle

Acronyms

AAA	Annular Aperture Array
Ag	Silver
Al	Aluminum
ALD	Atomic Layer Deposition
Au	Gold
CST	Computer Simulation Technology
CVD	Chemical Vapour Deposition
d.p.i	dots per inch
EBL	Electron-Beam Lithography
EELS	Electron Energy Loss Spectroscopy
EF	Enhancement Factor

EMW	Electromagnetic wave
EOT	Extraordinary Optical Transmission
FDTD	Finite-Difference Time-Domain
FIB	Focused Ion Beam
GSP	Gap Surface Plasmon
GST	$Ge_2Sb_2Te_5$
HSQ	Hydrogen Silsesquioxane
LC	Liquid Crystal
LCP	Left-hand Circular Polarization
LSPR	Localized Surface Plasmon Resonance
MMQWP	Metasurface-based Multi-wavelength Quarter Wave Plate
MoS_2	Molybdenum Disulfide
$MoSe_2$	Molybdenum Diselenide
PCM	Phase-Change Material
PEC	Perfect Electric Conductor
PEN	Polyethylene Naphthalate
PL	Photoluminescence
QWP	Quarter Wave Plate
RCP	Right-hand Circular Polarization
SEM	Scanning Electron Micrograph
Si	Silicon
SP	Surface Plasmon
SPP	Surface Plasmon Polariton
SPR	Surface Plasmon Resonance
TE	Transverse Electric

THz	Terahertz
TM	Transverse Magnetic
TMDC	Transition Metal Dichalcogenide
TMM	Transfer-Matrix Method
UV	Ultraviolet
VO_2	Vanadium Dioxide
WSe_2	Tungsten Diselenide
1D	One Dimensional
2D	Two Dimensional
3D	Three Dimensional

Chapter 1 Introduction

The interaction between light and matters has attracted enduring and fanatic research interest. With the development of nanotechnology in recent few years, the researches concentrate on manipulating light by well-designed subwavelength structures, to be more specific, by ultrathin patterned or layered nanostructures, so-called meta-surfaces. An electromagnetic meta-surface refers to a kind of artificial sheet material with subwavelength thickness and electromagnetic properties on demand. These meta-surfaces interact with light with surface plasmon resonances, cavity and waveguide modes, scattering and diffractions and etc. Unlike conventional optical components, meta-surfaces don't need to gradually accumulate changes of the amplitude, phase or polarization of electromagnetic waves (EMWs) along the optical path, they can produce abrupt changes in amplitude, phase or polarization by all kinds of resonances within subwavelength spatial dimensions. The mechanism of controlling EMWs by meta-surfaces is to eningeer the resonances on the nanostructures excited by EMWs from visible light to microwave. These modulations of amplitude, phase, polarization and local fields are realized by well-designed geometry and size of subwavelength artificial structures. In recent researches, meta-surfaces are widely used in negative index [1-4], ultra-high resolution color printing [5-20], planar lens [1, 21], wave plates [22-28], holograms [29], invisibility cloaking [30, 31], perfect absorption [32-37], chiral manipulation [38-45], amplitude and phase modulation [29, 46-54] etc.

To manipulate light by artificial subwavelength structures, this thesis will investigate the methods and applications of engineering resonances to control the interaction between light and structures, and further control the intensity, phase and polarization of output light in far-field and the local effects and field distribution around the structures. The overall contribution of this thesis is to introduce different novel ways of engineering resonances on nanostructures to realize applications in different terms. Basically we divide our researches into far field applications and near field applications and investigations. For far field applications, current research hot spots can be concluded into three main areas: 1) manipulating the transmitted/reflected spectra of light by meta-surfaces, especially in visible light range, which means color filters or printings with plasmonic and non-plasmonic nanostructures; 2) manipulating the polarization and relative phase shift of EMWs by meta-surfaces, for instance, plasmonic wave plates; and 3) generating specific kinds of beams [53, 55, 56] and holographic patterns [57-61] by meta-surfaces. Our research works includes the first two areas, which will be presented in Chapter 2 and Chapter 3 of this thesis respectively. In Chapter 2, we investigate color printing and imaging based on manipulation of reflective and transmissive intensity by resonances. To compare the manipulation of light by plasmonic resonances (free electron oscilations) and non-plasmonic resonances (electicmagnetic field oscilations of waveguides, cavities and scatterers) of nanostructures, we have presented a comprehensive literature review on the recent developments of plasmonic color printing, and then we reported our non-plasmonic color printing with Si nanostructures and an efficient TMM calculation. And in Chapter 3, we investigate plasmonic quarter wave plate based on manipulation of the relative phase difference between different polarizations by plasmonic resonances. To be specific, we present a design of actively switchable plasmonic quarter wave plate working at multi-wavelength in visible and near-infrared light, which is hybrid meta-surface with a spacing layer of phase change material GST. In addition, we have also reported two cooperative works on plasmonic quarter wave plates in THz range, based on similar mechanism. Moverover, the active control of plasmonic resonances of hybrid nanostructures could further contribute to optical applications other than quarter wave plates.

The other main part is the local-field manipulation of light by nanostructure resonances. As well as the fantastic far-field functionalities realized by subwavelength structures, researchers are also deeply interested in the diversity of the resonance modes on the subwavelength structures, especially plasmonic resonance modes. Specific resonant behaviors like dark modes [62-66], Fano resonances [67, 68], gap plasmons [69-72] and dielectric magnetic modes [73-77] have been deeply investigated, and their giant potential in optical applications is revealed. Generally, these resonance modes have their characteristic local electric or magnetic field distribution, which would be utilized in photoluminescence (PL) [70, 78-80], sensing [81-84], optical tweezers and trapping [85-87] and other biological applications. These local field researches also relay on the engineering of resonances on nanostructures, which will be discussed in this thesis as well. In Chapter 4, we have proposed a new mechanism to directly excite dark modes by using an electrical shorting approach with a continuous metal cover on a periodic HSQ pillar template. The key point of the research is to induce and engineer the dark plasmonic resonances on continuous metal structure without any asymmetry in geometry, environment and incidence. Another research on engineering plasmonic resonance to influence local field and other materials is a cooperative work on giant PL enhancement of WSe_2-Au plasmonic hybrid nanostructures, which is reported in Chapter 5. In simulation, we have revealed how a squared trenched Au nanostructure with gap plasmon resonances enhances the PL of monolayer WSe_2 on top of it. The enhancement was generated in both excitation process by strong local electric field of plasmonic resonances and emission process by large Purcell effects.

Overall, our research works in the following chapters concertrate on manipulation of light *via* subwavelength nanstructures, with both plasmonic and non-plasmonic resonances, and targeting on different kinds of applications. Although the manipulation of light in our works is quite different in form, the critical point is to engineer the resonance by well-designed nanostructures, which results in controlling of resonance modes, local field and far-field optical characteristics. We have shown the outstanding ability and great potential of nanostructures to manipulate and control light in optical applications. And our works can contribute to optical and photonic research by controlling the intensity, phase and polarization of light, and investigating the local fields and resonance modes of the nanostructures.

Chapter 2 Manipulating Light Intensity Spectra by Meta-Surface

2.1 Introduction: color generation via meta-surface

As we claimed in the introduction, by well-designed resonances of subwavelength nanostructural unit cells and their planar periodic array as a meta-surface, we can therefore manipulate the transmittive and reflective intensity spectra of these ultra-thin surficial nanostructure patterns. To be specific, we concentrate on the resonances within the wavelength range of visible light (with wavelength from 400 to 750nm), so that the transmitted or reflected light could be observed directly by human eyes and colors are generated by the meta-surfaces. For human eyes, colors are the visual perceptual property derived from the spectrum of light interacting in the eye with the spectral sensitivities of the light receptors (three retinal cone photoreceptors of red, green and blue). Therefore, by engineering resonance wavelength of meta-surfaces and thus manipulating the light intensity spectra, colors can be generated.

In nature, colors are mainly produced by objects or materials based on their physical properties such as light absorption, reflection, transmission or emission spectra. Color related technologies such as emissive liquid-crystal displays employ pigment-based color filters to absorb the complementary colors to produce the red, green, and blue channels [88, 89]. The highest possible spatial resolution in theory for color printing and imaging is set by the diffraction limit of the accompanying optics [90], which is ~250-nm-pitch for imaging through high numerical-aperture objectives with visible light. However, the highest spatial resolution of existing industrial techniques for color printing cannot reach 10,000 dots per inch (d.p.i) yet, with the pixel size at the level of ten micrometers, still 1 or 2 orders away from diffraction limit.

Recent developments in color filtering and printing technologies focus predominantly on high spatial resolution, color vibrancy, high efficiency, and slim dimensions. Conventional pigment-based color filters encounter more and more difficulties in satisfying these gradually increasing requirements. Especially with the drive towards higher-resolution imaging and displays, new innovations are needed to achieve higher spatial resolution, lower power consumption, higher compactness, and also color tunability in devices. Meta-surfaces with subwavelength nanostructures, either plasmonic or non-plasmonic, are promising to overcome those difficulties due to their ultra-small dimensions and the ability to efficiently manipulate light [13, 16, 19]. Thickness of meta-surfaces for visible light is usually around 100nm or even less, which can greatly improve the compactness of devices. The spatial resolution of both plasmonic and non-plasmonic color nano-printing can be larger than 100,000 d.p.i, which is already beyond the optical diffraction limit. In addition, these meta-surfaces have wide color tunability and robustness to high temperature and ultraviolet radiation exposure. Separately, we will comprehensively review the recent developments of plasmonic color nano-printing research in section 2.2, and report our non-plasmonic color nano-printing based on silicon nano-fins in section 2.3

2.2 Color generation via plasmonic meta-surface

Surface plasmons (SPs) are collective free-electron oscillations at metal-dielectric interfaces. They exhibit enhanced near-field amplitude of electric field at the resonance wavelength. This field is highly localized and decays exponentially away from the metal/dielectric interface [90-94]. Unlike photon absorption in pigments, which is determined by the energy level transitions of the molecules, the scattering and absorption of plasmonic nanostructures are determined by their geometry and dimensions. Leveraging on the development of nanofabrication technologies such as electron-beam lithography (EBL) and focused ion beam (FIB), the shape and size of metallic nanostructures can be well-controlled with sub-10-nm precision [95, 96]. With these subwavelength elements, the pixels of color imaging can be extremely small and the spatial resolution can be improved up to the diffraction limit, with thickness of resonators of only tens of nanometers, so that they can be regarded as elements of meta-surfaces. In addition to the advantage of high spatial resolution and ultrathin characteristics, plasmonic meta-surfaces have also the following attributes: (1) as the nanostructures are made of metal, they are chemically stable and can endure long-duration ultraviolet irradiation and high temperature compared to chemical pigments; (2) the device can realize a broad range of colors using a single element of metal, by just varying the lateral size and geometry of structures. This avoids the sequential deposition of inks, reduces process steps, and misalignment between color channels; (3) the surface plasmon resonances (SPRs) can be tuned by factors such as environment index, incident angle and polarization, it is possible to make the optical element active [5, 6, 9, 97-99] which could be useful for dense optical data archival [100], and contributes to security applications.

Here we will provide an overview of the most recent development of color generating via plasmonic meta-surfaces. In terms of mechanisms, we have concluded them into three types: 1) color generated by localized surface plasmon resonances (LSPRs); 2) color generated by propagating surface plasmon polaritons (SPPs); 3) color generated by coupling of localized and propagating surface plasmons. We will introduce them in following sections respectively.

2.2.1 Color generation via LSPRs

LSPRs are collective electron charge oscillations in plasmonic nanoparticles that are excited by light, and well-designed plasmonic nanoparticles can be viewed as optical nanoantennas that receive optical radiation from the far field to the near field at specific frequencies and vice versa. Due to the geometry- and dimension-dependence, the LSPRs of these nanoantennas can be manipulated to achieve desirable reflection and transmission spectra [5, 12, 98, 101], and further generate the imaging pattern with pre-designed plasmonic structures [29, 102]. Considering a simplified model of an array of identical metallic nanoparticles, which are typical plasmonic resonators, with a dipole of polarizability α for each nanoparticle, the LSPR can be estimated by the coupling dipole theory [103]. When the resonator is excited, it will radiate a scattering field in proportion to its dipole moment. The static polarizability of each resonator can be written as [104]

$$\alpha^{\text{static}} = V \frac{\varepsilon_m - \varepsilon_d}{\varepsilon_{\text{d}} + \chi\left(\varepsilon_m - \varepsilon_d\right)} \tag{2.1}$$

where ε_m and ε_d are the relative permittivities of metal and surrounding environment, respectively; χ is the geometrical factor along the dipole direction relating to the physical shape of resonator and V is the volume of resonator. When the resonator is a sphere, χ = 1/3 for every direction. If the size of resonator is large enough (radius a is of order 50nm or more) to consider the dynamic depolarization and radiative damping, we need to modify the polarizability by:

$$\alpha = \frac{\alpha^{\text{static}}}{1 - \frac{2}{3} i k^3 \alpha^{\text{static}} - \frac{k^2}{a} \alpha^{\text{static}}} \tag{2.2}$$

Assuming the whole array is infinite, the effective polarizability α* of the LSPR on single dipole resonator can be generally expressed as

$$\alpha^* = \frac{1}{\frac{1}{\alpha} - S} \tag{2.3}$$

where the array factor S for the square array with normal incidence can be written as

$$S = \sum_{dipoles} e^{ikr} \left[\frac{(1 - ikr)\left(3\cos^2\theta - 1\right)}{r^3} + \frac{\mathrm{k}^2 \sin^2\theta}{r} \right] \tag{2.4}$$

θ and r denote the position of dipole resonators. From eqn. (2.3), when the absolute value of S-1/α is minimized, the effective polarizability would be maximized, leading to a resonance of the dipole array with strong scattering. Regarding this planar array of plasmonic resonators as a meta-surface, the wave scattering backward at resonance could result in a reflected peak and a transmitted dip correspondingly.

Although these collective plasmonic resonances are also influenced by other factors such as the Wood's anomaly and Bloch wave surface plasmon polaritons [105-107], and all these factors are mutually coupled, these expressions can basically provide a good estimate to describe the LSPR of the resonator array. For instance, Jinghua Teng et al, had presented a reflective plasmonic color filters based on Ag nanorod arrays [12], which is typically generating color by meta-surface with LSPRs. In Fig 2-1, the dimensions and the periodicities of the Ag nanorods are designed to control the wavelength and intensity of LSPRs, so that they can control the resonance peaks in reflected spectra. To achieve abundant color band, especially the blue color in Fig 2-1 (b) and (c), small periodicity and very high diameter/periodicity ratio of the nanostructure is required, which means the gap between two nanorods needs to be ultrasmall. This requires high fabrication accuracy,

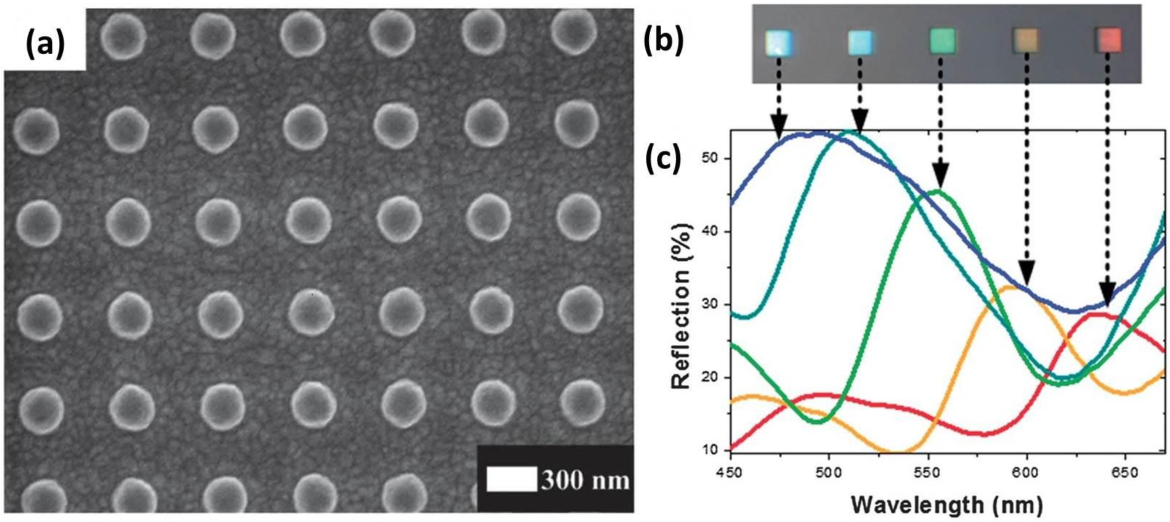

Fig 2-1 (a) Scanning electron microscope (SEM) image of the top view of a Ag vertical nanorods array on a quartz substrate with periodicity p=550 nm. (b) Optical image of the reflective colors from different Ag nanorod arrays. (c) Measured reflection spectra of the corresponding arrays as a function of wavelengths. Reproduced with permission [12]. Copyright 2013, RSC.

but on the other hand, provides high spatial resolution. The periodicity is close to the wavelength, so the color pixels are much smaller than those of conventional chemical pigment-based methods.

More generally, resonators with LSPRs can be manipulated by changing not only the dimensions of nanostructures, but also the shapes. For more complicated resonators, they should be considered as optical nanoantennas instead of simple nanoparticles. The break of geometry symmetry of these nanoantennas will lead to different responses to incident light with different polarization. In Fig 2-2, the polarization-dependent plasmonic meta-surface is reported by Crozier et al [5]. The resonators in unit cells are Al nano-crosses with different arm length. As shown in Fig 2-2 (a) and (b), either vertical or horizontal polarized incident light can only excite the LSPR of their corresponding arms, so that they have different transmission spectra and render different colors. At arbitrary polarization angle φ, the transmission spectra is a linear superposition of vertical and horizontal polarization states, represented as

$$\mathrm{T}\left(\varphi,\lambda\right)=T_V\left(\lambda\right)\sin^2\varphi+T_H\left(\lambda\right)\cos^2\varphi \tag{2.5}$$

where $T_V(\lambda)$ and $T_H(\lambda)$ are the transmittances for light polarized vertically and horizontally. In Fig 2-2 (b), for incident polarization along their short arms, the light with shorter wavelength is absorbed and the transmitted color is yellow; while for incident polarization along long arms, the light with longer wavelength is absorbed and the color is blue. With controlled position and rotating angle of these elements, it can achieve active polarized images. Fig 2-2 (c) (ii—v) shows a sample with different colors of the acronym “LSP” and background according to different incident polarization. Fig 2-2 (c) (vi—xi) shows another example that the cross nanoantennas are patterned with a rotating angle θ(x) =180^{o} x/L, where x is the spatial coordinate and L is the extent of the sample in the x direction. As the incident polarization angle varies, the transmitted color image along x direction is also gradually changed, moving like a wave.

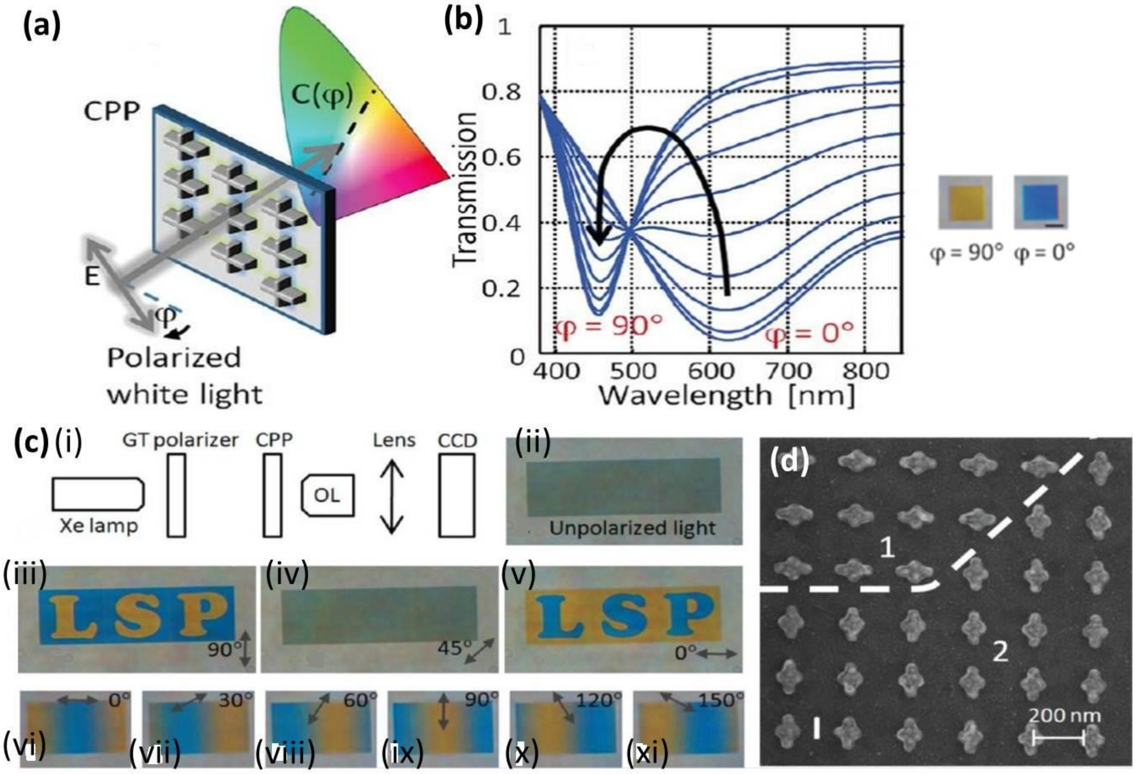

Fig 2-2 (a-c) Conversion of polarization state to visible color by cross nanoantennas: (a) Polarized white light is color filtered by the LSPs on the arms of the cross nanoantennas, the output color results from additive color mixing of the filtering functions of the two arms of the cross. (b) Simulated transmission spectra for linearly polarized illumination with polarization angles ranging from φ = 0°, at which yellow is blocked, to φ = 90°, at which blue is blocked, in steps of 10 °. (c (i)—(xi)) c (i) Schematic representation of experimental setup. c(ii)—(v) Transmission images of LSP pattern sample for (ii) unpolarized incident light, (iii) 90 °, (iv) 45 °and (v) 0 °polarized light. C (vi)—(xi) Transmission images of twisted sample for 0 °—90 °polarized light in steps of 30 °. (d) SEM image of part of LSP sample. (d) Schematic diagram of polarization dependent nanostructure with elliptical nano-pillars and coupled nano-square pair pillars with Al on top and at the bottom. (a)—(d) Reproduced with permission [5]. Copyright 2012, ACS.

Polarization dependent color filtering and imaging provides another degree of freedom to manipulate color information [5, 6], which is important and has potential applications in many fields. First of all, it can be applied to polarization- related measurements, such as birefringence measurements of cancerous tissues [108] and other bio-sensing applications. Secondly, it can improve data storage efficiency by having two different resonances for a single structure. The polarization dependence could at least double the information capacity by recording data in different polarization states. In addition, it can also be useful in security applications by patterned surfaces that have concealed messages that can be read out only through the right combination of polarizers.

As well as the nanoantenna arrays, the one-dimensional (1D) metallic gratings, periodic metal long rods array in one direction, are widely used as meta-surfaces in color filtering and imaging. The most significant advantage of 1D plasmonic grating color filter and image among the plasmonic nanostructures is their high efficiency (usually 60% to 90%), which is always an important parameter in practical applications. Another superiority is that gratings are usually highly wavelength selective and sensitive. For those grating nanostructures coupled with guided modes, the bandwidth of resonance can be very narrow (with FWHM of 30nm [109]), so that the filtered color can be pure. The spatial resolution of these 1D gratings can be also ultrahigh, closed to the diffraction limit [17, 20]. The period of grating can be minified to half wavelength, and when the length of grating is shortened to subwavelength, it evolves to the plasmonic nanoantenna arrays we mentioned above, or so-called two dimensional (2D) gratings. Furthermore, 1D grating is the polarization dependent. Only transverse magnetic (TM) waves (the electric field is perpendicular to the grating direction) can be filtered, while the transverse electric (TE) waves (the electric field is parallel to the grating direction) will be mostly reflected or transmitted. Therefore they are suitable to work for many polarization-related applications as discussed above.

2.2.2 Color generation via propagating surface plasmon

SPPs are EMWs travelling along a metal-dielectric interface. With normal incident light onto a flat metal film, SPPs cannot be excited because of the momentum conservation. However, when we pattern periodic structures on the film, like nano-holes and nanoantennas, they can provide the momentum and excite SPPs. With SPPs generated by nano-hole arrays, the transmittance of the metal film can be greatly enhanced, which is called the extraordinary optical transmission (EOT) effect. These kinds of meta-surfaces with EOT effect are good candidates for color generating.

Considering a single hole in a metallic film, the transmission efficiency should be proportional to $(r/\lambda)^4$, where λ is the incident wavelength and r is the radius of the hole [110, 111]. It means the transmission of subwavelength hole would be extremely low. However, the periodic metallic structures can provide the momentum for converting incident light into SPs, so that the hole array on the metal film can give rise to the EOT effect [112-114]. In the past few years, the hole arrays had been theoretically and experimentally [11, 115-125] studied in many aspects, such as the selective extraordinary transmission for color filtering. The wavelength of transmission peak λ_{max} depends on the periodicity and the constituent of the hole array. At normal incidence, for the square array:

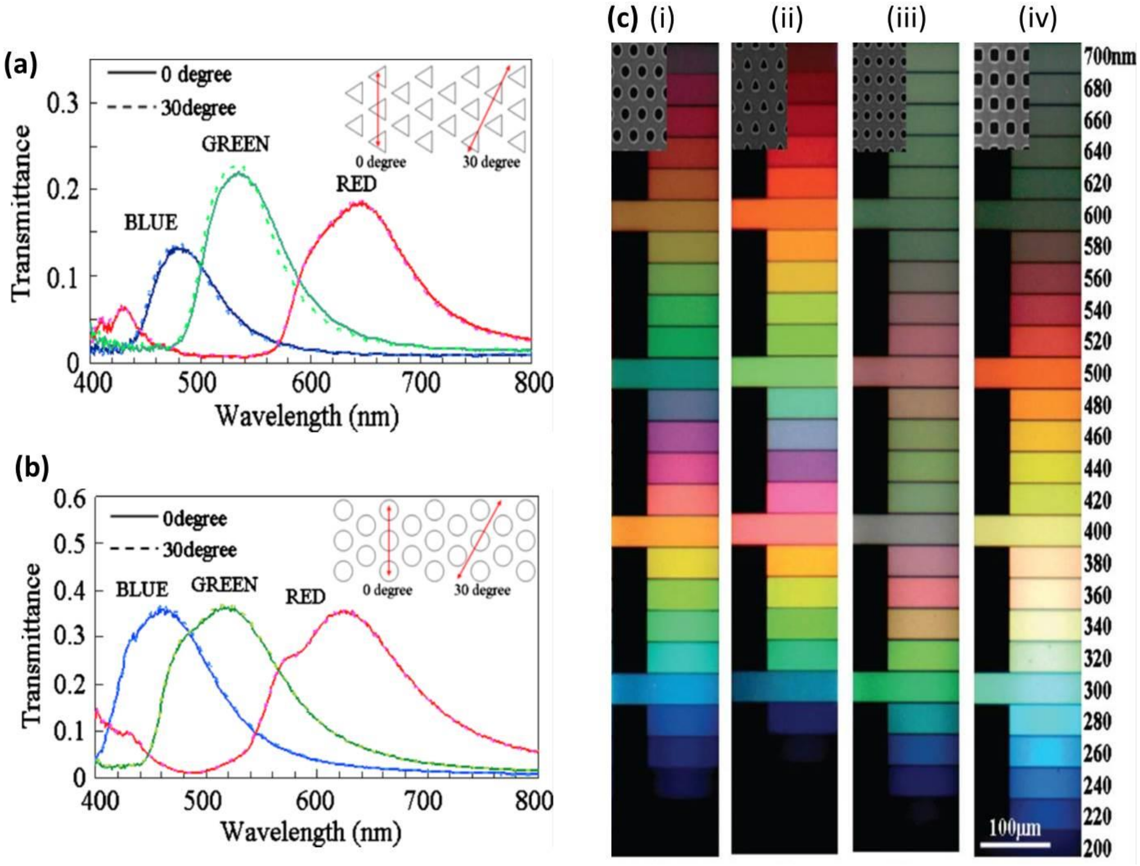

Fig 2-3 (a-b) Polarization dependence of the transmission spectra of RGB color filters with (a) triangular holes and (b) circular holes in hexagonal array. (c (i)—(iv)) Optical microscope images of Al color filters with (i) circular holes in hexagonal array, (ii) triangular holes, (iii) circular holes in square array, and (iv) square holes. (a)—(c) Reproduced with permission [126]. Copyright 2011, AIP Publishing LLC.

$$\lambda_{\max} = \frac{a}{\sqrt{i^2 + j^2}} \sqrt{\frac{\varepsilon_m \varepsilon_d}{\varepsilon_m + \varepsilon_d}} \tag{2.6}$$

And for the hexagonal array:

$$\lambda_{\max} = \frac{a}{\sqrt{\frac{4}{3}\left(i^2 + ij + j^2\right)}} \sqrt{\frac{\varepsilon_m \varepsilon_d}{\varepsilon_m + \varepsilon_d}} \tag{2.7}$$

where a is the periodicity of array, ε_m and ε_d are the relative permittivities of metal and dielectric material, and *i* and *j* are the scattering orders of the array [110, 127, 128].

Considering the interference of the scattering losses of the holes and the Fano-type interaction [107, 129], λ_{max} would be slightly blue shifted.

In particular, for the lowest order mode ($i = \pm 1$, $j = 0$), the SPR peak wavelength of hexagonal array is smaller than that of square array with the same period and material, according to eqn. (2.6) and eqn. (2.7). Moreover, the wavelength interval of transmission peak between the first two modes of hexagonal array is also larger, which makes hexagonal array more favorable to reduce the color cross-talk and improve the purity of color. On the other hand, the shape of holes also affects the transmitted color. As reported by Yasuo et al [126], they had compared the color generated by the nano-hole arrays on Al films with triangular holes in hexagonal array, circular holes in hexagonal array, triangular holes in square array and circular holes in square array. The spectra and colors are shown in Fig 2-3. The triangular hole arrays give narrower resonance peaks than the circular hole arrays, but with lower efficiency. After comparing, it is also found that lattice construction has larger influence on than hole shapes. Overall, the hexagonal array performs much better in building a full color map.

In experiments, the metallic film with hole array is usually fabricated on a glass or quartz substrate, which leads to an asymmetric dielectric environment. Therefore, two SP modes on both sides of the metal film are resonating at different wavelengths, as indicated in eqn. (2.6) and (2.7), which would reduce the color purity due to peaks overlapping. Owing to such asymmetry, momentum mismatch also results in an inefficient coupling between two sides and then a reduced transmittance. In order to deal with this, Cumming et al had employed an index-matching layer to coat the air side [127]. As shown in Fig 2-4, the transmittance was efficiently improved in the presence of SiO_2 layer in comparing with the case in the absence of SiO_2.

The refractive index of environment can be also utilized to modulate the transmitted spectra of these meta-surfaces. An active plasmonic color filter was reported by

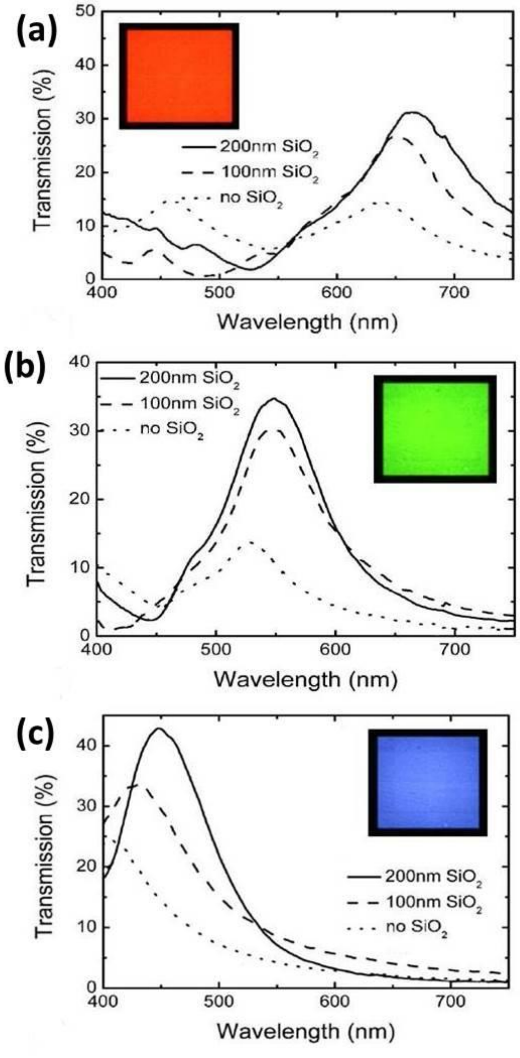

Fig 2-4 Measured transmission spectra of RGB color filters of circular hole array, with no cap layer, 100 nm and 200 nm SiO_2 cap layer for (a) red, (b) green and (c) blue color. The transmitted light image of the structure with a 200 nm SiO_2 cap layer is shown in the inset. (a)—(c) Reproduced with permission [127]. Copyright 2010, OSA.

overlaying photoresponsive liquid crystals (LCs) onto Au annular aperture arrays (AAAs) [99]. The photochromic LC molecules would change their form upon ultraviolet (UV) irradiation, and further generate a photo-induced refractive index modulation. With this refractive index modulation, the transmittance could be easily controlled by UV irradiation.

Overall, the nano-hole arrays on metal films, with their EOT effects, can provide a variety of colors with promising visual effects, already satisfying the resolution requirement of most practical applications. The transmission efficiency of nano-hole arrays is one aspect needed to be further improved, and their sensitivity to the refractive index of environment provides them the tunability to service as active optical control color devices.

2.2.3 Color generation via coupling SPs

We have already introduced some representative works on color filtering and imaging in previous two sections. In terms of color generating mechanism, they just simply based on either localized or propagating SPs. However, there is still plenty room for improvement of the spatial resolution and color vibrancy for the plasmonic meta-surfaces. One of the most efficiency ways to promote the performance is to take advantage of the coupling between localized and propagating SPs. This coupling can provide an additional degree of freedom to manipulate the SPR and thus control the color more accurately.

One of the representative coupled plasmonic nanostructures is reported by Joel Yang's group. It contains a metallic nano-disk suspended on top of a dielectric pillar and a complementary metallic hole as a back reflector [6, 8, 14, 130, 131]. The top disks

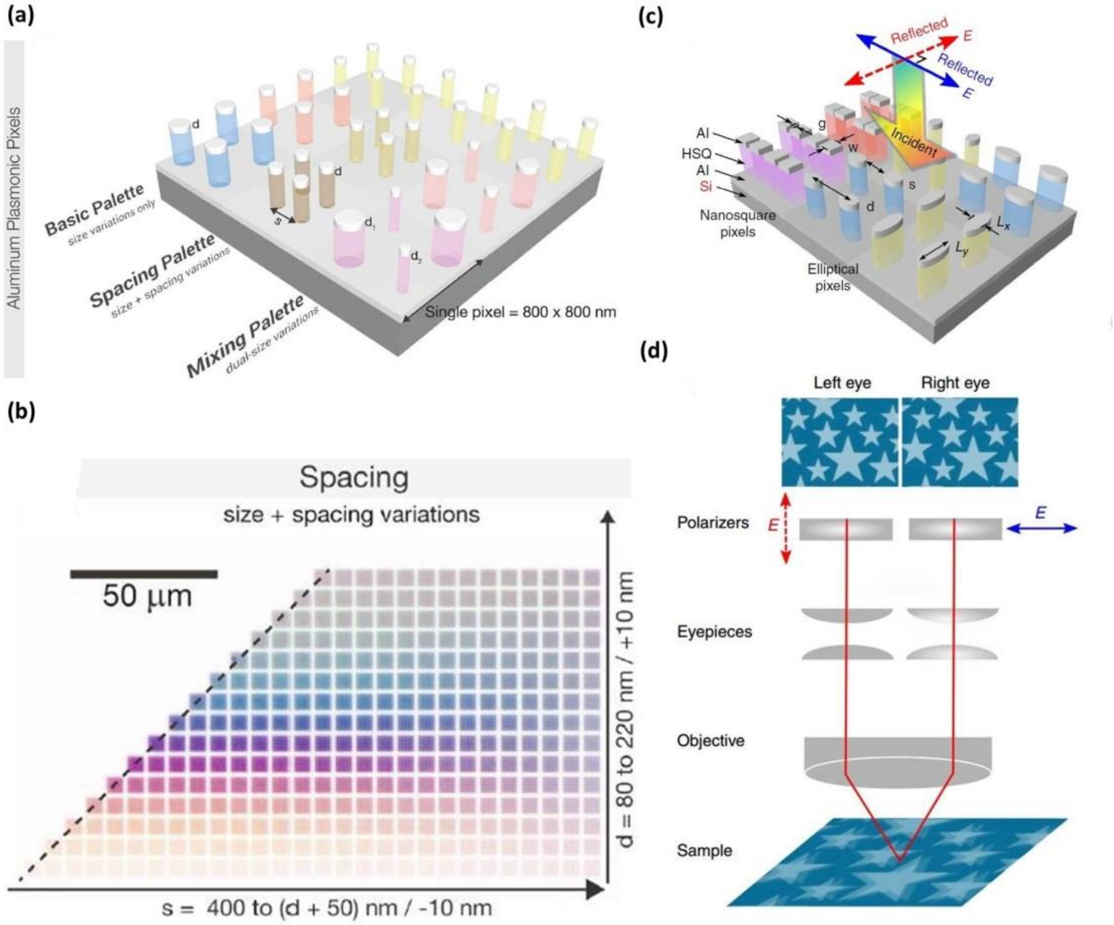

Fig 2-5 (a) Plasmonic color pixels composed of Al nano-disks with back reflector of varying disk size palette, varying disk size and spacing palette and mix-disks palette. (b) Full color palette for pixels in (a). (c) Schematic diagram of polarization dependent nanostructure with Al elliptical nano-disks and coupled nano-square pair with corresponding holes at the bottom Al layer. (d) Schematic of a stereomicroscope setup. By adding polarizers to the eyepieces of a bright-field microscope, the imaging of two superposed microprints encoded in orthogonally polarized pixels present two laterally displaced images to the left and right eyes of a viewer, resulting in depth perception. (a)—(b) Reproduced with permission [14]. Copyright 2014, ACS. (c)—(d) Reproduced with permission [6]. Copyright 2014, NPG.

provide LSPRs and the back reflector provides SPPs, and the height of the dielectric pillars determines the coupling between them. Previously this kinds of structure had been used for ultrahigh and uniform surface-enhanced Raman scattering [131], and demonstrating extraordinary light transmission effect with transparent substrate [130]. By depositing a thin layer of Au-Ag on hydrogen silsesquioxane (HSQ) pillars on a silicon substrate, a high spatial resolution nano-printing technology at diffraction limit was fabricated. Manipulating the separation between pillars and the sizes of the metal top disks, the coupling between the resonances of disks and the back reflector can be tuned to affect the reflected color. In this nanostructure the size of the unit cell varies from only 80 to 260 nm, much smaller than the wavelength, so that it is beyond the optical diffraction limit.

To enrich the color gamut and increase the practicality of this nano-printing technology , the constitute materials Au and Ag are replaced by Al, which is a more preferable metal for plasmonic color printing because of its neutral tint, durability, high reflectance in the visible regime, and low cost. Furthermore, as the schematic diagram of nanostructure shown in Fig 2-5 (a), developing from just varying gap and disk sizes, individual pixels are constructed by mixing disks of different sizes [14]. To complement the limited color palette produced by just modifying gap and disk sizes, dual-size-disk pixels (2×2 disks array mixed with different sizes) are constructed, which greatly increases the range of colors and provides an approach for plasmonic color mixing, and full color palette is present in Fig 2-5 (b). Even 3D plasmonic stereoscopic prints can be realized based on the localized-and-propagating-SP-coupled nanostructures by utilizing their polarization dependence [6]. Using biaxial color pixels composed of elliptical nano-disk—hole structures (shown in Fig 2-5 (c)) can independently control the reflected spectra of orthogonal polarized incident lights, so that two different color images can be encoded into the same area. Fig 2-5 (d) shows the process of generating depth perception by fine modulation of the differences between two images with different polarization. When the eyes see these two images of the same object but with small visual distance difference, the object looks like 3D. Therefore, the stereoscopic effects can be realized and high spatial resolution color imaging can be achieved.

2.2.4 Conclusion of plasmonic colors

All these nanostructures with LSPRs, SPPs and coupling of them are slim in thickness dimension, usually around 100nm or less, so we can consider them as meta-surfaces. Their excellent ability to generate color results from the wavelength-selective transmission or reflection based on SPs. Compared to the conventional pigments, plasmonic color shows more advantages including ultrasmall dimensions, impressive optical response, wide color tunability and compatibility for device integration. This thin geometry makes them easy for integration with miniaturized devices. The well-controlled plasmonic resonance also provides wide color range and accurately distinguished color. Moreover, diversity of plasmonic nanostructures contributes in achieving specific targets, such as high efficiency in transmission or reflection, narrower band-width for purer color, reduced incident angle dependence, tunable polarization applications, and electro-optic modulations.

Although plasmonic nanostructures have so many advantages and great potential in next generation color relevant applications, there are still some problems to be addressed. The first commercial applications would require a drastic reduction in patterning costs. Fabrication methods such as EBL and FIB are necessary to create master templates from which high-throughput replication processes such as nano-imprint can be used to create large volume of copies. On the other hand, the commonly used plasmonic materials, Au and Ag, are also expensive for mass production, leading to the recent trend to use Al. In addition to cost reduction, the performance of plasmonic devices needs to be comparable or better than existing technologies. For instance, in the application of plasmonic color filters for digital imaging products, the limiting factor is still the insufficient transmittance when compared to pigment-based filters. Hence, while many novel phenomena have been reported in literature, a strong need now is to significantly improve the optical performance of plasmonic color structures.

In summary, plasmonic nanostructures show great potential in development of color filtering, high-resolution printing and imaging, optical data storage and security. With improved low-cost fabrication technology, they are slated to offer improved performance and lower cost in applications ranging from digital displays, imaging sensors, molecular sensing, optical security devices, and optical data archival.

2.3 Color generation via non-plasmonic meta-surface

In section 2.2, we have introduced recent development of generating color by plasmonic meta-surfaces and reviewed some of the representative research works. Plasmonic color can provide high spatial resolution, vibrant colors and good compactness in devices. However, using metallic materials unavoidably results in large Ohmic loss in visible range, which is the primary limitation to improve efficiency for plasmonic meta-surfaces. Moreover, considering mass production, the costs of plasmonic noble metals, mostly Au and Ag, are expensive. Moreover, Ag even suffers the problem of oxidation, which reduces the working life of devices. Therefore, generating color with non-plasmonic structures has recently attracted a lot of interests.

Non-plasmonic structural color is not unfamiliar to people. Some living creatures, including some types of insects, birds and aquatic animals [132-139], naturally produce their colorful appearance with micro or even nano sized structures on their surface such as feathers, shells and scales. These colors usually come from the combined effects of thin film/multilayer interferences, grating diffraction, photonic crystals and light scattering. Nowadays, a great number of researches have been done to investigate and imitate the natural structural colors. For example, in Fig 2-6, the image of a butterfly wing shows the multilayered nanostructure arrangement, which can produce abundant colors. The bionic nanostructure has been fabricated to achieve the similar optical effects [135].

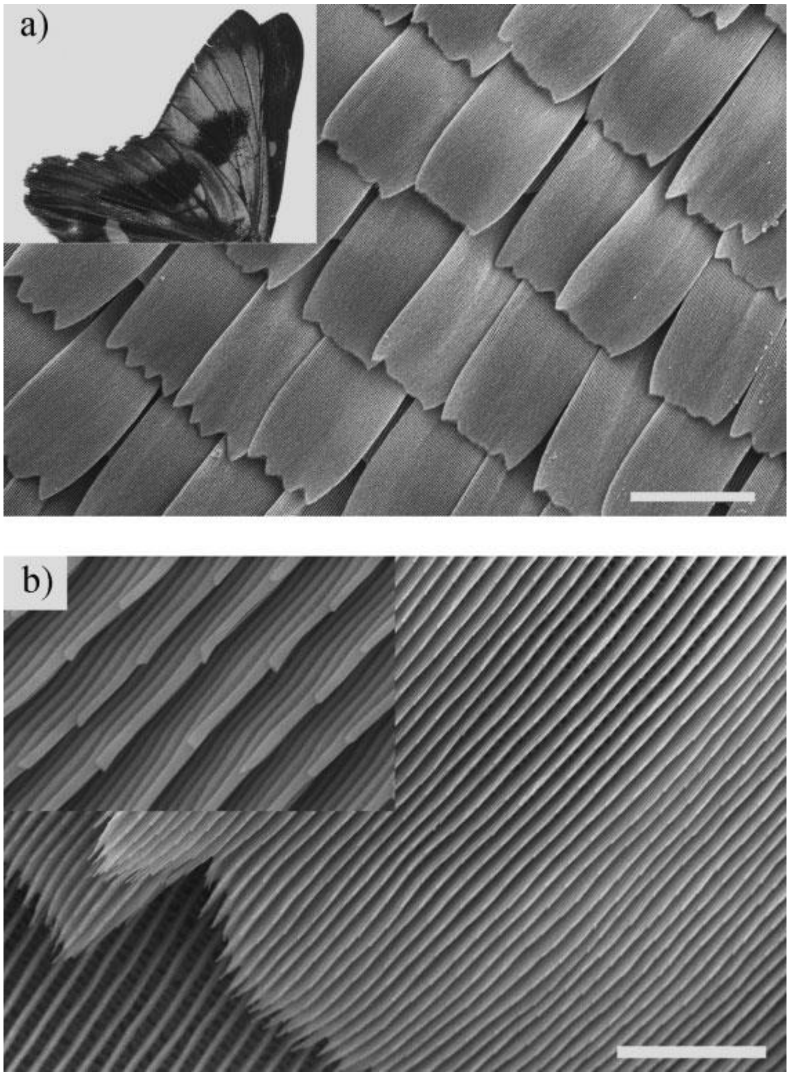

Fig 2-6 Morphology of butterfly wing scales (A. meliboeus). (a) SEM image of the wing scales (inset shows a photograph of the butterfly wing). Scale bar: 50μm. (b) Higher magnification SEM images of a butterfly wing scale, showing a multilayered nanostructure arrangement. Scale bar: 10μm. (a)—(b) Reproduced with permission [135]. Copyright 2009 John Wiley & Sons.

In addition to the bionic nanostructures, many artificially designed non-plasmonic nanostructures present their capacities to generate colors, such as the dielectric horizontal or vertical nanowires, gratings, multi-layer structures, high-index resonators, etc [16, 140-145]. These nanostructures are designed with many specific mechanisms, including waveguide modes scattering, diffractions, Mie scattering of high index particles with magnetic and electric resonance modes. In many of these research works, Si, as a widely used semiconductor, is a desirable material because of its high refractive index and relative low intrinsic loss compared to metals in the visible regime, and the advancement of related fabrication and characterization techniques.

However, in most of the recent researches, the dimensions of non-plasmonic nanostructures are larger than plasmonic ones in some extent. To deal with this problem, in the following section, we have presented a Si fin nanostructure for color printing with high spatial resolution beyond the optical diffraction limit and slim thickness to serve as a meta-surface. The dimension parameters for specific color can be easily designed and controlled based on the effective medium approach.

2.3.1 Color generated by Si nanostructure

To propose a non-plasmonic meta-surface for color generation, silicon (Si) could be a suitable candidate material. Si is the most widely used material in semiconductor industry. Relying on its mature technology platform, fabrication and characterization techniques of silicon-related devices has undergone tremendous developments in the past several decades. Recently, the optical characteristics of Si nanostructures have attracted a lot of interests in the area of nano-photonics due to the following two advantages. First, the permittivity of Si in the visible regime ranges approximately from 15 to 30, so that Si nanostructures are suitable for performing as optical cavities with ultra-small sizes [146]. Second, as the key advantage of Si compared to typical noble metals with SPRs, it has a much smaller Ohmic loss, which enhances its potential to be an ideal material for high quality factor optical cavities [147].

Due to the above advantages, Si nanostructures have been used for various optical applications in different areas, such as dielectric gradient meta-surface [47], chirality beam splitter [148], negative-angle refraction [149], color display with Si nanowires [141, 142, 150] and multispectral imaging with vertical silicon nanowires [140, 151, 152]. In these researches, the Si nanostructures essentially support waveguide modes or optical scattering modes to realize the designed functionalities. For these waveguide modes in visible light range, the dimensions of Si nanostructures have to be above the cut-off wavelength, typically above 30nm. Therefore, the Si nanostructures with dimensions below the cutoff are rarely investigated. Recently, with the development of the fabrication technology, Si nanostructures below 20nm can be realized already.

In this section, we present a sub-diffraction color printing with the color pixel made of silicon nanostructures with width dimensions of below 20-nm, and height dimensions of around 100nm as a meta-surface. Dr. Dong Zhaogang had fabricated the sample and measured the spectra, and I had simulated the nanostructures and built up the theoretical model. Our work is different from the research works in the literature on Si nanostructures, where were utilizing the scattering to manipulate light and generate colors. In comparison, the scattering from our presented Si nano-fin structure, with width of less than 20 nm, is negligible, and the periodicity is also small that the grating effects can be avoided. It is shown that the Si fin nanostructures could be approximated by an effective medium with the refractive index calculated based on the volume ratio. We believe this high spatial resolution Si color pixel has great potential in on-chip color nano-printing and related applications in semi-conductor industry.

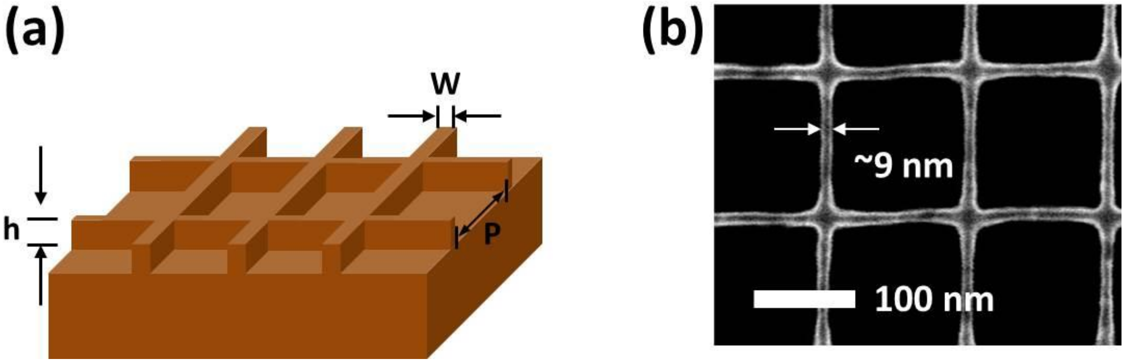

Fig 2-7 (a) Schematic of single color pixel made of Si nano-fin structure. (b) Scanning electron micrograph (SEM) images of the silicon nano-fin structures with a width of 9nm.

2.3.1.1 Structure and results

Our structure is an ultra-narrow Si square fin on the Si substrate, as shown in Fig 2-7. Fig 2-7 (a) presents the schematic of structure, the height *h* of the fin is about 90nm; the width *w* of the fin varies from 8nm to 16nm, which is much below the cut-off of waveguide modes; and the periodicity *P* of the fin varies from 60nm to 400nm, so in the small part of these periodicities the pixel sizes can be beyond the optical diffraction limit. Fig 2-7(b) presents a typical scanning electron micrograph (SEM) image of the silicon nano-fin structures with a typical width of 9 nm.

These Si fin nanostructures were obtained by ion reactive plasma dry etching, and the HSQ protection mask was fabricated by EBL with a corresponding exposure time of 0.75 μs. If the EBL exposure time is increased further, the HSQ protection mask will have a thicker line so as to result in a wider Si nano-fin.

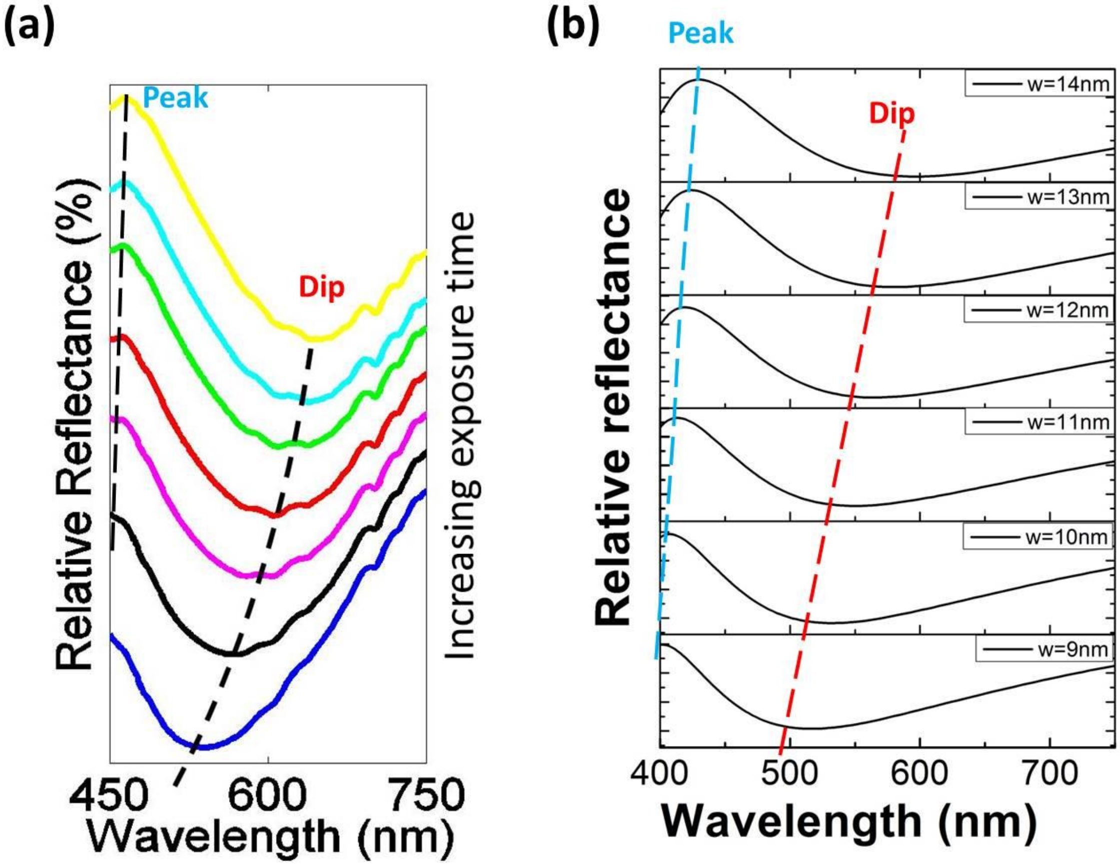

Fig 2-8 (a) Experimental measured relative reflectance spectra for various exposure times. The increasing exposure time refers to increasing width, which varies from 9nm to 14nm. (b) Simulated relative reflectance spectra for various fin widths with respect to flat silicon substrate. The nano-fin has a height of 90 nm and a pitch of 140 nm.

Fig 2-8 shows the (a) experiment and (b) Finite-difference time-domain (FDTD) simulation relative reflectance spectra with respect to the flat Si substrate for a set of Si fin nanostructures with height h=90nm and periodicity P=140nm. In experiment, the exposure time varies resulting in a range of width from 9nm to 14nm. The width increases as the exposure time increases. Accordingly, the simulation was done on the nanostructures with width increasing from 9nm to 14nm with a step of 1nm. It is shown that the simulation results resemble the key features of the experimental measured results, where the spectra show a red shifted trend as the width increasing and the dip wavelength is shifted from 500 nm to 600 nm.

Meanwhile, the variation of periodicities of the nanostructures can also affects the reflected spectra. By controlling both the width and the periodicity of Si fin, the reflected spectra can be manipulated and designed color can be generated. As shown in Fig 2-9, optical microscope images of Si fin nanostructures with different dimensions present different colors. With this color palette, high spatial resolution color imaging can be achieved.

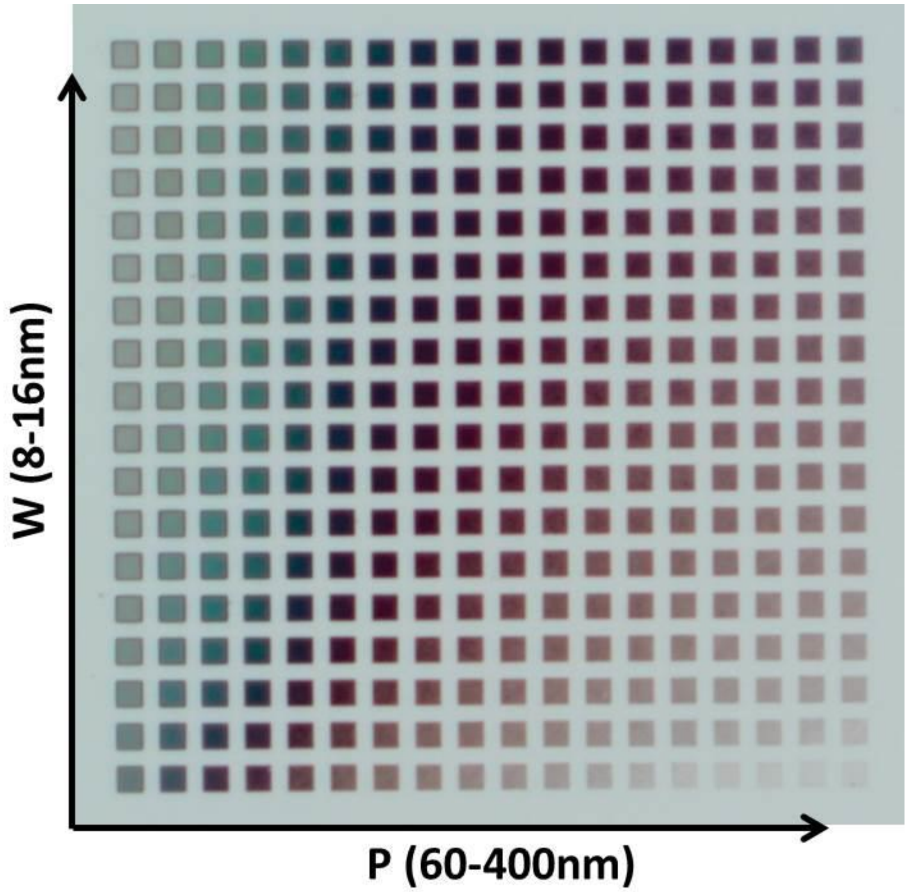

Fig 2-9 Bright-field optical microscope images of the fabricated silicon nano-fin structures with respective pitch sizes and widths.

2.3.1.2 Effective Medium Approximation

In order to have a clearer understanding of the physical origin at both the peak and dip wavelengths, we plot out the respective electric field distributions at these two wavelengths (*i.e.* 426 nm and 600 nm) as shown in Fig 2-10 (c)-(f), respectively. Since the incident optical field is polarized along *x*-direction, in this case, this incident optical field will possibly excite the transverse magnetic (TM) modes for the silicon nano-fin along Plane B and transverse electric (TE) modes for the one along Plane A, respectively. However, considering the sub-20nm width, TE modes in Si nano-fin along Plane A cannot be excited. That's why in these figures the electric field inside Si nano-fin along Plane A is weak (no TE modes) and inside nano-fin along Plane B is strong (excited TM modes). Moreover, for Plane A in Fig 2-10 (c) and Plane B in Fig 2-10 (d), the electric field distribution has a constructive interference within nano-fin structure along *z* direction, and it satisfies the condition that:

$$2\,h=\lambda/\,n_{eff} \qquad (2.\,8)$$

where λ is the wavelength in vacuum, n_{eff} and h denote the effective refractive index of the silicon nano-fin structure, and the height of the silicon fin, respectively. Similarly, for Plane A in Fig 2-10 (e) and Plane B in Fig 2-10 (f), the dip wavelength satisfies the condition:

$$2\,h=\lambda/(2\,n_{eff}) \qquad (2.9)$$

so as to result in a destructive interference within this nano-fin structure along *z* direction. In addition, when the width of nano-fin is becoming smaller from 14 nm to 9 nm as shown in Fig 2-8, the silicon ratio of the fin structure is reducing. As a result, the effective refractive index n_{eff} will decrease, and thus both the peak and dip wavelengths will shift to smaller values.

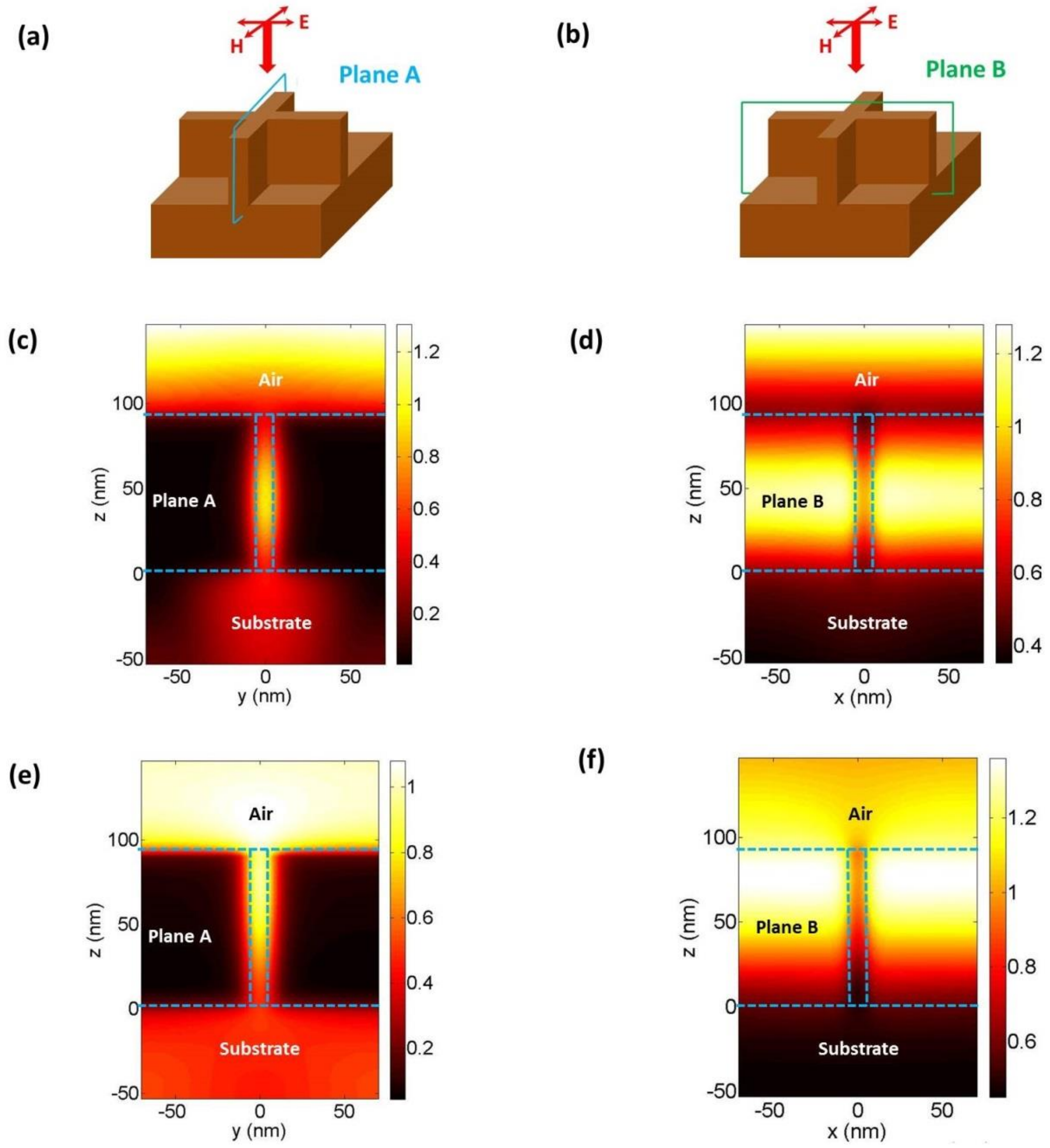

Fig 2-10 FDTD simulation schematic with the defined monitor planes, *i.e.* (a) Plane A and (b) Plane B. The nano-fin has a height of 90 nm and a pitch of 140 nm. (c)-(f) Spatial distribution of the electric field magnitude at Plane A and Plane B, respectively, with a silicon fin width of 14 nm. (c)-(d) and (e)-(f) present the electric field magnitude at the peak wavelength and the dip wavelength of the reflectance spectra, respectively. The green dash line denotes the boundary of the nano-fin structure.

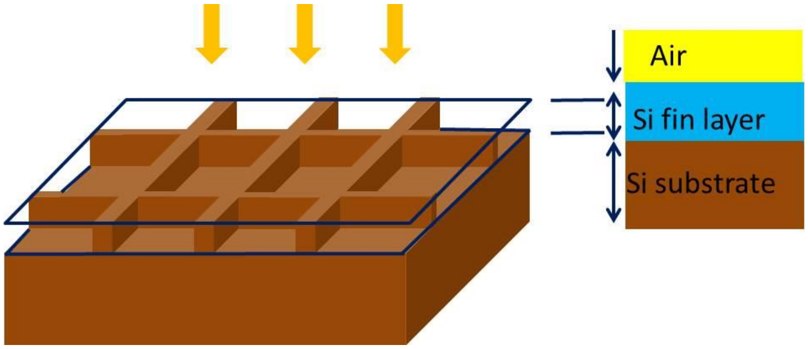

Fig 2-11 Schematic of the Si fin nanostructure equivalent to a three-layer Fabry-Perot cavity, considering the fin as a homogeneous layer.

Next, we would like to present the effective medium theory to explain the resonances of the silicon nano-fins as observed in Fig2-2. Most research works on silicon nanostructures are utilizing their scattering to manipulate light and generate colors. However, the scattering of our silicon nano-fin with width of sub-20 nm is negligible, and the periodicity is also small to avoid the grating effects. The resonance of the structure results from the multiple reflections of "air – Si fin – Si substrate", which can work as a Fabry-Perot cavity as shown in Fig 2-11. Since this silicon nano-fin is in such a small size as compared to the wavelength, the whole macroscopic fin layer can be regarded as a homogeneous layer, as shown in Fig 2-11. Here we use the Lichtenecker's equation [153] to model this Si fin layer:

$$\varepsilon_L^k = f_1\varepsilon_1^k + f_2\varepsilon_2^k \tag{2.10}$$

where ε_L is the Lichtenecker's effective permittivity, f_1 and f_2 are the filling factors ($f_1 + f_2=1$), ε_1 and ε^2 are the permittivity of material 1 and 2, respectively. Parameter k is related to the specific microgeometry topology of the composite, and ranges from -1 to 1. In specific cases, k=1 denotes that the composite is a system consisting of plane-parallel layers disposed along the field, while k=-1 denotes that the composite is a system consisting of plane-parallel layers disposed perpendicular to the field. In our fin nanostructure, due to the geometry symmetry and the polarization dependence, when the incident polarization is along one of the Si fins, the Si fin nanostructure can be regarded as a composite of parallel slabs perpendicular to E field (k=-1) and parallel slabs along E field (k=1), neglecting the coupling between Si fins with different directions. However, the permittivity of Si is much larger than that of air, and the filling factor of Si is much smaller than air. So that when considering the Si fin perpendicular to E field (k=-1), ε_L will be closed to 1, which means the Si fin along this direction contributes little to the effective permittivity. This agrees with the previous discussion that TE modes in the nano-fins perpendicular to E field cannot be excited, and only TM modes in nano-fins along E field are excited. Thus, the effective permittivity of Si fin structure will be mainly determined by the Si fin along E field (k=1), so that the effective permittivity can be simplified to the following equation:

$$\varepsilon_{\text{eff}} = A\,\varepsilon_{\text{Si}} + (1-A)\,\varepsilon_{\text{Air}} \quad , \qquad \varepsilon_{\text{eff}} = n_{\text{eff}}^{\,2} \text{ , (when } \mu_0=1) \tag{2.11}$$

where ε_{Air}, ε_{Si} and ε_{eff} denote the permittivity of air (ε_{Air}=1), Si, and the effective permittivity of the Si nano-fin structure. *A* is the effective volume fraction of Si fin along the E field direction.

Based on this effective medium approximation, we can easily calculate the multilayer reflectance by transfer-matrix method (TMM) [154]. The TMM used in optics is a method to analyze the propagation of electromagnetic waves through a layered medium. The TMM is based on the continuity conditions for the electric field across boundaries from one medium to the next according to Maxwell's equations. The field at the end of a layer can be derived from the field at the beginning of the layer by a simple matrix operation. A stack of layers can then be represented as a system matrix, which is the product of the individual layer matrices. The final step of the method involves converting the system matrix back into reflection and transmission coefficients. In a simplified case, a normal incidence from material 1 to material 2, at the interface of two materials, we have:

$$\mathrm{M}_{12} = \begin{pmatrix} 1+\frac{n_1}{n_2} & 1-\frac{n_1}{n_2} \\ 1-\frac{n_1}{n_2} & 1+\frac{n_1}{n_2} \end{pmatrix} \tag{2.12}$$

and inside material 1, we have:

$$P_1 = \begin{pmatrix} e^{i(2\pi n_1 d_1/\lambda)} & 0 \\ 0 & e^{-i(2\pi n_1 d_1/\lambda)} \end{pmatrix} \tag{2.13}$$

where M_{12} and P_1 are the transfer-matrixes, M is at interface and P is inside material, the numbers denote the materials; n_1 and n_2 are the refractive index of material 1 and 2; d_1 is the thickness of material 1 and λ is the wavelength in vacuum. With these transfer-matrixes M and P, we can calculate the reflectance by:

$$\begin{pmatrix} \mathrm{t} \\ 0 \end{pmatrix} = M_{air-fin} P_{fin} M_{fin-Si} \begin{pmatrix} 1 \\ r \end{pmatrix} \tag{2.14}$$

where *r* and *t* are the reflection and transmission coefficients, respectively.

With the calculation of TMM, we can compare the TMM and FDTD results of structure with different dimensions. In Fig 2-12, the height of Si nano-fin varies, which changes the transfer-matrix P in eqn. (2.13). When the height is too small, the fin layer is almost negligible, so the reflected spectra would be similar to a flat Si film. As thin film interference, when the height becomes larger, the wavelength of main resonance peak, which refers to $2n_{eff}h=\lambda_0$, is increasing. When the height of the silicon nano-fin is larger than 140 nm, the structure will start to support higher-order mode (when $2n_{eff}h=2\lambda_0$ for reflected peak).

In Fig 2-13, the periodicity of Si nano-fin varies, thus the effective volume fraction of Si *A* in eqn. (2.11) is changed. So the effective permittivity and refractive index of Si nano-fin also changes. When the periodicity of fin structure increases, the volume fraction of silicon decreases, so that the effective refractive index will decrease, and the reflected peak (constructive interference) will shift to a shorter wavelength. And when periodicity is large, the incremental of periodicity leads to less reduction of effective refractive index, so the resonance wavelength shifts slightly with large periodicity.

In Fig 2-12 and Fig 2-13, the FDTD and TMM results match each other very well substantially. There are only a few minor differences, which are relatively clear at shorter wavelength. The reflected peak bandwidth is a bit smaller in FDTD results; in Fig 2-12, for FDTD, it is likely to see the high order mode referring to $2n_{eff}h=3\lambda_0$ with large height, but this mode can hardly be seen in TMM; and in Fig 2-13, for FDTD, resonance intensity with smaller periodicity is a bit larger than that with large size, while for TMM, resonance intensity with larger periodicity is relatively larger. At shorter wavelength, the Si fin nanostructures are relatively larger in terms of wavelength. And the effective

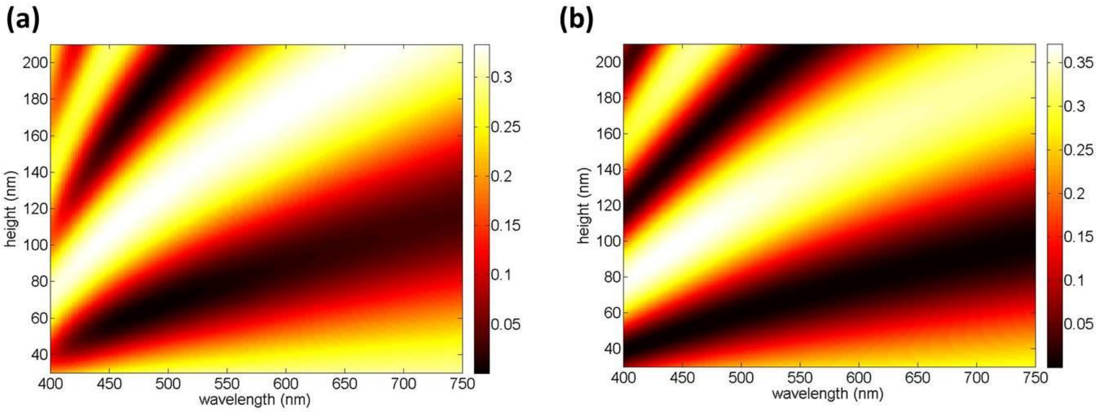

Fig 2-12 Comparison of the simulated reflectance spectra by (a) FDTD and (b) TMM approach based on the effective medium theory, with the Si nano-fins with periodicity of 140nm, and width of 14nm and different height.

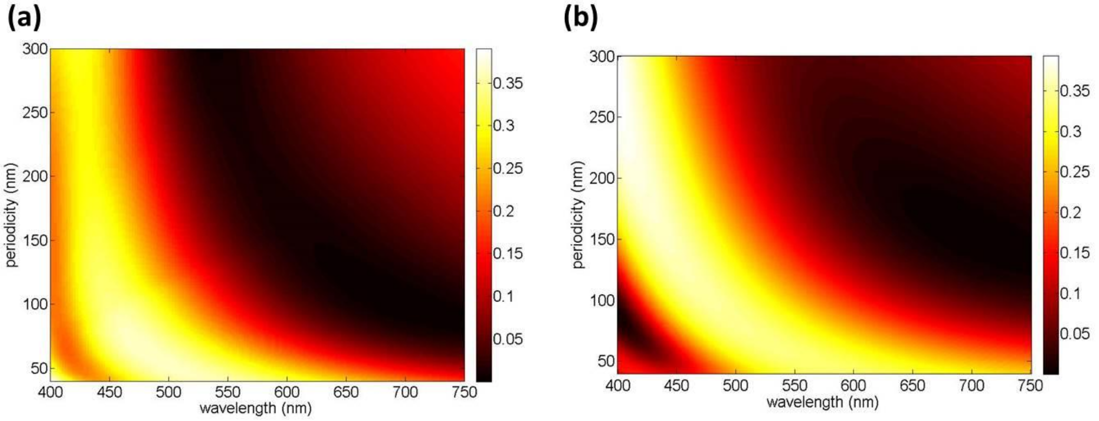

Fig 2-13 Comparison of the simulated reflectance spectra by (a) FDTD and (b) TMM approach based on the effective medium theory, with the Si nano-fins with height of 90nm, and width of 17nm and different periodicity.

medium approximation ideally applies to structures much smaller than wavelength, so that the Si fin layer becomes not so "homogeneous" at short wavelength as at long wavelength, which leads to minor differences between FDTD and TMM results. And at shorter wavelength, the refractive index of Si is larger, making the optical path inside Si nanostructure even smaller. In spite of this condition, the fin width is still much smaller than wavelength and the spectra from two methods agree with each other quite well. That is a key advantage of our ultra-narrow fin nanostructure. If the width is above 30nm, the effective medium theory cannot work so well.

The TMM has an overwhelming advantage in calculation time and requirement of computer performance. For FDTD simulation, we were using 3D FDTD method Maxwell solver from the commercial software package *Lumerical FDTD Solutions*. We use periodic boundary conditions with the maximum unit cell size up to 300nm, and the finest mesh size should be 0.5nm because the minimum width of the Si fin is just 8nm. And in the z direction, which is along the plane wave light incident direction, the simulation distance is comparable to wavelength. Although we have used symmetric (y direction with E field polarized in x direction) and asymmetric (x direction) conditions to reduce the amount of calculation, such an ultra-fine mesh compared to simulation region requires large memory and long calculation time. To achieve a spectra map like Fig 2-12 and Fig 2-13 by sweeping parameters, FDTD takes quite a few hours or even several days on high-profile server, while it just needs several seconds or less by TMM on low-profile computer. Therefore, the design of Si fin nanostructure for specific color by TMM is much more convenient and efficiency.

Another characteristic should be noticed is the polarization dependence. As the electric field distribution shown in Fig 2-10, only TM modes can be excited. Therefore, the electric field inside the Si bar along the direction which is perpendicular to the incident polarization can be almost neglected. And in the effective medium model, we also mentioned the polarization dependence. Fig 2-14 presents the FDTD simulated reflectance of the nanostructures with Si bar array only along x direction and only along y direction, with incident light polarized at x direction, and compares them with the whole Si fin and the flat Si substrate. It is clear that the result of only x-direction Si bar is closed to the whole Si fin, while the only y-direction is similar to the Si substrate, which means that the contribution to the cavity mostly comes from the bars along the incident polarization direction in the fin structure. This also supports the appromxiation in effective medium that we only consider the Si fin along E field direction as the effective volume, and for Si fin along the other direction, the effective permittivity is closed to air, as claimed above. Based on this polarization dependence, the Si fin meta-surface can also be used in polarization related applications like bio-sensing, data security and stereoscopic prints, which is usually done by plasmonic meta-surfaces as we discussed in section 2.2.1.

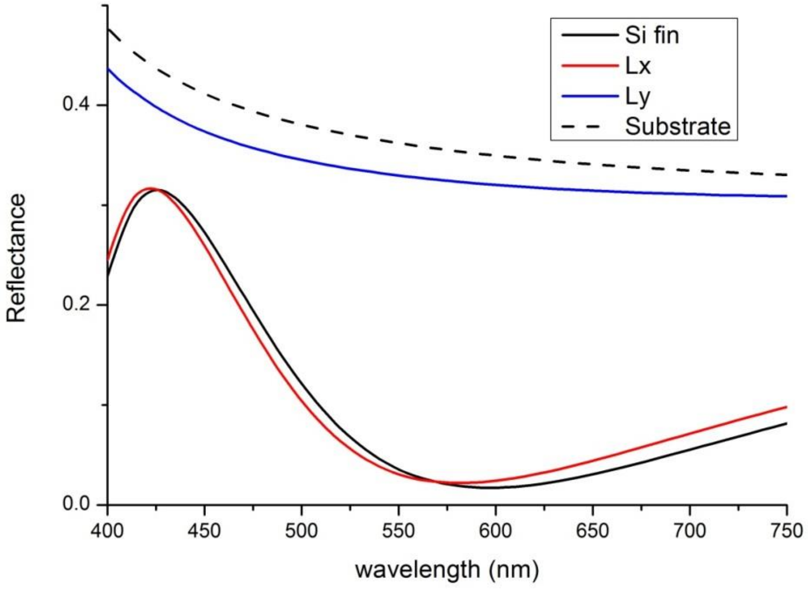

Fig 2-14 Reflectance of Si fin nanostructure, only Si bar array along x direction, only Si bar array along y direction and flat Si substrate with incidence polarized in x direction. The periodicity is 140nm, height is 90nm and width is 14nm.

To conclude, in this section we present an ultra-narrow Si fin nanostructure based color printing technique with ultra-high spatial resolution. For the Si fin with such small width and periodicity, which is much smaller than wavelength, the fin layer can be equivalent to an effective medium with a homogeneous refractive index. Such a simplified effective medium will enable a direct TMM calculation of required Si nanostructures for achieving certain designed color. We believed that the presented Si color pixel beyond optical diffraction limit will have a very good compatibility with the existing semi-conductor industry and it paves a way towards the full potential for on-chip color nano-printing applications.

Chapter 3 Manipulating Polarization of EMWs by Meta-Surface: Plasmonic Quarter Wave Plates

3.1 Introduction: polarization and phase manipulation via meta-surface

In last chapter we have investigated the light intensity spectrum manipulation by meta-surface. Other than the intensity or amplitude of EMWs, meta-surfaces can also control the phase and polarization of EMWs, because the resonance is always accompanied by a large phase shift, and the polarization is determined by the relative phase difference between orthogonal directions. To be specific, in this chapter we will only discuss about the plane waves, and the polarization only refers to linear polarization and circular/ elliptical polarization. As well as the manipulation of light intensity spectra which can provide abundant colors and images, the manipulation of polarization state of EMWs is also of great importance, due to the information carried by polarization states in applications such as chemical and biological sensing, optical data storage and transmission. Conventional methods to control the polarization state of light are using birefringent materials, which are anisotropy in refractive index along the two orthogonal axes [155]. In this way, the difference in phase delay of different polarization needs to be gradually accumulated along the optical path inside the birefringent materials, leading to large bulk size, high loss and limitation in choice of materials. In terahertz (THz) frequency regime, the problem is even more serious. As well as the longer wavelength, the limited natural birefringent materials only provide small birefringence index, resulting in large thickness of the elements. It brings much difficulty in integrating polarization manipulators into compact devices and systems. For instance, one of the most commonly used polarization controlling optical devices is wave plate. A quarter wave plate (QWP) is an optical device that alters the polarization state of a transmitted or reflected light wave, which converts linearly polarized light into circularly polarized light and vice versa [155]. It can be used to produce elliptical polarization as well. However, conventional QWPs constructed of birefringent materials suffer difficulties of reducing dimensions, which limits their integration into compact optical systems. Recently, more and more researches concentrate on QWPs made by plasmonic meta-surfaces.

Plasmonic meta-surfaces are able to manipulate polarization states with an ultra-thin layer, based on the abrupt phase shift on the resonators. With the asymmetry in geometry of the plasmonic nanostructures, the resonance response to different polarized incidence can be conveniently controlled. Particularly, quite a lot of research works have been done on QWPs and other polarization related optical applications like chiral manipulation and half wave plates based on meta-surfaces. Most of these polarization related applications are realized in infrared range [28], THz [22-27] and microwave [156, 157].

In this chapter, we will present several works on plasmonic QWPs which are ultra-thin compared to the working wavelength, in visible/near-infrared and THz range. These QWPs, although working at quite different wavelength, base on surface plasmons. One of the QWPs works at the boundary of visible light and infrared, and it is hybridized with a phase-change material, $Ge_2Sb_2Te_5$ (GST), which makes this wave plate switchable. Another QWP works at THz range, where the metal is more “ideal”, and it can achieve better converting ratio and efficiency. An improvement on this QWP is realized by hybridizing another phase change material, vanadium dioxide (VO_2), also making it switchable. These switchable phase-change meta-surfaces provide a promising way for realization of polarization manipulating components, enabling novel applications with integrated optical devices.

3.2 Switchable plasmonic QWP in visible/near—infrared light

Since many research works had been done on QWPs by plasmonic meta-surface, it is necessary to improve the performance of plasmonic QWPs. One of the promising ways is to make this device active. For meta-surface, usually the functionality is settled once it is fabricated, and can never be changed. However, when we bring phase-change material (PCM) into the meta-surface, it is possible to control the functionality or working wavelength of the optical devices and make them switchable. In the following sections we will introduce some PCMs and then report our switchable plasmonic QWP based on metal—PCM meta-surfaces.

3.2.1 Phase-change materials

PCM technology has provided the possibilities to achieve meta-surfaces with active functionalities. The amorphous and crystalline phases of PCMs can present significantly different optical properties, and the phase states can be rapidly switched [158, 159]. The phase state refers to the arrangement of the constituents (atoms or molecules) of the materials. When the environment changes, such as changing temperature and illumination, the arrangement of the constituents of PCMs will be changed, leading to the phase

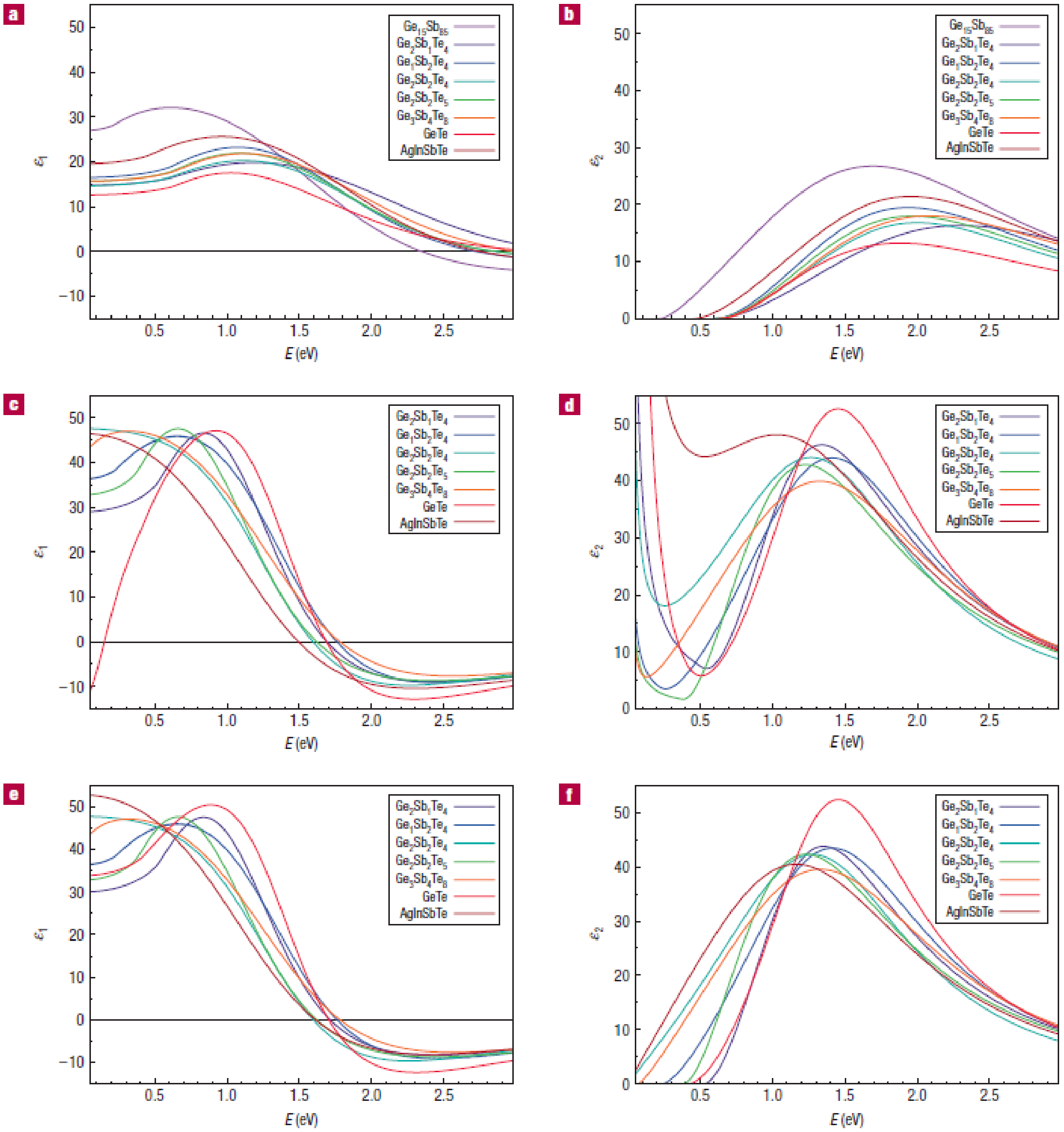

Fig 3-1 Dielectric function $\varepsilon_1(\omega)$ and $\varepsilon_2(\omega)$ for various materials. (a) and (b): Amorphous phase-change sample. (c) and (d): Crystalline sample including Drude-type contribution. (e) and (f): Crystalline sample with Drude contribution subtracted. (a)—(f) Reproduced with permission [160] Copyright 2008 NPG.

change. In crystalline state, the constituents of material are arranged in a highly ordered microscopic structure, forming a crystal lattice that extends in all directions; while the amorphous state lacks the long-range order characteristic of a crystal and has an internal structure made of interconnected structural blocks. Based on the distinct properties of their amorphous and crystalline phases, PCMs are widely used in applications of rewritable optical data storage [161]. In addition, these PCMs can also be hybridized with surface plasmons for tunable plasmonic applications, including research works on negative index metamaterials [162], Fano resonances [163, 164], flat lens [165] and perfect absorbers [32-34], etc.

Fig 3-1 has shown the dielectric functions of some of the PCMs calculated by ref. [160]. $\varepsilon_1(\omega)$ and $\varepsilon_2(\omega)$ are the real part and imaginary part of the dielectric functions, respectively. At low energy, the Drude contribution from free carriers should be subtracted, as shown in Fig 3-1 (e) (f). The shift of dielectric functions between amorphous and crystalline states of these PCMs is obvious in visible and near-infrared light range, providing the potential to be employed as active material in our design of switchable QWPs at respective wavelength. In the following of this section, the data of dielectric functions for $Ge_2Sb_2Te_5$ (GST) is adopted from this paper.

3.2.2 Switchable plasmonic QWP with GST

We have designed a switchable reflective metasurface-based multi-wavelength QWP (MMQWP) in visible and near-infrared range. This MMQWP is constructed by arrays of Au-GST hybrid cross nanostructure with different arm length. The Au nano-cross is strutted by GST, on a flat Au film. Due to the difference in arm length, these nanostructures can support two orthogonal resonant modes, and the asymmetry results in a $\pi/2$ phase delay between the polarizations along different arms, working as a QWP. In addition, when the phase state of GST is switched by heating, the resonances of both arms shift. By properly design of the dimensions of the nanostructure, we have realized a switchable dual-band QWP, with amorphous GST working at 732nm in visible light and crystalline GST working at 781nm in infrared range, with more than 95% of the energy in reflected light converting from linear polarized light into circular polarized light. When the phase state of GST is switched, the performance of QWP is obviously reduced, which enables the active control of polarization states.

Fig 3-2 shows a schematic of the switchable MMQWP, which is composed of a flat Au film with cross-shape GST array supporting the Au cross resonators. The periodicity P of the unit cell is 500nm, the bottom Au film is optically thick, the height of GST h is 100nm, the thickness of top Au cross is 50nm, the width of the cross w is 50nm, and the arm length of cross L_x and L_y is 300nm and 385nm, respectively. Thin Si_3N_4 layers of 2nm are added between Au and GST to prevent diffusion. This meta-surface could be fabricated by firstly patterning PMMA nano-cross aperture array on Au film by EBL, and then sputtering Si_3N_4, GST, Si_3N_4 and Au on it layer by layer, at last lifting-off the PMMA. The heater can be located behind the meta-surface to control the temperature.

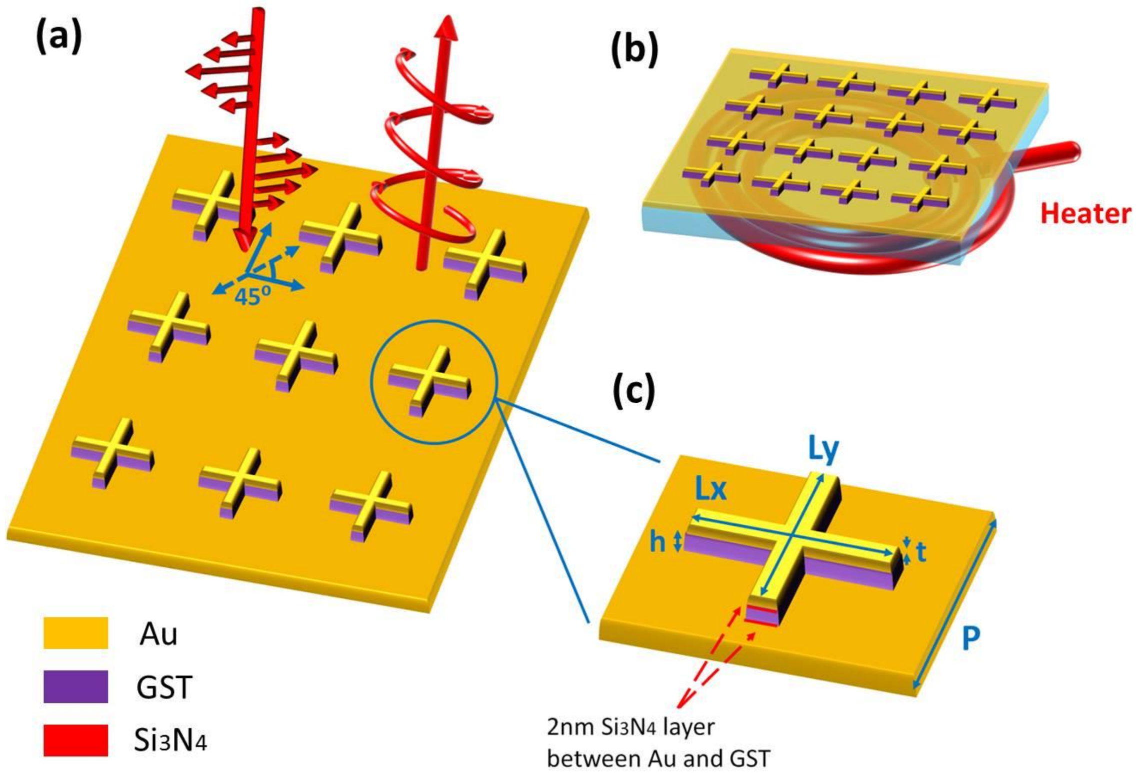

Fig 3-2 (a) Schematic of light reflected by the switchable MMQWP. (b) Schematic of heating system. (c) Schematic of the unit cell, in which P=500nm, h=100nm, t=50nm, L_x=300nm and L_y=385nm. In the structure gold color presents Au, purple presents GST and red presents Si_3N_4.

With normal incident light linearly polarized with 45 degree to *x* axis, the Localized surface plasmon resonance is excited on both arms of the top Au nano-cross, while the propagating surface plasmon is excited on the bottom Au film. The coupling of localized and propagating surface plasmon can be manipulated by the height and phase state of GST.

To design the dimension of the arm length of nano-cross, we have investigated the intensity and phase of reflected lights for nano-rod arrays supported by GST layer on Au film with different length, from 250nm to 450nm, with incident light polarized along the

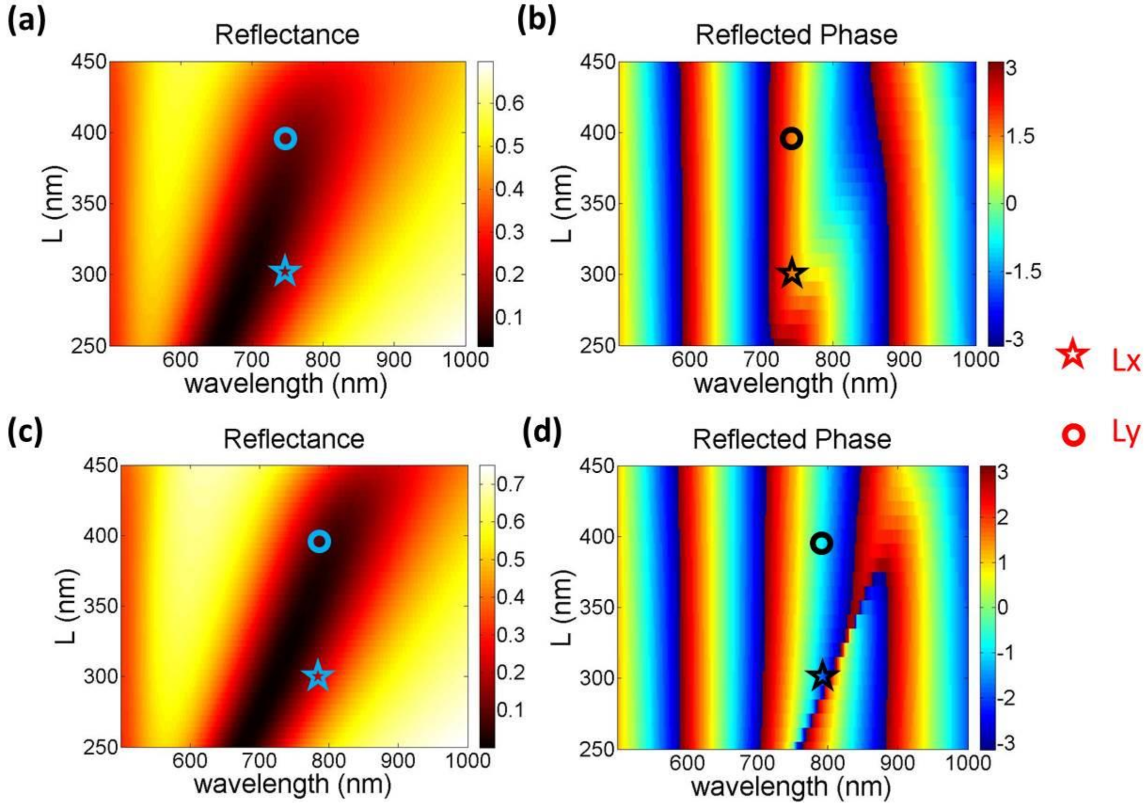

Fig 3-3 FDTD simulation of (a) reflectance and (b) reflected phase of Au-GST hybrid nano-rods with different length (L) at 300K (amorphous state); and (c) reflectance and (d) reflected phase of Au-GST hybrid nano-rods with different length (L) at 425K (crystalline state). The star and ring denote the length (L_x=300nm and L_y=385nm) chosen to form the cross and the corresponding working wavelength.

rods. Fig 3-3 shows the reflectance and reflected phase of nanostructures at 300K (room temperature) and 425K. The crystallization temperature of GST is between 373K and 423K, so Fig 3-3 (a) (b) and (c) (d) refer to GST in amorphous and crystalline states, respectively. The reflected phase is collected at a distance away from the meta-surface, so the reflected phase contains the phase generated by propagating path. However, we just need to care about the phase difference of nanostructures with different length at the same wavelength, so the propagating distance can be neglected. For reflectance, we can see the resonance wavelength is shifted about 50nm to 100nm for the same nanostructure when

GST transfers from amorphous to crystalline, depending on the length. For the reflected phase, the phase changes abruptly at resonances, as the typical characteristics for a Lorentzian resonance, and at the resonance wavelength, the phase difference which would be achieved by two different arm lengths, is much more obvious for nanostructure with crystalline GST than that with amorphous GST.

Because of the independence of the resonance on each arm of nano-cross, the phase delay between different polarization states can be achieved by different arm length, and the birefringence of meta-surface can be realized. Using either amorphous or crystalline GST, the QWP can be designed by controlling a phase delay of π/2 with the same reflectance, at different wavelength, as the arm length marked by star and ring in Fig 3-3. In addition, in Fig 3-3 (d), we can see the phase difference can almost approach π, which implies this kind of hybrid nanostructure is also possible to serve as a half wave plate. However, with the parameters for π phase delay, the reflectance is low and doesn't match each other, significantly reducing the performance.

As the normal incident wave is polarized at θ = 45 degree to x-axis, the incident and reflected electric field can be noted as:

$$\begin{aligned}\vec{E}_{inc} &= \left(\hat{e}_x E_0 \cos\theta + \hat{e}_y E_0 \sin\theta\right) e^{i\left(\vec{k}\cdot\vec{r}-\omega t\right)} \\ \vec{E}_{refl} &= \left(r_x \hat{e}_x E_0 \cos\theta + r_y \hat{e}_y E_0 \sin\theta\right) e^{i\left(-\vec{k}\cdot\vec{r}-\omega t\right)}\end{aligned} \tag{3.1}$$

where θ is the polarization angle, r_x and r_y are the reflection coefficients for unit incident intensity along x and y direction, respectively. And we simply assume that $\vec{r}$=0 and t=0. And

$$\begin{aligned} &R_x = \left|r_x\right|^2 \cos^2\theta, R_y = \left|r_y\right|^2 \sin^2\theta, \\ &\Phi_x = angle(r_x), \Phi_y = angle(r_y), \Delta\Phi = \Phi_x - \Phi_y \end{aligned} \tag{3.2}$$

where R_x and R_y are the reflectance for unit incident wave polarized at θ, Φ_x and Φ_y are the reflected phase and $\Delta\Phi$ is the phase difference between the two polarization states, respectively.

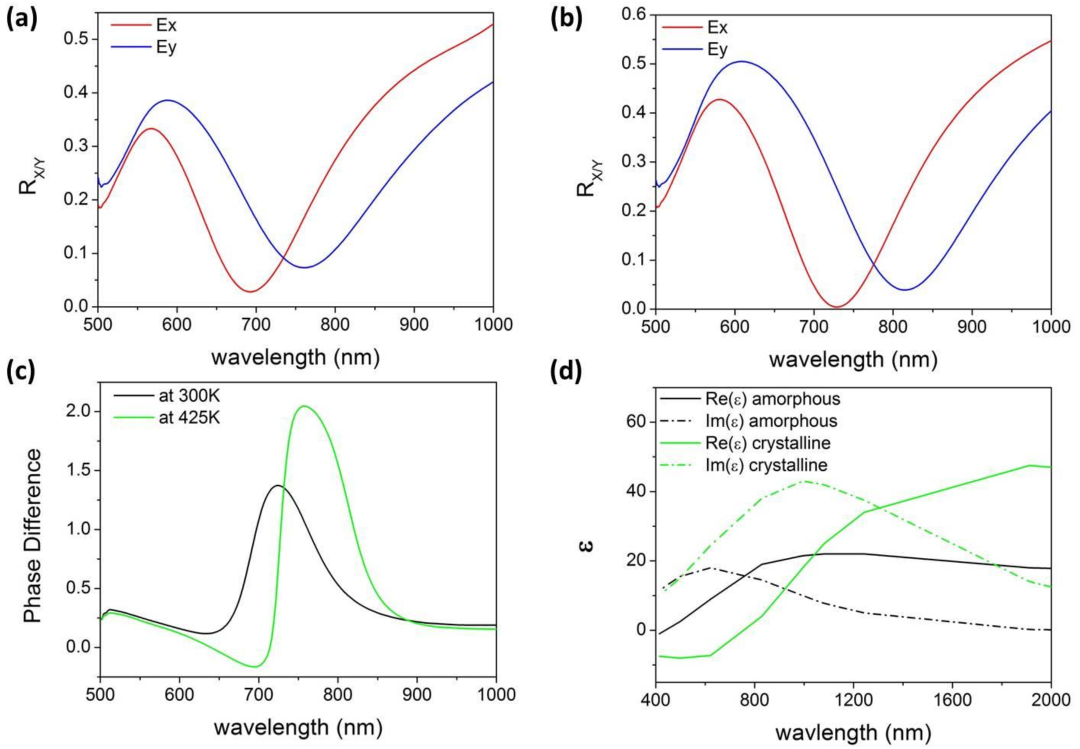

Fig 3-4 Reflectance for linear polarization along x and y direction for hybrid nano-cross structure (a) at 300K (amorphous) and (b) at 425K (crystalline). (c) Reflected phase difference between x and y polarization for hybrid nano-cross structure at 300K (amorphous) and 425K (crystalline). (d) The permittivities of GST in visible and near-infrared light range (referred to ref. [160].): the black lines denote amorphous states; the green lines denote crystalline states; the solid lines denote real parts and the dash lines denote imagery parts.

Therefore we present the reflectance of polarization in x axis and y axis for GST in amorphous at 300K in Fig 3-4 (a) and crystalline at 425K in Fig 3-4 (b). The resonance wavelength in x direction is 693nm for amorphous and 729nm for crystalline, while the resonance wavelength in y direction is 760nm for amorphous and 816nm for crystalline. And we should note that around 735nm for amorphous and 775nm for crystalline, the reflectance of x and y direction is closed. So we also plot the phase difference between x and y polarization for both states in Fig 3-4 (c). At 425K, the phase difference can be larger than π/2, so it is possible to generate circular polarized light with a π/2 phase different while R_x and R_y are closed; at 300K, although the phase difference cannot reach π/2, it is also maximized around the wavelength where x and y direction has the same reflectance. All the differences result from the changes of permittivities of GST at phase state transition, as shown in Fig 3-4 (d). The permittivity data is adopted from ref. [160].

To analyze the problem more clearly, the reflected wave is converted into right-hand circular polarization (RCP) and left-hand circular polarization (LCP), as following expression:

$$\begin{aligned} \vec{E}_{refl} &= \left(r_{RCP}\hat{e}_{RCP}E_0 + r_{LCP}\hat{e}_{LCP}E_0\right)e^{i\left(-\vec{k}\cdot\vec{r}-\omega t\right)} \\ R_{RCP} &= \left|r_{RCP}\right|^2, R_{LCP} = \left|r_{LCP}\right|^2 \end{aligned} \tag{3.3}$$

where r_{RCP}, r_{LCP} and R_{RCP}, R_{LCP} are the reflection coefficients and reflectance of RCP and LCP waves, respectively. Please note that the incident wave is linear polarized at θ =45 degree, E_0 is the total incident intensity, so the total reflection should be the sum of R_{RCP} and R_{LCP}.

In Fig 3-5 (a) (b), which shows the reflectance in term of circular polarization, it is obvious at the wavelength of 732nm at 300K and at the wavelength of 781nm at 425K, RCP is nearly zero, thus the reflected wave is almost LCP wave. Furthermore, the ellipticity of polarization can be calculated by:

$$Ellipticity = \frac{|r_{RCP}| - |r_{LCP}|}{|r_{RCP}| + |r_{LCP}|} \qquad (3.4)$$

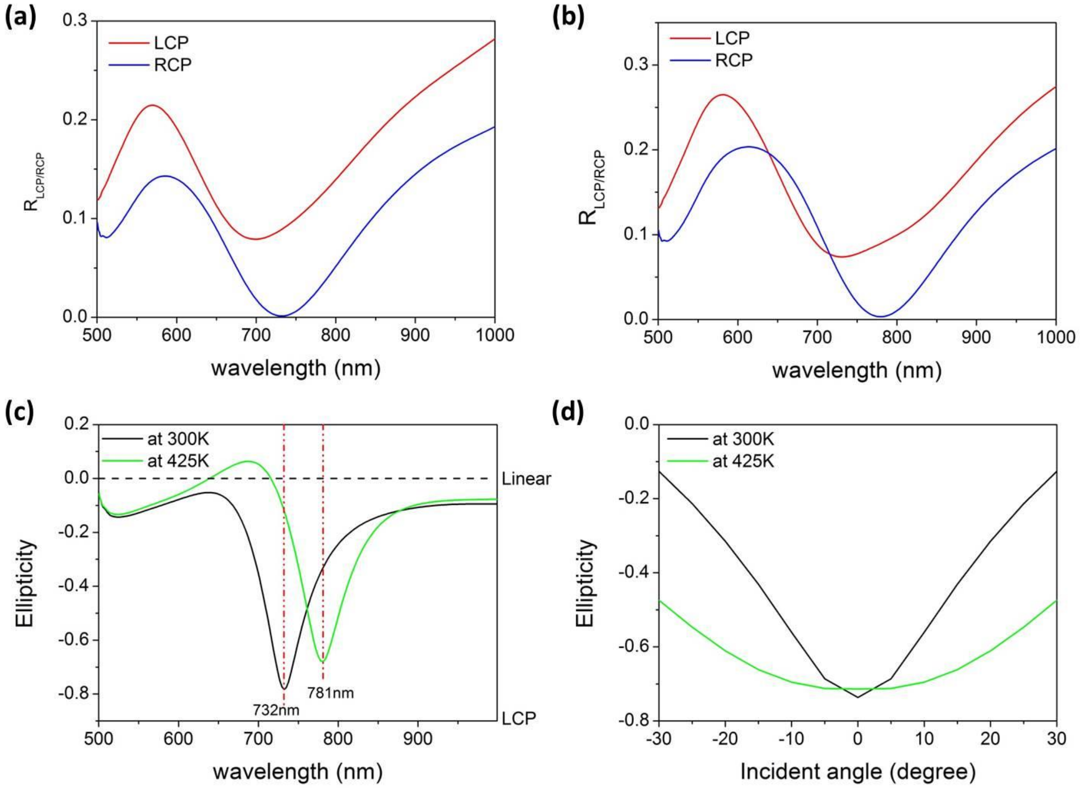

Fig 3-5 Reflection of RCP and LCP light with incident wave linearly polarized at 45 degree to x axis for hybrid nano-cross structure (a) at 300K (amorphous) and (b) at 425K (crystalline). (c) Ellipticity of polarization of reflected light with normal incident wave linearly polarized at 45 degree to x axis for hybrid cross nanostructure at 300K (amorphous) and 425K (crystalline). (d) Ellipticity of polarization of reflected light with titled incident wave at working wavelength marked in (c), 732nm for amorphous state at 300K and 781nm for crystalline state at 425K, respectively.

Ellipticity =1 refers to RCP, ellipticity = -1 refers to LCP and ellipticity = 0 refers to linear polarization, as shown in Fig 3-5 (c). At 300K, as the GST is in amorphous state, the ellipticity is about -0.75 at 732nm, which means that the energy ratio of LCP light in total reflected light R_{LCP}/(R_{LCP}+ R_{RCP}) could reach 98%. When the temperature is heated up from room temperature to 425K, GST is switching to crystalline state, and the ellipticity changes to -0.09, which means a linear reflected light. So the reflected light at this wavelength is LCP for nanostructures with amorphous GST and linearly polarized with crystalline GST. On the other hand, the ellipticity is -0.68 with crystalline GST at working wavelength of 781nm, so the energy ratio of LCP light in total reflected light is also over 95%. While GST is in amorphous state, the performance of QWP is largely reduced. With the ultra-fast phase transition of GST [159], this meta-surface can efficiently control the polarization of output lights, switching between circular and linear polarization states.

In addition, we have investigated the incident angle dependence of this MMQWP. As shown in Fig 3-5 (d), the incident angle varies from -30 degree to 30 degree, keeping the polarization angle at 45 degree. At room temperature, at the working wavelength of 732nm, the absolute value of ellipticity drops rapidly (black curve), the meta-surface fails to work as a QWP with large incident angle. However, when the GST is crystallized at 425K (green curve), the meta-surface presents a much better tolerance. The absolute value of ellipticity can still keep around 0.5 with incident angle of ±30 degree. The large difference in incident angle dependence of meta-surface with GST in difference phase states may also contribute to active manipulation of light polarizations.

In summary, we have numerically demonstrated an ultrathin active MMQWP in visible/infrared range using asymmetric cross shape Au-GST hybrid meta-surface. The refractive index of GST layer between Au nanostructures can be controlled by switching the phase states. At 732nm in visible light, the nanostructure with amorphous GST is a reflective QWP with very high polarization converting ratio, changing linear incident light to circular polarized reflections; while it still keeps the linearity of polarization unchanged with crystalline GST. And at 781nm in near-infrared light, the nanostructure with crystalline GST can also work as QWP, while that with amorphous GST does not work so well. Furthermore, the MMQWP exhibits a much better incident angle tolerance with crystalline GST than with amorphous GST. This switchable phase-change meta-surface provides a promising way for realization of polarization manipulating components, enabling novel applications with integrated optical devices.

3.3 Plasmonic QWP in THz range

In last section, a switchable MMQWP at the boundary of visible and near-infrared light was presented. One of the most important problems of plasmonic QWPs in visible and near-infrared light is the large Ohmic loss, for example, the total efficiency at working wavelength of the QWP in last section is just about 10% even though it is in reflective mode. If the nanostructure was designed in a transmitted mode, the efficiency might be even lower. This problem can be solved in a large extent in THz regime, where metals are more closed to perfect electric conductor (PEC) and the loss could be much lower. In addition, the fabrication of meta-surfaces in THz is much easier than those in visible light, since the THz structures can be about thousands of times larger than those for visible light (usually hundreds of micrometers vs. hundreds of nanometers).

On the other hand, optical devices, such as QWPs, with meta-surfaces are of great importance in THz. In particular, information conveyed by the polarization state promises applications for sensitive detection of explosive materials, THz imaging and THz wireless communication. And conventional QWPs with natural birefringent materials could be at least a few millimeters thick [24], which is difficult to be integrated into ultra-compact THz optical systems. Therefore, QWPs based on ultra-thin meta-surfaces can efficiently overcome the difficulties in bulky size and compact integration.

3.3.1 An ultrathin THz QWP using planar Babinet-inverted meta-surface

In this section, we will report a cooperative project with Wang Dacheng and etc., in which an ultrathin THz QWP for polarization control based on planar Babinet-inverted meta-surface is demonstrated. I have done the simulation for structure designing and Wang Dacheng has done the fabrication and measurement. The QWP is constructed by arrays of asymmetric metallic cross apertures, according to the Babinet's principle which states that the diffraction pattern from an opaque body is identical to that from a hole of the same size and shape except for the overall forward beam intensity, the Babinet-inverted cross apertures can support two orthogonal resonant modes in THz range. Each resonant mode gives rise to EOT effects accompanied by a specific phase shift at the resonance. It only allows the resonant wave to pass through, which eliminates the interference of the non-resonant waves. According to the dispersion equation of surface plasmon in metallic slots, the propagation constants as well as the phase delays are tunable by varying the width and length of the slots [166, 167]. By properly choosing the size of the asymmetric cross aperture, two resonant modes superpose with each other, producing equal transmitted amplitudes with a phase difference of $\pi/2$ at a certain frequency and operating as a THz QWP. A simple Lorentz oscillator model is also employed to analytically describe the performance of the QWP, which is in good agreement with the experimental and simulation results.

3.3.1.1 Simulation

To accurately design the dimensions of the asymmetric cross aperture, we investigate the transmittance and the transmitted phase delay of rectangular slots on metal film first. For narrow cross apertures, the coupling of resonances along different arms of the cross can be neglected, so the transmitted intensity and phase in x and y direction can be adopted from those of slots, respectively. In Fig 3-6, FDTD simulation results of transmittance and the transmitted phase delay of slots with different length L are presented. The width of slots is 6μm, the thickness of metal film is 5μm and the periodicity of unit cell is 150μm. The metal film is set as Cu and the substrate is polyethylene naphthalate (PEN).

To design the length of slots, we just need to find out two length data with the same transmittance in Fig 3-6 (a) and with a phase difference of π/2 in Fig 3-6 (b) at the same working frequency. Advanced optimization can be done to get higher transmittance to improve the efficiency of QWP. Synthetically, the arm lengths of the cross aperture is decided to be L_x=105μm and L_y=125μm.

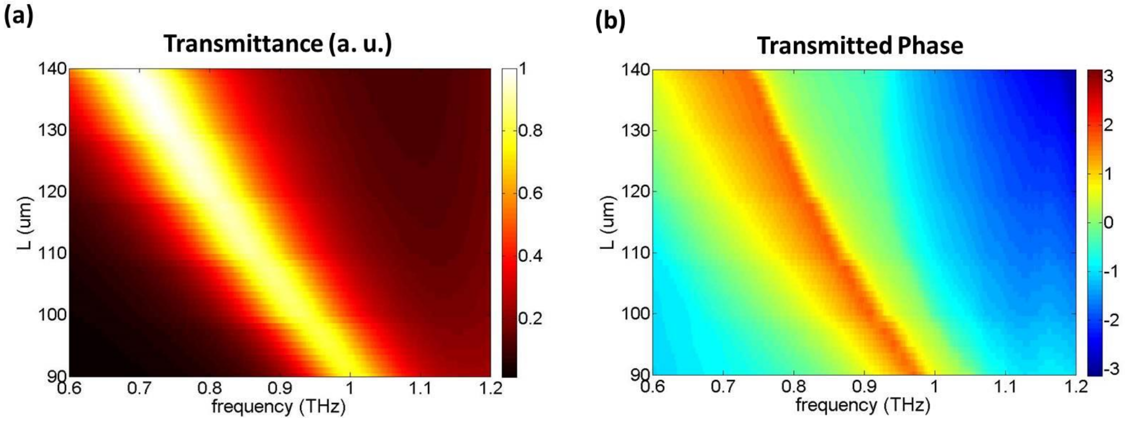

Fig 3-6 (a) The normalized transmittance and (b) transmitted phase delay of Babinet-inverted rectangular apertures with different length.

3.3.1.2 Analytical model

To better understand the physics behind the THz QWP with Babinet-inverted cross metasurface, a Lorentz oscillator model was employed to analytically describe the transmitted amplitude and transmitted phase delay. Based on Babinet's principle, a slot antenna can be depicted by a Lorentz oscillator model similar to a rod antenna [168]. We can assume in our THz QWP the apertures harmonically oscillate along the incident electric field and present a transmission peak in far field. For x-polarized incident wave, the transmitted amplitude can be described as [43]:

$$\ddot{t}_x + \gamma_x \dot{t}_x + \omega_{0x}^2 t_x = g_x E_x e^{i\omega t} \tag{3.5}$$

where t_x and γ_x are the amplitude and damping rate of transmitted electromagnetic field. g_x is the geometric factor, revealing the coupling between the resonator and the incident electromagnetic field. ω_{0x} is the fundamental resonance frequency of the aperture and $E_x\exp(i\omega t)$ is the incident electromagnetic field. And the transmitted amplitude t_x and phase delay φ_x can be described as:

$$\begin{aligned} t_x &= \frac{g_x E_x}{\sqrt{\left(\omega_{0x}^2 - \omega^2\right)^2 + \omega^2 \gamma_x^2}} \\ \tan\varphi_x &= \frac{\omega \gamma_x}{\omega_{0x}^2 - \omega^2} \end{aligned} \tag{3.6}$$

Similarly, transmitted amplitude t_y and phase change φ_y can be obtained when the incident electromagnetic wave is y polarized. When the incident electromagnetic wave is polarized at θ degrees to x axis, the total output electric field can be treated as a superposition of two orthogonal components. Based on simulation results, the damping rate and geometric factor can be fitted as $g_x = 3.26$, $g_y = 3.66$ and $\gamma_x = \gamma_y = 0.75$ THz for $L_x = 105\mu m$ and $L_y = 125\mu m$.

3.3.1.3 Experimental results

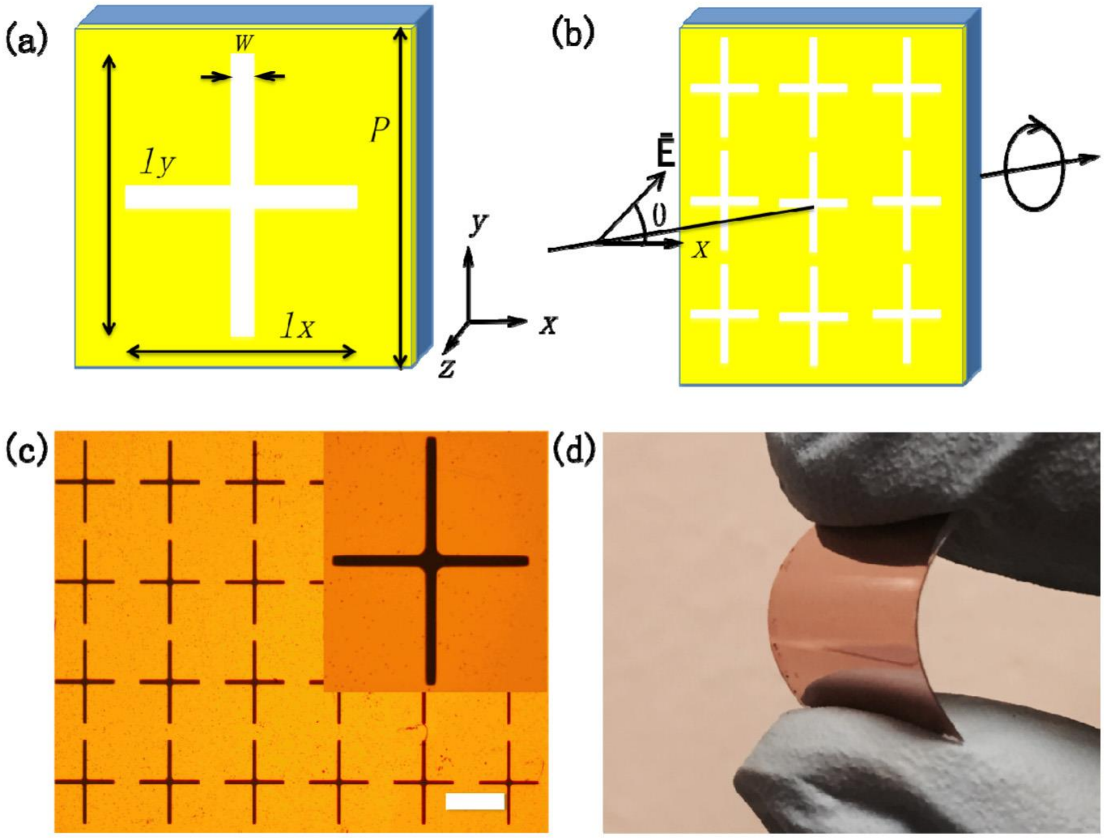

Fig 3-7 (a) Schematic of one unit cell. (b) Schematic of working principle of the QWP. The normal incident THz wave is polarized at θ = 45 degrees to x axis. (c) Microscope image of the fabricated asymmetric cross apertures with a zoomed image as the insert. The scale bar is 100 μm. (d) Photograph of the fabricated THz QWP.

The fabrication of the QWP sample and the characterization of its performance are done by Wang Dacheng. The schematic and image of the sample is shown in Fig 3-7. During the measurement, the incident THz wave was polarized at θ = 45 degrees to the two slots in the QWP. The measured amplitude transmission of the QWP along x and y direction and the phase difference between two orthogonal slots are shown is Fig 3-8 (a) and (d). From the measured results, two resonant peaks at 0.806 and 0.925 THz were observed, which correspond to fundamental resonant modes with x and y polarized incident light. The superposition of these two peaks presents an equal transmitted amplitude of 0.545 at 0.870 THz along both x and y directions. The measured phase difference between x and y directions is around π/2 at 0.870 THz as well. These indicate that the incident linearly polarized THz wave is converted into a circular polarized THz wave at 0.870 THz. The

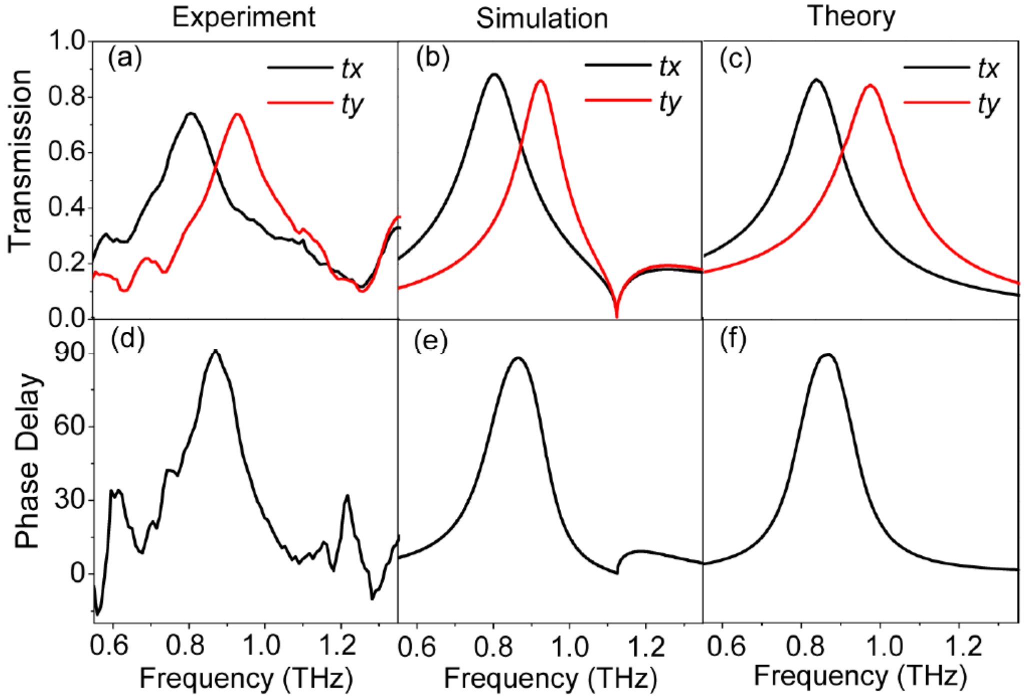

Fig 3-8 (a) Measured, (b) FDTD simulated and (c) analytical model calculated transmission and phase delay between two resonant modes for (d) experimental, (e) simulation and (f) theoretical results.

simulated and analytical amplitude transmission and phase difference are shown in Fig 3-8 (b), (e) and (c), (f), respectively. In simulation, at 0.874 THz, transmitted amplitude of 0.628 with a phase difference of around π/2 is presented, which is in good agreement with the experimental results. The resonance frequency is slightly shifted and the amplitude is a bit suppressed in experiment comparing to the simulation, which might results from the reduction of metal film thickness, size fluctuation in fabrication and the loss in metal film and substrate.

Then the ellipticity of the transmitted wave have been measured and simulated, as shown in Fig 3-9. The Stokes parameter S_0 is calculated as $S_0 = (|E_x|^2 + |E_y|^2)/ |E_0|^2$, which is the output electric field power. At 0.870 THz, the QWP presents an output power of 0.297 in

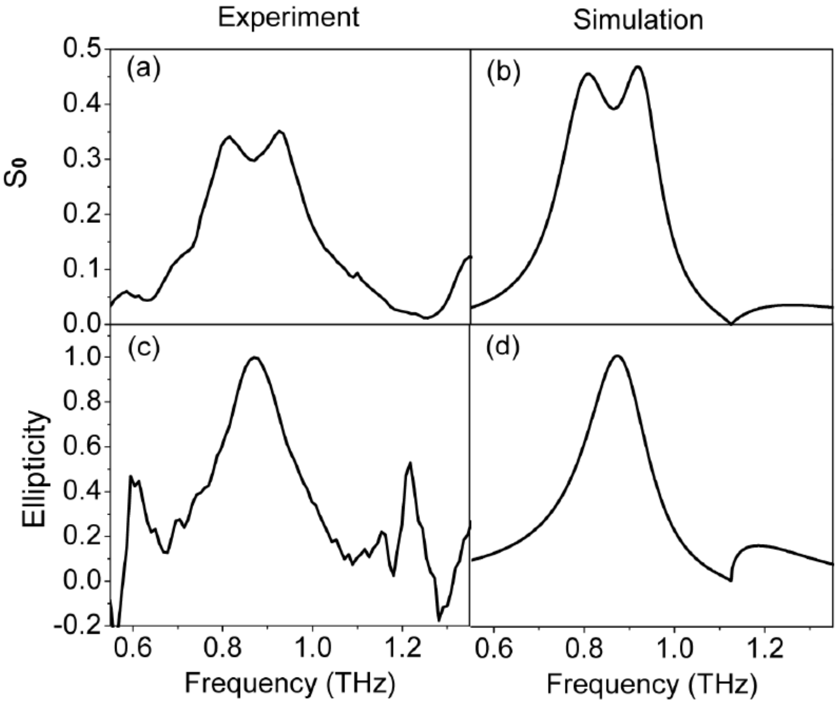

Fig 3-9 (a) Measured and (b) simulated Stokes parameter S_0, and calculated ellipticity for (c) experiment and (d) simulation.

experiment, while in simulation the output power is 0.394 at 0.874 THz, which is much higher than similar plasmonic structures in visible and near-infrared range. In the experiment, the ellipticity at 0.870 THz is 1, indicating the output THz wave is a perfect LCP light. The simulated ellipticity presents similar results with 0.999 at 0.874 THz. The simulation and experiment results are in good agreement with each other. Therefore, this ultrathin device shows good performance as a THz QWP, and it opens up avenues for new functional terahertz devices design.

3.3.2 Switchable ultra-thin THz QWP using active phase-change meta-surface

In this section, we will present a further extending research of the ultra-thin THz QWP in last section, making the QWP active and switchable by introducing the phase-change material, VO_2, into the meta-surface. Fig 3-10 (a) shows the schematic of the switchable QWP, which is composed of ultrathin asymmetric cross-shaped resonator arrays with VO_2 pads inserted at the end of the cross-shaped resonators. The geometrical parameters are P=150 μm, L_x=90 μm, L_y=124 μm, l_x=9 μm, l_y=5 μm and w=9 μm, respectively. The birefringence is generated by the difference between the arm lengths of the cross. The switching property of the QWP is controlled by a resistive heater as a proof of concept to manipulate the VO_2 phase transition at different temperatures, which can also be realized by optical pumping [169]. At 300K, VO_2 behaves as a semiconductor, while at 400K, its electrical conductivity significantly increases from 140 S/m to 5×10^5 S/m and changes to a metal phase, as shown in Fig 3-10 (c). Therefore, the inserted VO_2 pads can change the effective lengths of the cross arms at different temperatures.

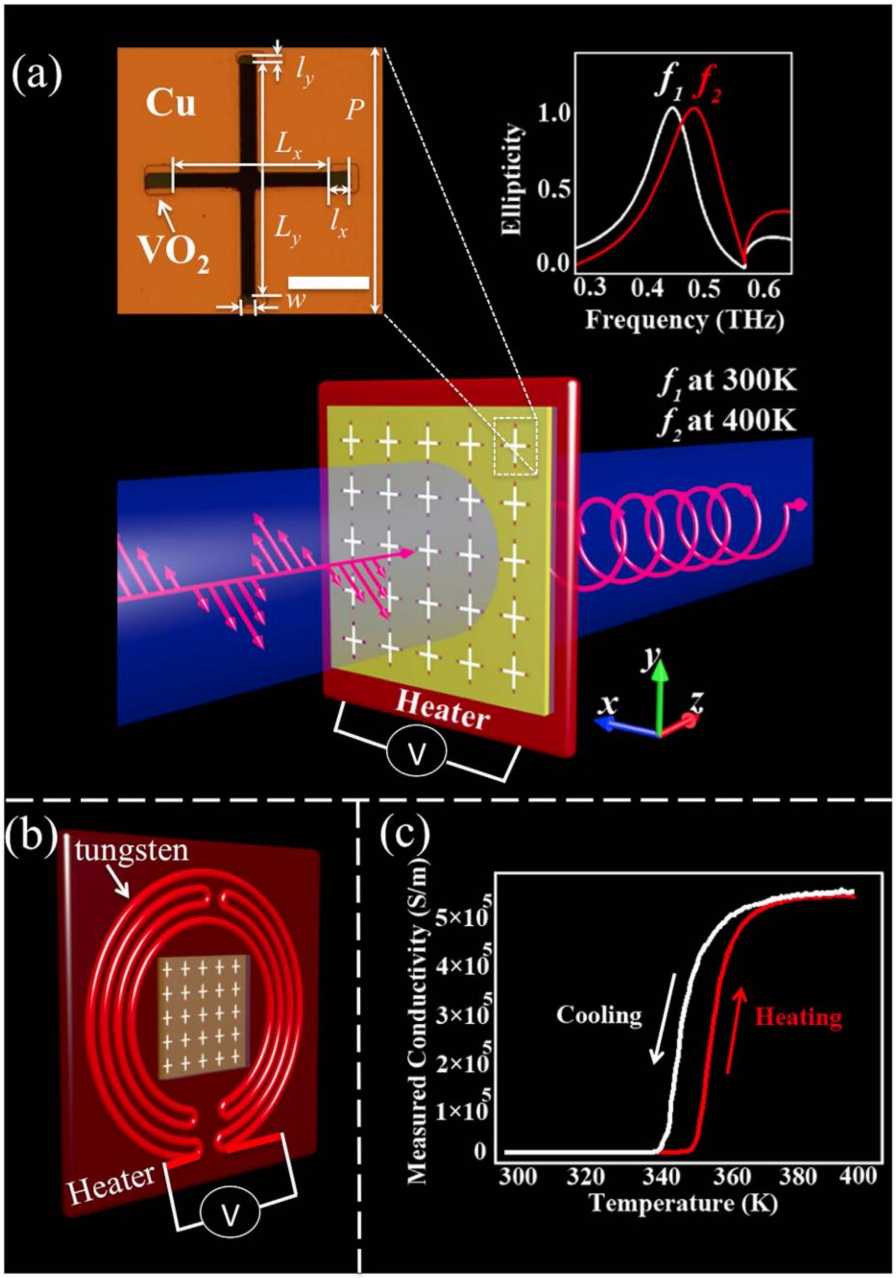

Fig 3-10 (a) Experimental switching schematic of the THz QWP. The top left inset is a microscope image of one unit cell in the fabricated samples. The scale bar is 50 μ m. The top right inset is the simulated ellipticity of the output THz waves, indicating that at both f_1 and f_2 the output THz waves are circularly polarized. (b) Schematic backside view of the resistive heater with a square aperture (6×6 mm^2) milled at the center to allow THz to pass through. (c) Measured electrical conductivity of fabricated VO_2 films at different temperatures during the heating and the cooling cycles.

By properly design of the geometrical parameters, this meta-surface can work as QWP at different frequency at corresponding temperature. Fig 3-11 shows the measured transmission coefficients and phase delays of THz QWP before and after the VO_2 phase transition. In experimental results, at 300 K, the QWP presents a transmission coefficient of 0.59 at 0.468 THz and a phase delay of 80 °between y and x axes, which means the incident linearly polarized THz wave is converted into a circularly polarized wave. When the QWP is heated to 400 K, the VO_2 phase transition changes the performance of the QWP. As it can be seen, a transmission coefficient of 0.28 at 0.502 THz and a phase

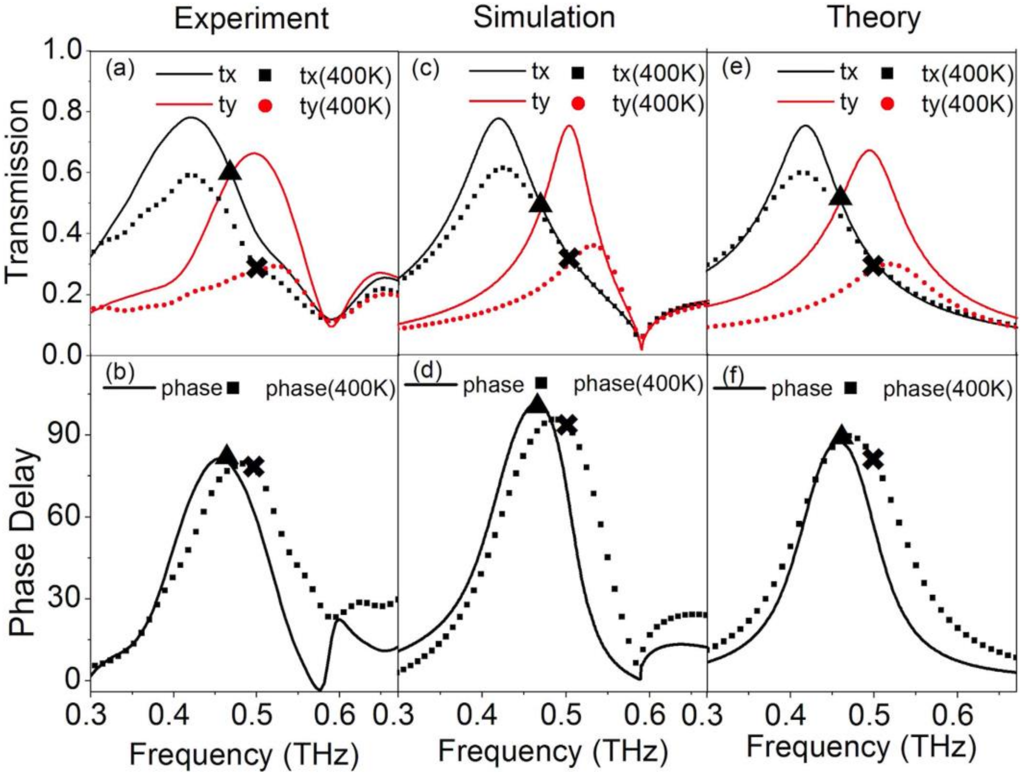

Fig 3-11 (a) Measured transmission spectra along two slots at 300K (solid line) and 400K (dot line). (b) Measured phase difference between y and x axes at 300K (solid line) and 400K (dot line). The inserted triangle indicates at 300 K, the transmission coefficients along two axes are the same, while their phase difference is close to 90 °. The marked cross shows similar results at 400 K. (c) Numerically simulated transmission spectra with the corresponding phase delay (d) based on different measured VO_2 electrical conductivities. (e) Analytical fitted transmission spectra and (f) the corresponding phase delays, according to the analytical model in section 3.3.1.2.

delay of 75 °between y and x axes are obtained. Therefore, the THz QWP is able to switch its operating frequency with a switching range of 34 GHz. One thing to note is that experimental phase delays at both 300 and 400 K are smaller than 90 °, due to the size fluctuation in the fabrication process and the damping effect in the fabricated samples. To compensate the phase difference and obtain a perfect circularly polarized output THz wave in experiment, the optimized parameters in simulation should give a phase difference larger than 90 °.

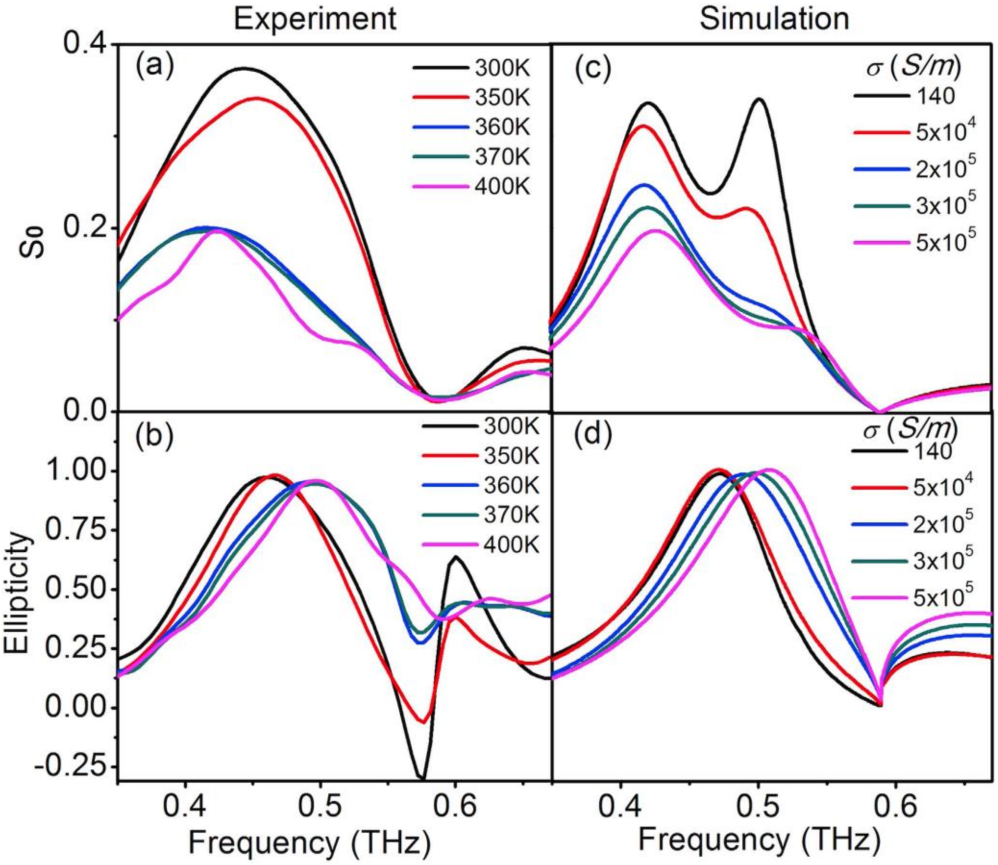

Fig 3-12 (a) Calculated Stokes parameter S_0 with respect to different temperatures based on measured results, indicating that the output power decreases when the temperature increases. (b) Measured ellipticity of the output THz wave at different temperatures, indicating the operation frequencies switching of the output circularly polarized THz wave. (c) Numerically simulated Stokes parameter S_0 with respect to different conductivities of VO_2 and (d) the corresponding ellipticity of the output THz wave.

To directly evaluate the performance of the QWP, the measured and simulated Stokes parameter S_0 and ellipticity of the output wave at different temperature (with different conductivity in simulation) is shown in Fig 3-12. It is observed that when the temperature increases from 300 to 400 K, the output power decreases. This is because of the increasing loss in the VO_2 pads. At 300 K, the VO_2 pads behave as a semiconductor and the corresponding loss is low. When the temperature increases, free carries in the VO_2 pads increase, leading to a high damping loss and small output power. In experimental results, at 300K, the ellipticity of the output THz wave is around 0.98 at 0.468 THz; at 400 K, the ellipticity is around 0.97 at 0.502 THz. Between 300 and 400 K, the ellipticity is close to 1 with the operating frequency shifting from 0.468 to 0.502 THz, which agrees quite well with the simulation results. This indicates that the output THz wave is circularly polarized at different temperatures.

In summary, by hybridizing meta-surfaces with VO_2, an ultrathin switchable THz QWP with a switching range of 34 GHz is demonstrated. The inserted VO_2 is able to change the effective length of the aperture resonators on metal film through the phase transition. At 300K, VO_2 behaves like a semiconductor and the THz QWP operates at 0.468 THz. While at 400K, VO_2 acts as a metal and the operating frequency of the QWP is switched to 0.502 THz. The simulation and analytical fitted results are in good agreement with the measured results. This switchable phase-change meta-surface promises a new route for active THz polarization manipulation devices and can be applied to other ultra-thin tunable devices.

Chapter 4 Direct Excitation of Dark Plasmonic Resonances in Visible Light at Normal Incidence

4.1 Introduction: excitation of dark modes on plasmonic nanostructures

In Chapter 2 and Chapter 3 we have reported our works on manipulation of intensity and polarization of EMWs, which can be observed in far-field. In very fundamental sense, these applications origin from engineering resonances of nanostructures. To better manipulate light, we need to better understand and utilize the resonance. Therefore, the fundamental of some specific plasmon modes is also worthy investigating. One of the interesting phenomena is the dark plasmon resonance modes. Dark plasmon resonances are charge oscillations localized on metal nanostructures that are weakly radiating and thus difficult to excite by light. In coupled plasmonic systems, these dark modes can be considered as a combination of multiple dipole resonances that collectively sum to zero. For example, in free space two parallel asymmetry dipoles can form a quadrupole with zero dipole momentum, which will be response to the momentum of incident wave (when the polarization of wave is parallel to each dipole), therefore cannot be excited. Dark modes have small scattering cross-sections and are thus difficult to excite directly by light at normal incidence.

Generally, on plasmonic structures like nano-disks, dimer or clusters, dark modes can be excited by utilizing electron beams [170-173], which can be observed by electron energy loss spectroscopy (EELS). These modes are also sensitive to the position of electron beam excitation point. In optical method, the conventional ways to excite dark modes are to generate asymmetry, including 1) asymmetry in source: with oblique incident light [174-176], dark modes can be excited on nano-particles, disks or ring because of the phase retardation; 2) asymmetry in near-field environment [177]; 3) most commonly, asymmetry in structures, for instance, heterogeneous dimers and clusters [178-182], dolmens [179, 183-185], and stacks [68, 186-188]. In these asymmetric nanostructures, the mechanism to excite dark modes is introducing Fano resonance. In general, a bright dipole resonance is excited first as the excitation source of the dark modes and thereby results in weak absorption.

In practical application, one of the major characteristics of dark modes is their narrowband absorption. In the case of color filters and printing applications, this narrowband feature may lead to purer color selections. In refractive-index sensing and single-molecule sensing [175, 180-182, 185], the narrowband resonance of dark modes can provide high sensitivity. As most of these applications require normal incidence and strong absorption, it is valuable to design structures that allow normal incidence to directly excite dark modes. In the following sections, we will introduce an idealized design of a novel symmetry structure consisting of a continuous metal coating on dielectric nano-pillars. Our analysis and numerical simulations of this structure will show the presence of narrowband dark modes that can be effectively excited to produce perfect absorption of normally incident light.

4.2 New methods to excite dark modes

As mentioned in last section, conventional optical methods to excite dark modes are utilizing asymmetry of incidence, environment and nanostructure, or indirectly exciting by an intermediate bright dipole mode. It is hard to directly excite plasmonic dark modes by electromagnetic field coupling on symmetric nanostructures with normal incident light. In this chapter, we provide a novel method to conquer this problem, in which the plasmonic dark modes are distinguished from previous research works.

Firstly, we take a review of the plasmonic nanostructure consisting of metal nano-disks on dielectric nano-pillars with a bottom back reflector plane [8], which had been discussed in section 2.2.3. The top disks provide LSPRs and the back reflector provides SPPs, and the height of the dielectric pillars determines the coupling between them. These nanostructures exhibit a broad range of colors when viewed in reflection mode under bright-field illumination in an optical microscope. Reflectance peaks were observed at wavelengths corresponding to the dipole resonances of the nano-disks and the interplay between resonances of the disk and the back reflector. Of course these modes are bright modes, but based on a small modification of this kind of nanostructure, we had demonstrated new optical dark modes, with a sharp reflectance dip in the spectra, overlaying the broader peaks in the original structure. By merely introducing a continuous 5-nm-thick Ag coating on the sidewalls of the nano-pillars, the top disk is in effect electrically shorted with the bottom back reflector layer. Although this sidewall is thin, it is still not thin enough to consider the nonlocal effects as a shell with large inner radius. Reminiscent of the effects of conductive bridges across closely-spaced metal structures [189, 190], our introduction of this conductive sidewall coating gives rise to new resonant modes. These resulting dark modes with quadrupole and higher-order multipoles are a consequence of the cancellation of the dipole of the nano-disk by dipoles of opposite polarity supported on the sidewalls, resulting in narrow-band perfect absorption. The metallic surface of this periodic pillar nanostructure is overall continuous. In contrast to the electromagnetically induced dark modes reported thus far in the literature [68, 174-188], we present the following three contributions. Firstly, the dark modes are directly excited without the need of using intermediate induced bright mode; this markedly improves the excitation efficiency of dark modes. Secondly, our proposed scheme (of excitation with normal incidence on continuous plasmonic metallic surface, in Fig 4-1 (a) and (b)) can be regarded as an electrical resonant method to induce dark modes by creating and manipulating the electric charges on the shorting sidewalls where the electric current behaves as a standing wave; this is different from the other reported methods employing, for example, oblique incidence, stacked or planarized heterogeneous structures, which rely on electromagnetically induced coupling. Thirdly, owing to this slight but non-trivial modification on the sidewall, a broad-band highly-reflective resonator is transformed into a narrow-band perfect absorber supporting quadrupole and even higher-order modes.

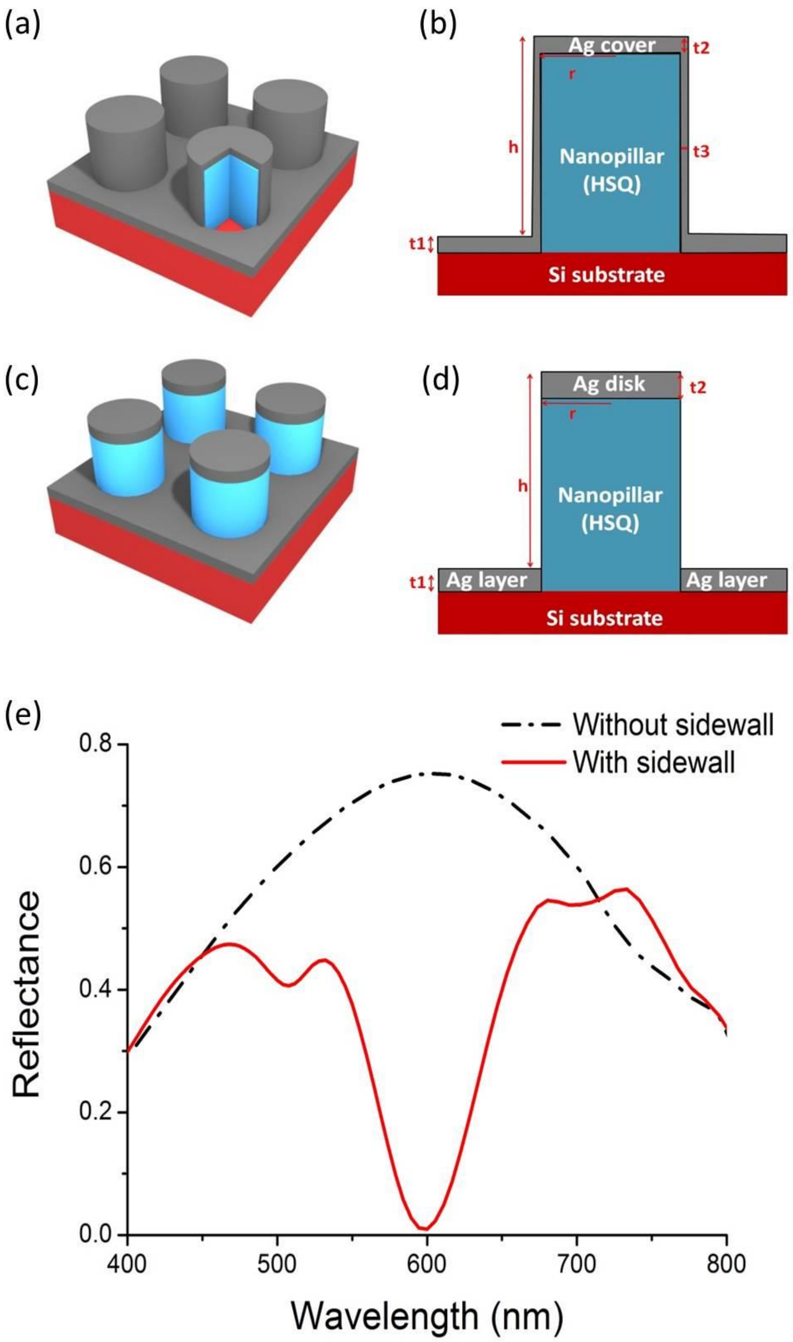

Fig 4-1 (a) Schematic diagram of the periodic HSQ pillars covered by Ag layer structure. (b) A cross-sectional view of the unit cell in (a), t_1=t_2=15nm, t_3=5nm, r=50nm. (c) Schematic diagram of the periodic HSQ pillars without Ag sidewall. (d) A cross-sectional view of the unit cell in (c), t_1=t_2=15nm, r=45nm. (e) The reflection spectrum for the structure with Ag sidewall (shown in (a), (b)) and without sidewall (shown in (c), (d)), h=85nm, p=120nm, p is the period of unit cell, h is the height of pillar from the Ag bottom-layer, and g is the gap between two neighbor pillars, p=2r+g.

4.3 Proposed design

Portrayed in Fig 4-1 (a) and (b) is our proposed structure comprising a periodic array of dielectric HSQ pillars covering by ultrathin Ag layers on a Si substrate. The covering of HSQ pillars is anisotropic, the thickness of the Ag layer on top of the HSQ pillars and

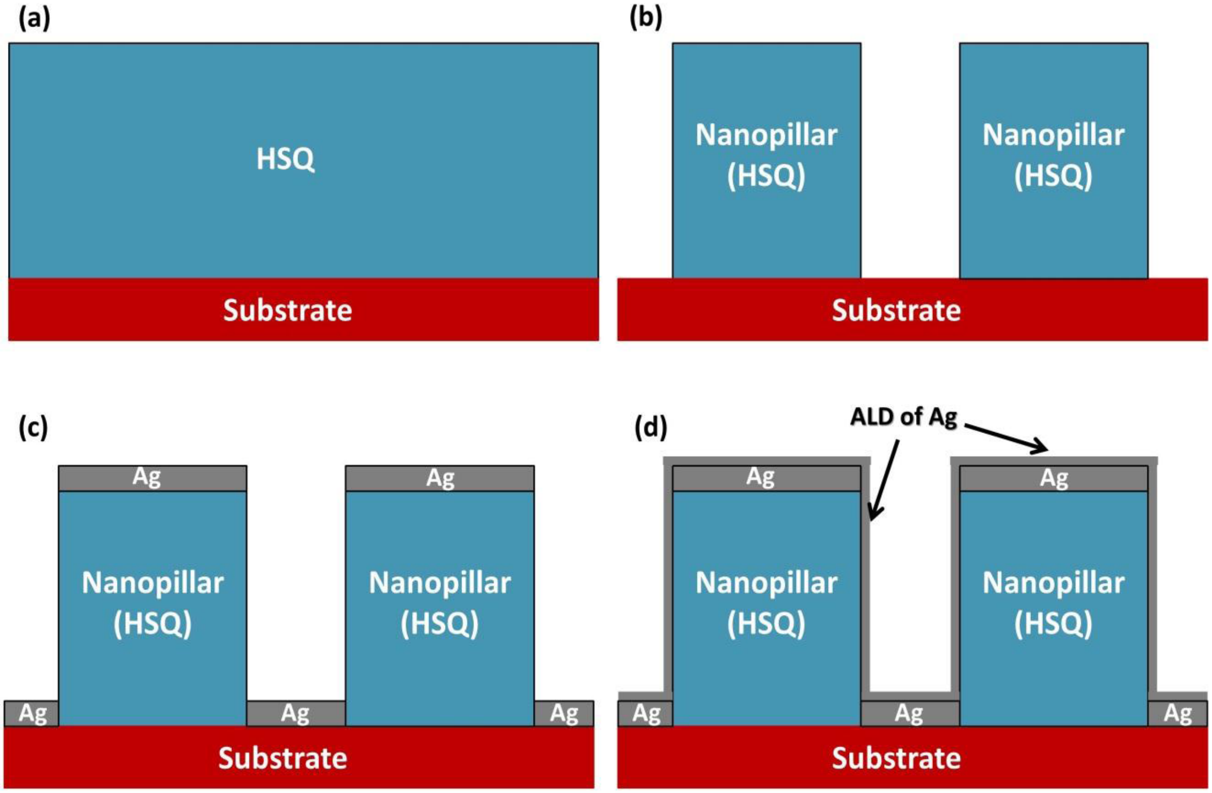

Fig 4-2 The Schematic diagram of proposed fabrication process: (a) Negative-tone HSQ spin-coated onto substrate. The thickness of the HSQ layer is 85nm. (b) HSQ nano-pillars after EBL. The unexposed portions of the HSQ are developed away using a salty developer, leaving HSQ nano-pillar array. (c) A layer of Ag is deposited onto the samples using an electron-beam evaporator. The Ag layer is about 10nm and covers the top of HSQ pillars and the blank area on the substrate, leaving the side of pillars bare. (d) Another 5nm Ag layer is coated cover the whole structure by ALD. The gray area in black frame represents the Ag deposited in process (c). After ALD the top/bottom Ag layer is 15nm and the sidewall is 5nm.

bottom-layer is 15nm, and the thickness of the Ag sidewall around the HSQ pillars is 5nm (which is much thinner than the penetration depth of Ag at visible light). Since the thickness of the top/bottom Ag layer and the sidewall is different, a 2-step method is proposed to deal with the metal deposition, as shown in Fig 4-2. Firstly, by using an electron-beam evaporator, a layer of Ag can be deposited on the top of HSQ pillars and at the bottom (Fig 4-2 (a)—(c)), which is similar to the structure in Fig 4-1 (c) and (d), but the thickness of this layer is about 10 nm. Secondly, another 5 nm Ag layer covering the whole structure (containing the top/bottom layer and the sidewall around pillars) can be added by Atomic Layer Deposition (ALD) [191, 192]. After that the Ag layer on top and bottom had increased to 15 nm and the sides of HSQ pillars are coated with 5 nm Ag sidewalls (Fig 4-2 (d)). Such a thin Ag sidewall allows the energy to flow into and out of the structure easily whilst still electrically connecting the top disks and bottom layer. This also makes our structure different from the pure metal pillars array [193] which blocks the electromagnetic wave outside the pillars.

4.4 Results and analysis

4.4.1 Generating dark mode

Fig 4-1 (e) shows the reflection spectrum of a wave at normal incidence. While the nanostructure is opaque with Si substrate, the reflection spectrum can also indicate the absorption. For comparison purposes, we also include a similar structure of the same size but without the 5 nm Ag sidewall in Fig 4-1 (c) and (d). For the structure without the Ag sidewall, there is a broadband peak in the visible light range. In contrast, the reflectance of our proposed structure drops to nearly 0 at 600 nm. Given that the structures sit on a Si substrate, the transmittance of the structure can effectively be neglected and the reflectance dip thus indicates absorptance instead. Hence, the thin Ag sidewall coating transforms this structure from a broad-band reflector to a narrow-band near-perfect absorber.

For the reflection spectrum, the broad-band peak of the structure portrayed in Fig 4-1 (c) and (d) results from the coupling of LSPR of the Ag disks on top of the HSQ pillars and the SPP of Ag bottom layer on the substrate [8]. However, the Ag sidewall serves as a bridge connecting the top disks and the bottom layer, and the top disks thus cannot be regarded as simple dipoles. As can be seen from the plots in Fig 4-3 (a) depicting the charge distribution at resonance, the charge can be pumped into the sidewall by the resonance of the top disk and a plasmonic standing wave will then be generated along the sidewall. The charge is accumulated at the edge of the top disk while remaining zero at the bottom. At the antinode of the standing wave in the middle of the sidewall, however,

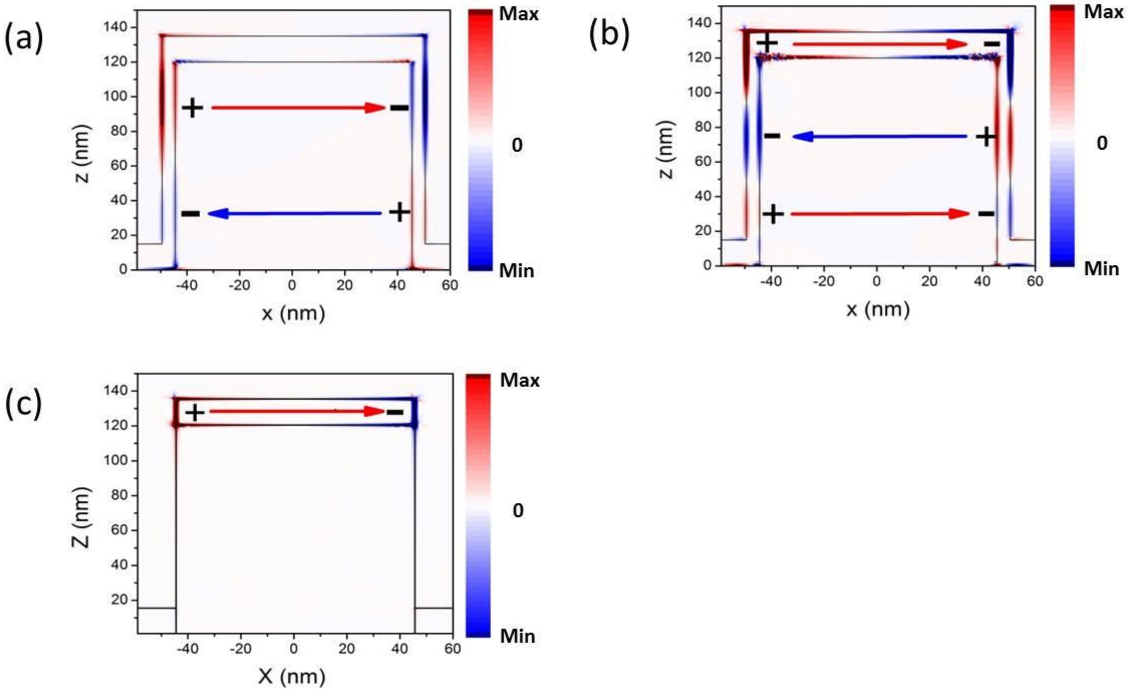

Fig 4-3 Higher-order dark modes excited by visible light. (a) The charge distribution for an excited quadrupolar dark mode at a wavelength of 600 nm, with h = 120 nm, p = 120 nm. (b) The charge distribution for a hexapolar dark mode at a wavelength of 569 nm, with h = 120 nm, p = 120 nm. (c) For comparison, the charge distribution for bright dipole mode resonance of the structure without a sidewall shown in Fig 4-1 (c) and (d). The signs and arrows denote dipoles and their directions. It should be pointed out that some of the area with extremely large charge density has been smoothed; the highest intensity has been suppressed in order to maintain the contrast.

charge is accumulated and forms another horizontal dipole in the middle of the sidewall; this is opposite to the dipoles of the top disks and the charge profile on the metal covering the pillar and thus constitutes a quadrupole (dark mode) where the two sets of dipole moment nullify each other and the radiation is reduced to yield zero reflection of this nanostructure. Different from the dark modes reported for other plasmonic oscillators (e.g. in plasmonic nanoparticles or nanorods) caused by the coupling of the electromagnetic field, this dark mode in the continuous metal structure is caused by the electric current oscillation and charge accumulation driven into the ultra-thin sidewall by the bright dipole resonance of the top Ag disk. Seen from this perspective, we can regard it as an electronically induced absorption of the ultra-thin Ag sidewall (in contrast to electromagnetically induced absorption).

4.4.2 Higher order modes

In addition, we observe in Fig 4-1 (e) a minor dip at a shorter wavelength for the reflectance of our proposed structure. This is due to the same effect as explained above, but with a hexapolar mode on the sidewall of the pillar. At a wavelength of 508 nm, two more dipoles (other than the one on the top disk) are induced on the sidewall and so each pillar is effectively holding a hexapole also in dark mode, with a form of "positive– negative– positive" distribution. These high-order multipolar dark modes are suppressing the radiation and reducing the reflectance as well. In Fig 4-1 (e), this hexapolar mode is much weaker than the quadrupolar mode because the resonance wavelength of the hexapolar mode is far away from that of the top disk dipoles for the structure without the sidewall while the resonance wavelength of the quadrupolar mode is close to it. The dark modes are mainly induced by the top disk dipoles; hence, only the dark modes near the top-disk dipole resonance wavelength can be so strong. If we open a ring gap on the sidewall at the position where the charge is accumulated and the electric current is zero, the quadrupolar and high-order multipolar modes will not be affected and the spectrum near the resonance will remain almost the same; in this sense the nanostructure can be regarded as an optical flute which can absorb specific wavelengths (similar to the flute playing specific tones).

To further investigate how the structure performs as a perfect absorber, we plot the profiles of the electric field, Poynting vectors and electric current in Fig 4-4 for both quadrupolar and hexapolar modes to explain the energy absorption. From the electric field plots, we can readily determine the positions of the quadrupole and hexapole; since the entire structure has a continuous Ag cover, the power flow is squeezed into the gaps between the pillars. When the incident wavelength is at the quadrupolar mode resonance, the power flow penetrates through the Ag sidewall at the position of zero net charge and then exits at the bottom, encircling the charge like a vortex. Each time the power passes the sidewall, a large amount of energy is lost. Hence, the power flow is localized along the sidewall (either going into or out of the pillar) and then energy is lost on the sidewall. Interestingly, if the pillar is made of pure solid Ag without the HSQ core, power flow cannot freely go inside and outside the solid Ag pillars and light is thus mostly reflected. For our structure, the sidewall is thin enough for light to penetrate, which drives the power flow to encircle and flow around the accumulated charge, generating the energy vortexes along the sidewall of the pillars; it thus leads to greatly increased absorptance. A similar phenomenon can be observed for the hexapolar mode, where the charge on the Ag sidewall enforces the power flow to go “in－out－in” the pillar. Since we presume that our structure has only one type of loss (*i.e.* metallic loss in Ag), all of the absorption should take place in the Ag cover and the energy lost in Ag is proportional to the square of the electric current density. We observe from the electric current distributions for different multipoles shown in Fig 4-4 (e)–(g) that most of the energy is depleted on the sidewall at the resonance wavelength. Hence, energy is mostly lost on the ultrathin sidewall instead of the top disks or the bottom layer.

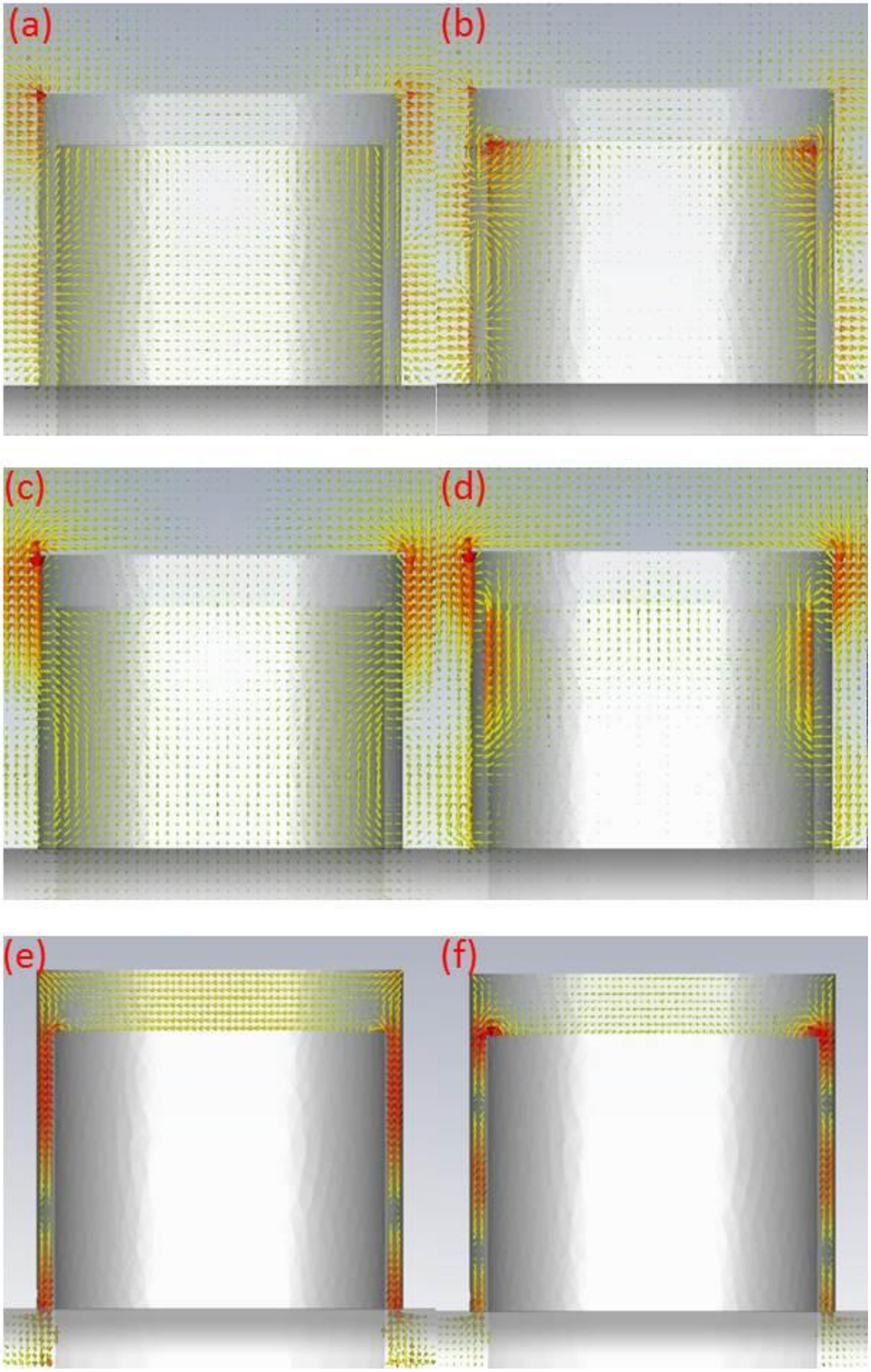
(a)
(b)
(c)
(d)
(e)
(f)

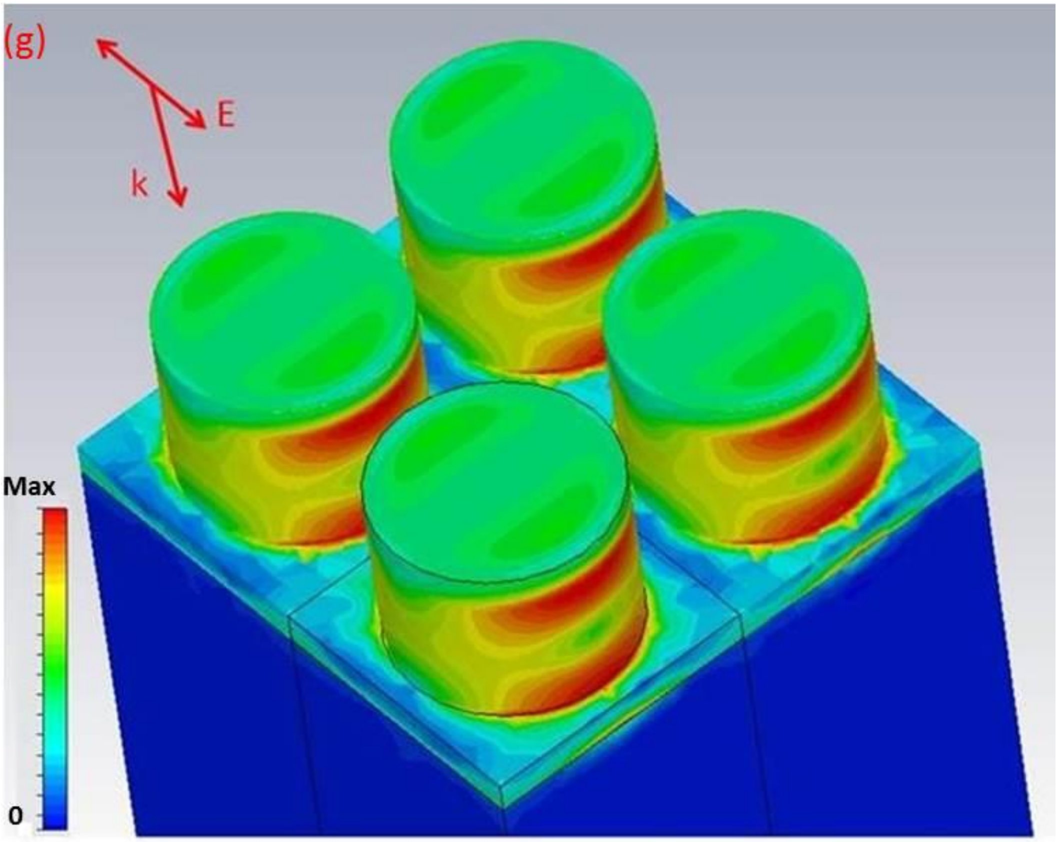

Fig 4-4 The electric-field distribution of (a) quadrupolar mode and (b) hexapolar mode. The Poynting vector distribution of (c) quadrupolar mode and (d) hexapolar mode. The electric current (J) distribution in Ag of (e) quadrupolar mode and (f) hexapolar mode. (g) 3D view of the electric-current intensity profile in log scale at quadrupolar mode; it can also indicate the energy absorption profile in which most energy is absorbed at the sidewall (dissipated energy $E \propto J^2$). The figures were simulated by CST (Computer Simulation Technology), using periodic boundary. For the structure, h = 85 nm, p = 120 nm. Both the size and the color of the arrow show the magnitude, and all intensity is normalized.

Fig 4-4 allows us to infer how each part of the structure works. The top metal disks, if separated from the other parts of the structure, can clearly be regarded as dipole resonators. However, once the thin metal sidewall is connected, the dipole mode no longer holds and the disk performs like a pump pushing the electrical current into the sidewall. We should thus focus on the 5 nm Ag sidewall when exciting dark modes.

Firstly, it electrically breaks the bright dipole mode on the disks so that there are only directly excited dark mode resonances in our structure (Fig 4-3 (a) and (b)); this is quite different from previous research on dolmen or stacked structures that utilize a bright dipole mode to excite the dark modes. Secondly, the sidewall performs as the carrier of the standing wave; our dark modes are electrically (instead of electromagnetically) induced such that it needs the metal sidewall to support the current oscillation. Lastly, the sidewall is also the energy consumer; the quadrupoles or higher-order multipoles guide the power to penetrate such an ultrathin metal layer again and again (Fig 4-4 (c) and (d)) and the energy is greatly depleted each time the power passes the sidewall (Fig 4-4 (g)). We infer from Fig 4-4 (e) and (f) that the electric current on the bottom layer is so small that we can approximately disregard it, thus implying that this Ag layer is not an important part of the structure. Indeed, it is not so necessary for supporting the standing wave on the sidewall and the incident light can hardly reach the bottom. Without this bottom layer, FDTD simulations likewise yield the similar narrowband absorption associated with the dark modes in the reflection spectrum.

In addition to using directly excited quadrupolar dark mode to achieve perfect absorption, we can equally seek to enhance the hexapolar mode so as to make this structure a dual-band near-perfect absorber targeting particular wavelengths. We infer from Fig 4-5 that the resonance wavelength and absorptance depend on the height h of the pillar. The red and green lines plotted in Fig 4-5 correspond to the quadrupole and hexapole resonances, respectively. The resonance wavelength is almost linear with h, and the slopes of both resonance wavelengths are approximately 2. When h is small, the high-order modes, such as hexapole mode, are not strong enough to be observed. The hexapolar mode can be

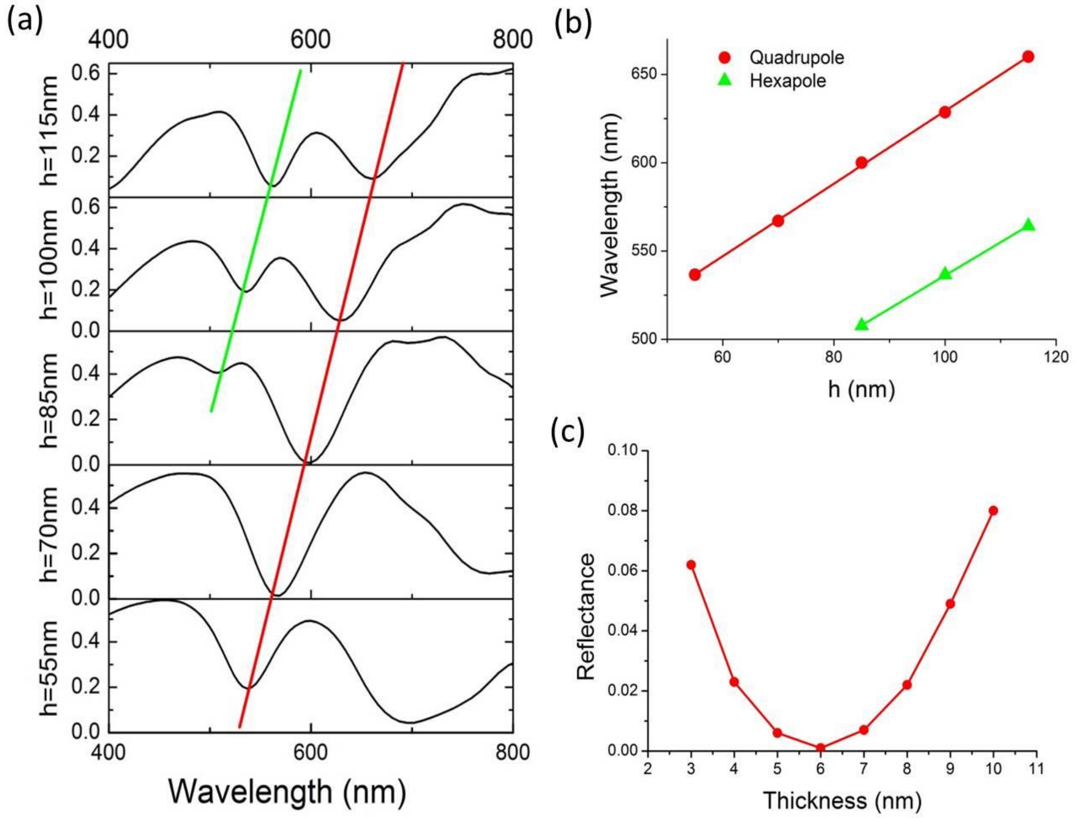

Fig 4-5 (a) The reflection spectrum of the structure with different *h*, where the red and green lines indicate quadrupolar and hexapolar modes respectively. (b) The fitting of the resonance wavelength versus *h* for quadrupolar and hexapolar modes (with slope of 2.06 and 1.88 respectively). (c) The reflectance of the quadrupole resonance dip for the structure with different Ag sidewall thicknesses, with fixed HSQ height h = 85 nm, period p = 120 nm.

easily observed when *h* exceeds 85 nm. As *h* becomes larger, it is easier to accommodate and enhance higher-order multipolar modes; for example, we observe from Fig 4-5 (a) that at *h* = 115 nm the absorption of the hexapolar mode is even more significant than that of the quadrupolar mode. It can be understood that the results show that the higher structures can support stronger hexapole modes, and when *h* is small, the hexapole mode becomes extremely weak. Although the dark mode resonances are located on the sidewall, they still need the top disk to drive the charge into sidewall. Therefore, the dark modes, no matter quadrupole or hexapole, will become weaker as they shift further away from the original resonance of the disk (about 600 nm, shown by the black dashed curve in Fig 4-1 (e), which is the resonance peak for nanostructures without sidewalls). When *h* is small, the resonance wavelength of hexapole mode would be so short, as the trend shown in Fig 4-5 (b), that the amount of charge pumped into the sidewall by the top disk would be very limited and the dark mode resonances would be too weak to be observed. In principle, for an even larger *h*, we should also be able to observe higher order modes like octupole.

4.4.3 Size toleration

In fabrication, it is very difficult to achieve a 5 nm homogeneous Ag sidewall and accurately control its thickness. By Ag evaporation, the layer may be not continuous or even patchy. So the sidewall is proposed to be deposited by ALD, but the thickness is still hard to keep uniform at such small size. To address this limitation, we also need to investigate whether this structure can tolerate variations in the sidewall thickness. Additional simulations have been performed in Fig 4-5 (c) to examine how the absorption (shown by reflectance) at the quadrupole resonance dip depends on the thickness of the Ag sidewall. The simulation results in Fig 4-5 (c) affirm that reflectance can be kept below 10% even when the thickness varies from 3 nm to 10 nm.

Another way to reduce the fabrication difficulty is to simplify the 2-step Ag deposition method into just an ALD process. After achieving the HSQ pillar array by EBL, the Ag evaporation process can be skipped, and a thin Ag cover can be directly deposited on the structure by ALD. As a consequence, the top layer and sidewall will have the same thickness ($t_1 = t_2 = t_3$ in Fig 4-1 (b)). This simplified structure can still support the dark modes, but the strength of the mode is greatly reduced; and when t_3 is increased to 10nm, the resonance wavelength also shifts, as shown in Fig 4-6. As discussed before, the sidewall should be thin enough to let the power flow penetrate into the pillar, while the top disks should be thick enough to prevent the power flow from directly going inside and guide the power flow into the gaps (see Fig 4-4 (c) and (d)). Thus, the Ag cover with the same thickness cannot satisfy both requirements perfectly at the same time, and the efficiency of dark mode excitation is reduced. And the resonance wavelength shifting of t=10nm is due to the narrowing of gap size since we keep the periodicity and the radius of HSQ pillar unchanged.

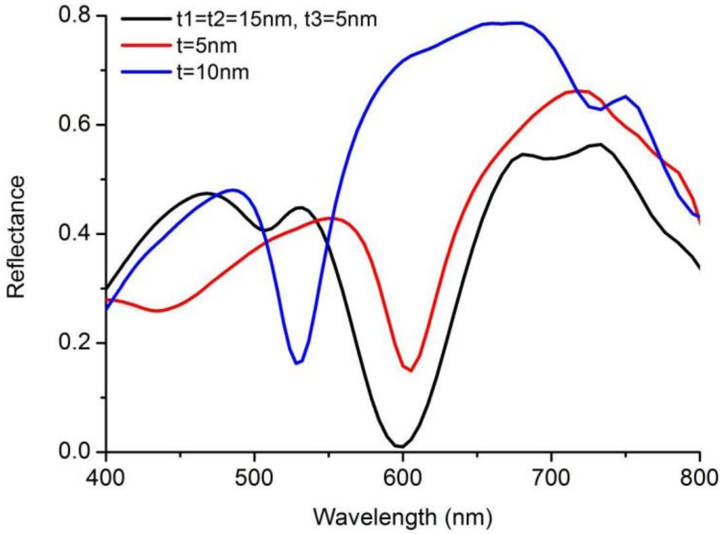

Fig 4-6 The reflectance of nanostructures proposed by (1)the 2-step deposition (black curve), in which t_1=t_2=15nm, t_3=5nm; (2) ALD of Ag with thickness of $t_1 = t_2 = t_3$ = 5nm (red curve); (3) ALD of Ag with thickness of $t_1 = t_2 = t_3$ = 10nm (blue curve). Where t_1 is the thickness of the bottom Ag layer, t_2 is the thickness of the top Ag disks and t_3 is the thickness of the Ag sidewall, as shown in Fig 4-1 (b). Height and radius of HSQ pillar is 85nm and 45nm, period of the unit cell is 120nm.

4.5 Conclusion

In a conclusion, we have proposed a new mechanism to directly excite dark modes (including the fundamental and higher-order modes) by using an electrical shorting approach with a continuous metal cover on a periodic HSQ pillar template. In absent of the metal sidewall, the top disks and back reflector provide a background resonance, and when the ultra-thin sidewall (thinner than skin depth to allow light power flow to pass through) is introduced, the background resonance and the strong coupling of the narrow gaps leads to the electrical standing wave resonance on the sidewall and therefore generates the dark plasmon modes. Such an approach is quite different from the conventional (indirect) methods of introducing dark modes (which are usually only of fundamental order). Owing to the high efficiency of direct excitation, our mechanism and nanostructure can additionally be naturally employed to achieve narrow-band perfect absorption under visible light. Such a narrow-band perfect absorption could be with great potential in color vibrancy applications, subject to the improvement in fabrication technologies which can be able to accurately control the size parameters of the nanostructure. The top metal disks behave like an electric current generator, and the quadrupoles and high-order multipoles in the dark modes can be excited on the sidewall electrically. At the resonance wavelength, the reflectance can be almost zero and the bandwidth is around 70 nm. Furthermore, by manipulating the structure size, we can also enhance the hexapolar mode to make it a dual-band absorber. In addition, we have discussed the size parameter tolerance to ensure the feasibility of fabrication. Apart from the obvious application as an absorber, our proposed method of exciting the dark mode in an electrically continuous structure may find applications in many other optical devices.

Chapter 5 Giant Photoluminescence Enhancement via Plasmonic Hybrid Nanostructures

5.1 Introduction: surface plasmon enhanced PL

In last chapters, we have investigated the resonance of nanostrucutures and therefore used them to manipulate light, so that we can generate colors and control the polarizations. And we also studied the fundamentals of dark plasmon resonances and found a new way to excite dark modes. Moreover, in order to better engineer the resonance of the nanostructures, we have to achieve deeper insight into the local effects of resonances, especially for plasmonic nanostructures. Based on the strong electric field enhancement and the cavity effects, plasmonic nanostructures have attracted a lot of research interests in near field applications, including photoluminescence (PL) [70, 78-80], sensing [81-84], optical tweezers and trapping [85-87] and other biological applications. In this chapter we will talk about the PL enhancement by plasmonic nanostructures. PL is emission of light which is caused by the irradiation of a material with other light . It is one of many forms of luminescence and is initiated by photo-excitation. Usually, PL is used in the context of semiconductor. Therefore, PL is excited by illumination of the semiconductor device with light which has a photon energy above the bandgap energy, and then occurs for wavelengths around the bandgap wavelength. Generally, PL has processes of absoption, energy transition and emission. The PL of the emitter is modified by its optical environment, which can be tuned by plasmonic nanostructures. When the decay dynamics of the emitter is perturbed by the modified density-of-states associated with the plasmonic nanostructure, the optical properties of the emitter can be manipulated [194], resulting in PL enhancement by the enhanced local electromagnetic field caused by surface-plasmon resonance [195-197]. In previous researches, the PL of Au nanostructure itself had been reported [198], and the SP-enhanced fluorescence of single molecular [194] and the SP- enhanced PL of semiconductors [195, 199-202] by plasmonic nanostructures had been deeply investigated. The enhancement can be explained in two ways: 1) enhanced absorption of incident light and 2) enhanced spontaneous emission rate. This enhancement can improve the performance of optical applications such as ultrathin light emitting diodes, photo-detectors, transistors, and biosensors.

Recently, strong PL emission enhancement by SPRs of metallic nanostructures has been reported in metal-semiconductor and 2D materials [78, 79, 194-197, 203-211]. In the following sections, we will focus on the influence of SPs to monolayer 2D materials and find methods to enhance the PL of 2D materials. We will introduce a cooperative work on giant PL enhancement in WSe_2-Au plasmonic hybrid nanostructures which achieved much higher PL enhancement than previous reported results. We will focus on the explanation and simulation of this phenomenon in terms of the local field caused enhancement of absorption and spontaneous emission rate by the Au nanostructures.

5.2 Photoluminescence of 2D materials

Since numerous research breakthrough has been achieved by investigating graphene [212], other kinds of 2D materials have also attracted considerable attention. One of the important research hot spots is the applications in ultrafast and ultrasensitive photodetectors, efficient light absorbers and emitters with 2D materials, which would be related to the PL of these 2D materials. Crystalline monolayers of transition metal dichalcogenides (TMDCs), such as molybdenum disulfide (MoS_2), molybdenum diselenide ($MoSe_2$), and tungsten diselenide (WSe_2), have PL emission which is caused by the transition from an indirect band gap semiconductor of these bulk materials to a direct band gap semiconductor in their atomically thin forms. Recently, PL of monolayer MoS_2, $MoSe_2$ and WSe_2 [213-218] has been reported. However, their application in photonic devices is limited by their low absolute PL caused by low quantum efficiency and weak absorption. One approach to boost light emission efficiency in TMDCs is utilizing the SPRs of metal nanostructures. Recently, the main designing strategy for metal nanostructure is increasing the emission rate of TMDCs by tuning the energy of SPRs to the exciton transition of TMDCs, and the effect of SPRs coupling to the excitation field of pump laser is often neglected. Based on this strategy, previous research works have demonstrated PL enhancement on monolayer MoS_2 using Au and Ag nanostructures [79, 206, 207, 209-211, 219-223]. However, due to its intrinsic low PL quantum yield efficiency, PL enhancement in monolayer MoS_2 is still modest even using complicated metal [79], limiting its application in optoelectronic devices. In comparison, WSe_2 is another promising TMDC material with a larger quantum efficiency than MoS_2 offering an alternative solution for designing efficient light absorbers or emitters [224-

229]. However, the PL response in WSe_2--plasmonic metal system has not been so deeply investigated as that of MoS_2--metal and the PL enhancement factor could be further improved so far.

5.3 PL enhancement of WSe_2 by square trenched Au nanostructure

In this section, we will report a cooperative work on huge PL enhancement in WSe_2-Au plasmonic hybrid structures. We hypothesized that plasmonic structure without resonance to TMDCs but with strong resonance to pump laser can also play a significant role in light absorption and emission of TMDCs. To verify our hypothesis and further improve the PL emission ability of TMDCs, a series of WSe_2−Au square or disk arrays was prepared, and 532nm and 633nm laser were used respectively to excite the PL of WSe_2 in order to explore the importance of template resonance at pumping laser wavelength. It is shown that the LSPR of the template strongly couples to 633 nm pump laser, leading to a giant PL enhancement factor up to three orders of magnitude in single crystal monolayer WSe_2. We have investigated the detailed mechanism for PL enhancement, and explained this phenomenon by both SPR enhanced pump laser absorption and enhanced spontaneous emission rate by Au nanostructures.

For the structure, a monolayer crystal WSe_2 flake was paved on the Au film with ultra-narrow square trenches, as shown in Fig 5-1. The width of the trench is sub-20nm, and the narrowest gap size can be ~12 ± 1 nm; the depth of trench is around 70nm; and the pitch size is much smaller than the pump and PL wavelength, ranging from 60nm to 200nm. Typical square shape is observed in Au templates with pitch size of 140nm to

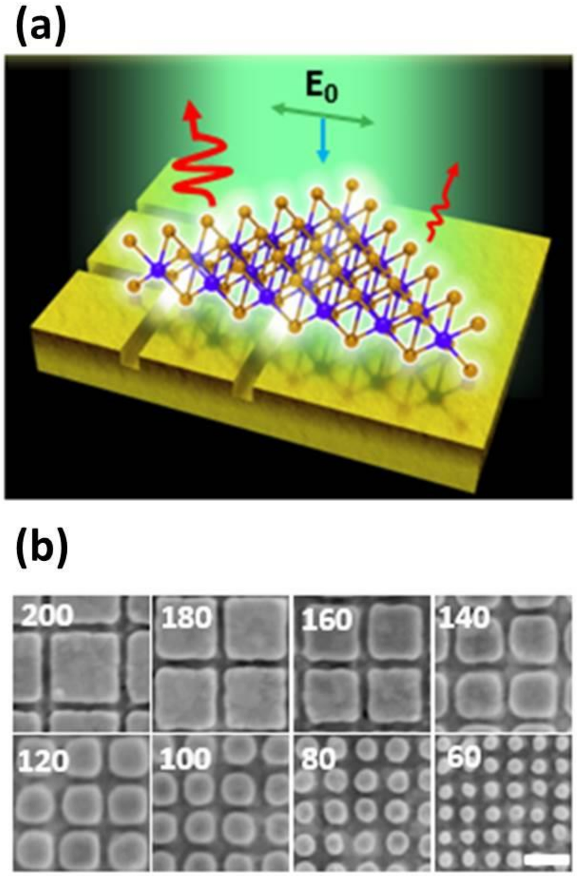

Fig 5-1 (a) Schematic of PL emission from a single crystal monolayer of WSe_2 flake on a gold substrate. Part of the triangular flake rests on the patterned region of the substrate consisting of sub-20-nm wide trenches. (b) SEM images of the template-stripped gold nanostructures of the patterned arrays with respective pitch sizes. The inset number denotes the pitch size in the unit of nm. The SEM images are having the same scale bar and the scale in the figures is 100 nm.

200nm. Nevertheless, when the pitch size is getting smaller, the Au structure transforms from square to disk, which is a typical shape of Au templates with pitch sizes of 60nm and 80nm. This is because extremely high spatial resolution for accurate definition of sub-20nm nanogaps is increasingly difficult to obtain when the pitch size is becoming small. Such a small size of the gaps between the Au squares is critical in plasmon coupling with light and optical field confinement, thus strong gap plasmon can be excited and the local electric field is significantly enhanced. These Au trench nanostructures provide strong local electric field at pumping wavelength so that the absoption of monolayer WSe_2 is largely enhanced, while they can also improve the emission rates at the PL wavelength.

Compared to the PL of pristine WSe_2 grown on sapphire substrate, the PL intensity of WSe_2 transferred onto unpatterned flat Au film is enhanced 7-fold and its peak position is slightly blue-shifted by 2 nm. The rise of PL intensity and the slight blue shift of the peak position observed in WSe_2 on gold flat film may be due to the charge transfer between gold and WSe_2 [230]. In order to have a systematic investigation on PL enhancement, a series of templates with different pitch sizes were prepared, as shown in Fig 5-1 (b). Fig 5-2 presents the PL spectra of WSe_2 on the various templates including unpatterned flat Au film using 633nm and 532nm pump lasers, respectively. Typical PL spectra of WSe_2 on the unpatterned flat Au film have one pronounced emission peak at 760nm, while the PL peak of monolayer WSe_2 on all templates is dramatically blue shifted to 745–754 nm. As pitch size increases, the resonance wavelength increases, and the PL peak position of the WSe_2 on Au templates almost continuously shifts towards longer wavelength, indicating the variation of PL peak position is influenced not only by charge transfer between gold and WSe_2, but also by the plasmon resonance of the Au template. In terms of PL intensity, we can see a much larger PL enhancement of WSe_2 on the Au templates than that on the unpatterned flat Au film. Here we define the average PL enhancement factor as PL intensity spectrally integrated from 700nm to 800nm of WSe_2 on the Au templates divided by that of WSe_2 on the unpatterned flat Au film. Moreover, it is worth noticing that the PL emission from bare gold templates are ranging from 532 to 700 nm, where it almost does not have any overlap with the PL from WSe_2, ranging from 700 to 800 nm. As a result, PL signal, collected from 700 nm to 800 nm, can be considered purely from WSe_2, rather than from the sum of WSe_2 and plasmonic nanostructures. When using 633nm pump laser, the PL enhancement factor increases from 143-fold for pitch size of 60nm to 1810-fold for pitch size of 200nm. This 1810-fold PL enhancement of WSe_2 by plasmonic nanostructures is the largest PL enhancement factor reported in metal--TMDCs hybrid system so far. In comparison, PL enhancement factors measured by 532nm laser are much smaller, where it could be due to that 532nm pump laser will excite the inter-band transition of electrons in Au so as to result in a higher material loss [198].

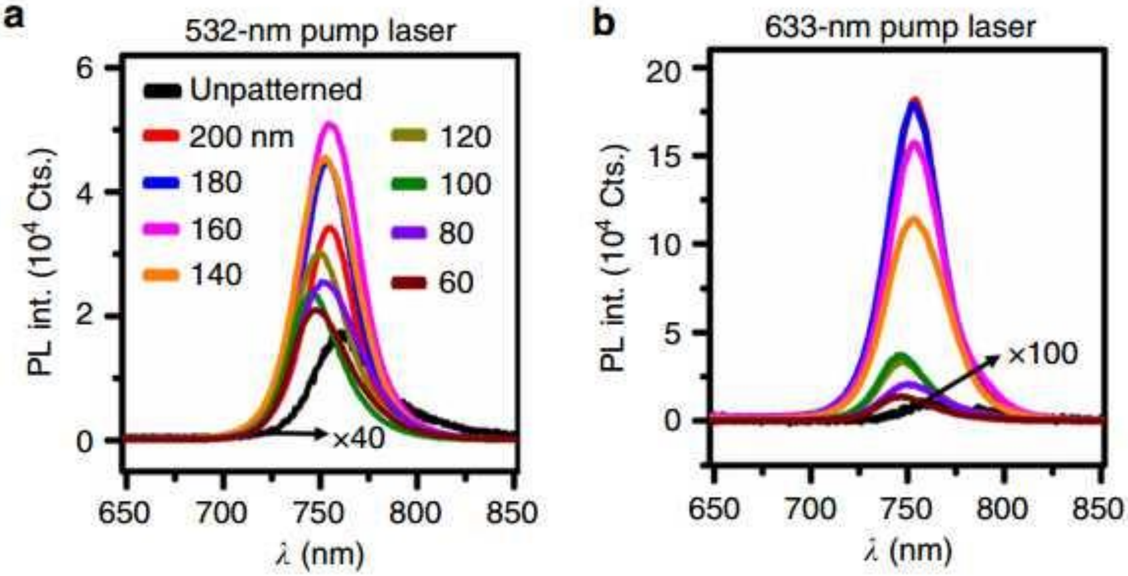

Fig 5-2 PL of WSe_2 on templates with different pitch size as measured by (a) 532nm pump laser and (b) 633nm pump laser, respectively. The different color curves represent PL with Au nanostructures with different pitch size from 60nm to 200nm, and the black curves represent PL of WSe_2 on unpatterned flat Au film (multiplied by 40 in (a) and multiplied by 100 in (b)).

5.3.1 Resonance wavelength and reflectance

The fabrication and measurement of the WSe_2-Au hybrid nanostructures is done by Dr. Dong Zhaogang and Wang Zhuo, and I have simulated the reflectance spectra of the nanostructures as well as the enhancement of absorption and emission (in the following sections). For fabrication, Dr. Dong Zhaogang and Wang Zhuo transferred chemical vapour deposition (CVD)-grown WSe2 monolayer flakes onto Au substrates onto which trenches as narrow as sub-20 nm have been patterned by a template-stripping method [231]. For the Au nanostructures, the square net trenches on the Au film are with sub-20nm width, around 70nm depth and 60nm to 200nm pitch sizes. The unit cells are much smaller than the half wavelength of pumping laser (532nm and 633nm) and the PL light (750nm), so we don't need to consider the grating effects. With such narrow and deep trenches, gaps plasmons are induced by the strong coupling of the Au cubes at both sides. The strong gap plasmon resonance greatly enlarges the absorption, leading to reflective dips.

To find out the resonance and better understand how the plasmonic resonance engineers the PL enhancement of WSe_2, we have simulated the relative reflection spectra to compare with experimental results, as shown in Fig 5-3. The reflectance is normalized with respect to the reflectance of a flat Au film. The geometries and dimensions of nanostructures with different pitch sizes are set to fit the SEM images of experiment samples in Fig 5-1(b). The edges are rounded and the widths are varied according to the SEM images. For small pitch sizes, the horizontal cutting planes look like circles while for larger pitch sizes they become better squares. As the pitch size increases, the resonance wavelength of Au nanostructures shifts from about 510nm to 630nm, which is closed to the wavelength of pump laser. Comparing the experimental and simulation spectra, the resonance wavelengths match quite well, and the experiment dip is a bit broader due to the size fluctuation in the fabrication.

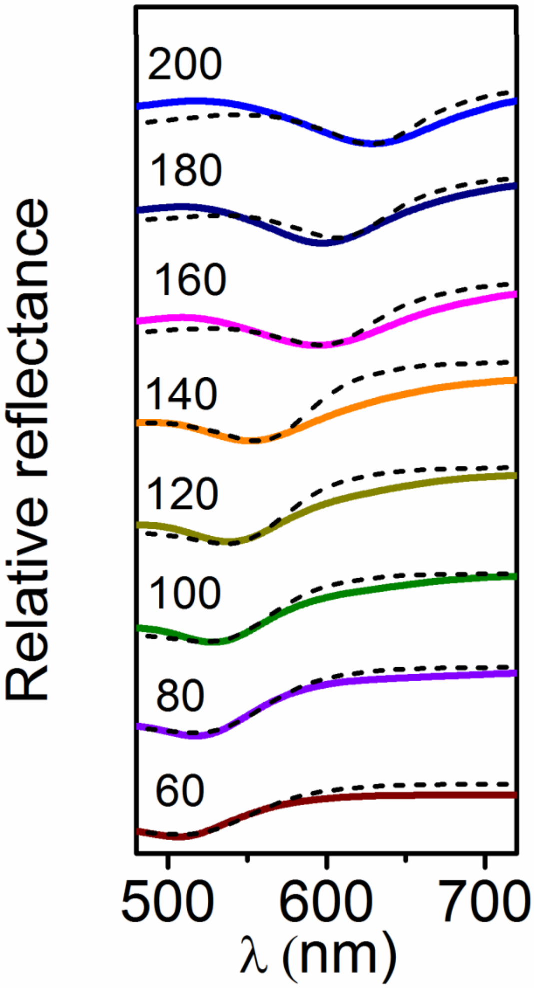

Fig 5-3 Relative reflectance spectra of patterned Au nanostructures with pitch size of 60nm to 200 nm with respect to the flat gold film. The solid and dashed curves present the experimental and simulated spectra, respectively. Legends denote the pitch size in units of nm for each pattern.

We propose that a local field enhancement due to the excitation of surface plasmon of the tempalte is responsible for the increase in WSe_2 PL intensity. This field enhancement increases the number of excited carriers in the WSe_2, leading to the enhanced PL [195]. Since localized surface plasmon exhibits largest near-field amplitude at the resonance wavelength, it may be argued that WSe_2 on template matching resonance with pump laser should have the largest PL enhancement factor. However, this is not the case in the experiment. Since we used pump lasers with wavelength of 532nm and 633nm, we can discuss relationship between the resonance wavelength of Au nanostructures with different pitch sizes and the pump laser wavelength. As shown in Fig 5-3, the resonance wavelength is closed to 633nm for template with 200nm pitch size, and the resonance wavelength is closed to 532nm for template with 100nm pitch size. Compared with the results in Fig 5-2, for 633nm pump laser, PL intensity is mostly enhanced for template with 200nm pitch size, however, for 532nm pump laser, PL intensity is mostly enhanced for template with 160nm pitch size, rather than 100nm pitch size. One of the explaination is that the match of resonance wavelength and the pump laser cannot ensure the maximum local field enhancement. As the resonance width reflected by the dip width in reflectance spectra of the templates is broad and resonance strength in each template varies, even if the resonance wavelength of a template deviates from the wavelength of the pump laser, a large PL enhancement factor can still be observed. Therefore, for different templates, a strong resonance with a larger wavelength shift is still possible to provide a stronger local electric field than a weak resonance with wavelength matching. On another hand, the enhancement in emission process for different templates should also be considered. In order to have a systematic investigation on PL enhancement, in the following sections, we will discuss the absorption enhancement (local electric field enhancement), the emission enhancement, and compare the combination of these two factors with the experimental results.

5.3.2 Absorption enhancement

The PL process can be enhanced by plasmonic nanostructures in both the absorption process and the emission process. The PL enhancement factor (EF) of monolayer WSe_2 on patterned nanostructure, compared to that on the flat Au film, is defined as:

$$\mathrm{EF} = \text{Pump Laser Enhancement Factor} \times \text{Purcell Factor} \tag{5.1}$$

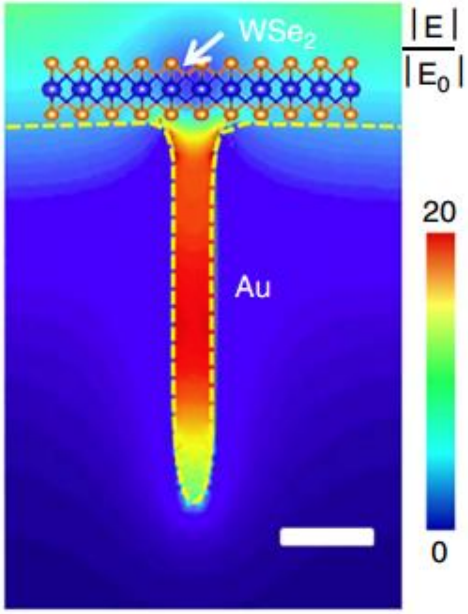

Fig 5-4 Representative simulation of the electric field distribution of the lateral gap plasmons with a WSe_2 monolayer flake suspended over a single trench. The polarization of the incident laser field is across the gap. The dashed yellow line denotes the boundary between air and gold. The scale bar: 20 nm.

where the pump laser enhancement factor is determined by the local electric field energy, and the Purcell factor indicates the emission enhancement.

In absorption process, the giant increment of PL intensity as observed in WSe_2-Au hybrid nanostructure is closely related with strong optical field induced by LSPR of the sub-20-nm gaps on gold templates. A representative simulation of the electric field distribution of the gap plasmons with a WSe_2 monolayer suspended over the trench is shown in Fig 5-4. Although the maximum electric field occurs inside the trench while the WSe_2 monolayer is located on top of the trench, the enhancement of local electric field on top of the trench is still considerable. FDTD method is used to simulate the electric field intensity enhancement factor, which is the average relative electric field intensity on top of the trench (just the sub-20nm gap region, where is the effectively enhanced region) with respect to that on flat Au film, at the wavelength of pump laser (532nm and 633nm) for each bare Au template, respectively. The periodic nanostructures are modeled as the

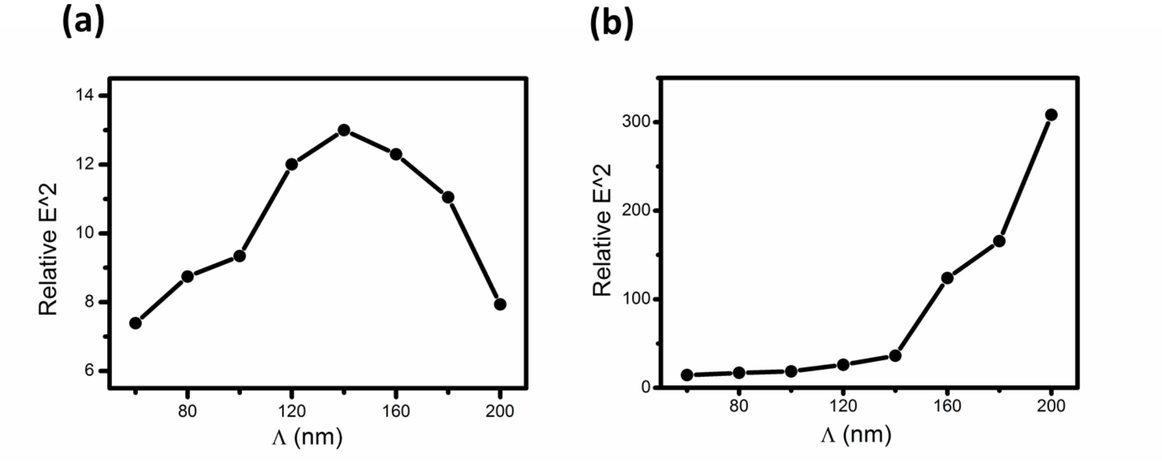

Fig 5-5 Relative electric energy enhancement on top of the trenches of Au nanostructures with different pitch sizes Λ at a pump laser of (a) 532nm and (b) 633nm.

image shown in Fig 5-1 (b), and since the WSe_2 monolayer is just one-atom thick, its contibution to the local electric field could be approximately neglected, so that we don't need the physical parameters for monolayer WSe_2. In Fig 5-5, the electric field intensity enhancement factors for different pitch sizes and pump lasers are shown. At a pump laser of 532nm, although the resonance wavelength of nanostructure with pitch size Λ = 100nm is closest to the pump wavelength, the maximum electric field enhancement occurs at Λ = 140nm. That is because the resonance intensity in this kind of nanostructures is generally stronger with larger resonance wavelength, and when resonance wavelength shifts too far away (with large Λ), the electric field at pump wavelength also decreases rapidly. At a pump laser of 633nm, the resonance wavelength of nanostructure with pitch size Λ = 200nm is closed to the pump wavelength, and the resonance intensity is also strong, so it obviously achieves the resonance intensity. Comparatively, the nanostructures can provide much stronger absorption enhancement with pump laser at 633nm rather than 532nm.

5.3.3 Emission enhancement

As claimed in eqn. (5.1), the PL enhancement is also related to the Purcell factor. The Purcell factor generally describes the enhancement of spontaneous emission rates of atoms when they are matched in a resonant cavity. In this work the Purcell factor is the enhancement of the spontaneous emission rates of WSe_2 on patterned Au nanostructures with respect to the spontaneous emission rates of WSe_2 on flat Au film. Together with the electric field enhancement at pump wavelength, the radiation enhancement at emission wavelength also contributes to the giant PL enhancement.

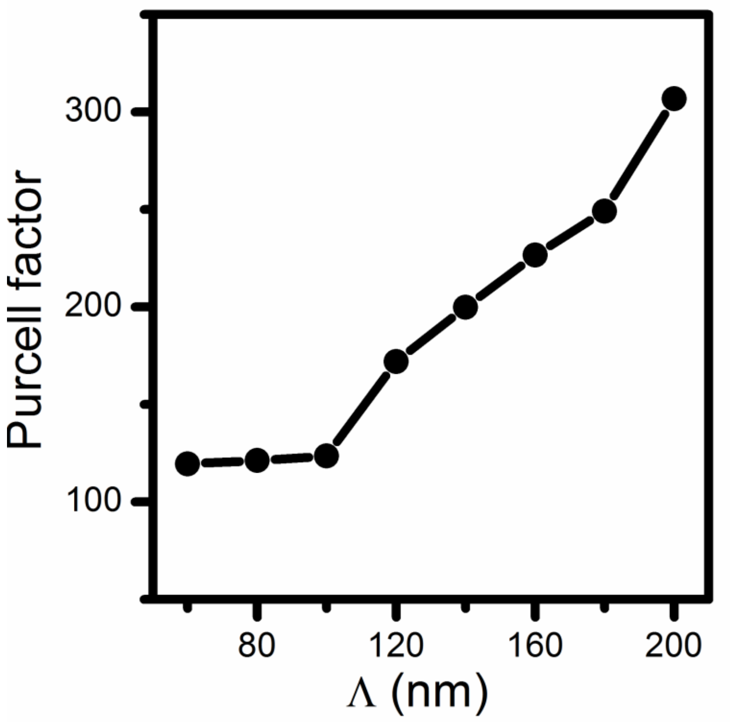

Fig 5-6 Purcell factor on top of the trenches of Au nanostructures with different pitch sizes Λ at emission wavelength of 750nm.

As shown in Fig 5-6, the Purcell factor increases as the pitch size of nanostructures increases, due to the reduction of interval between resonance wavelength and emission wavelength. Such a large Purcell factor of the ultra-narrow gap cavity has significantly improved the PL performance of monolayer WSe_2. In simulation, we have modeled the monolayer WSe_2 as a seris of arrayed dipole sources on top of the trenches to calculate the enhanced radiative power at 750nm, which is the PL wavelength of WSe_2 on Au templates. In FDTD, the radiative power of the dipole source can be obtained in the source monitors, and we calculate the total radiative power of the dipole sources on top of the trenches (sub-20nm wide region, the same as the calculation of enhanced electric fields) with respect to those radiative power of the same dipole sources on flat Au film, regarding as the Purcell factor. We should note that the Purcell factor is calculated neither at resonance wavelength nor at the strongest field positions (which are approximately at the center inside the trenches), so the Purcell factors should be much smaller than those Purcell factors (P_F) calculated from equation:

$$P_F = \frac{3}{4\pi^2}\left(\frac{\lambda_c}{n}\right)^3\left(\frac{Q}{V}\right) \tag{5.2}$$

where λ_c is the wavelength in vacuum, n is the refractive index, Q is the quality factor and V is the mode volume, respectively.

5.3.4 PL enhancement

Based on the absorption enhancement (by enhanced electric field energy) and the emission enhancement (by Purcell factor), we can calculate the simulated PL enhancement by eqn. (5.1), comparing with the experimental results measured by Wang Zhuo. As seen in Fig 5-7, the largest PL enhancement was achieved at the maximum of the product between the electric field enhancement factor at the excitation wavelength and the Purcell factor at the emission wavelength, at WSe_2 on the nanostructure with the pitch of 200 nm with 633nm pump laser, and at WSe_2 on the nanostructure with the pitch of 160 nm with 532nm pump laser. Therefore, the phenomenon that the maximum PL is not on the nanostructure with resonance matching 532nm pump laser in section 5.3.1 can be explained. Such a giant enhancement for the measured PL emission is due to the plasmon-enhanced absorption process and the plasmon-enhanced emission process together. With the gap plasmon resonance tuned to the 633nm pump laser wavelength,

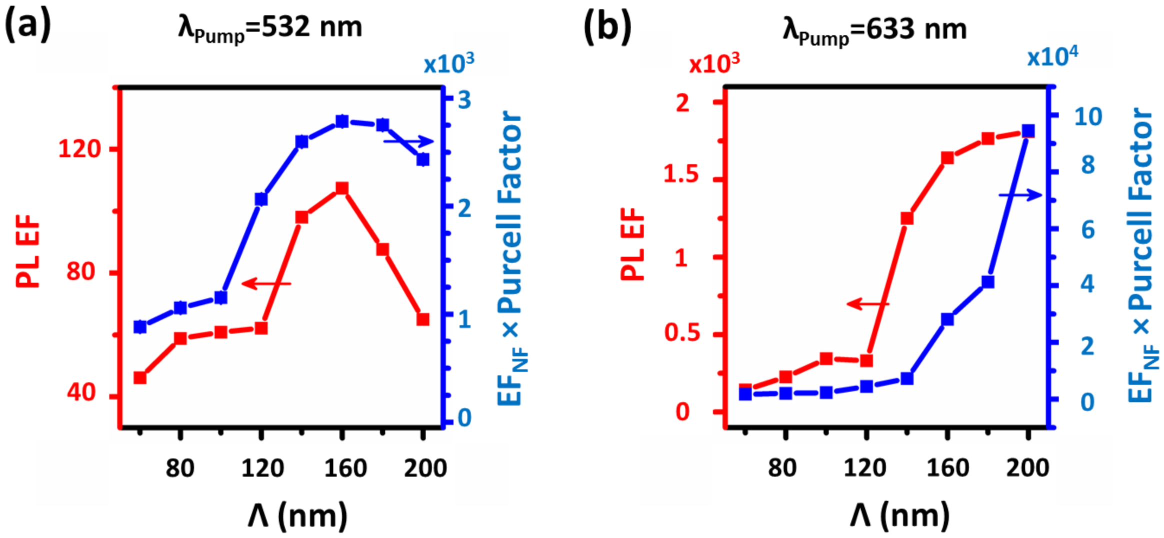

Fig 5-7 Simulated and experimental PL enhancement for different pitch sizes Λ with pump laser wavelength of (a) 532nm and (b) 633nm.

the integrated PL intensity from WSe_2 on Au nanostructure with 200nm pitch size was enhanced up to 1,810-fold (without correction by the trench area fraction) compared with the reference on unpatterned flat Au film. With measured PL mapping for large pitch sizes (larger than wavelength), we found that the enhancements are localized to WSe_2 at the trenches, and we assume it is also applicable to nanostructure with pitch size down to 200nm, which cannot be resolved in PL mapping. According to the polarization dependence, as measurements were done with the pump laser polarized along the x-axis, fields are confined only within the trenches along the y-axis. Correcting for the small area occupied by these trenches, we obtain the maximum effective PL enhancement factor of around 20,000 in WSe_2 over the trench using formula [219]:

$$\langle PL \rangle_{eff} = \frac{I_{patterned}}{I_{unpatterned}} \frac{A_0}{A_{gap}} \tag{5.3}$$

where $I_{patterned}$ is the PL intensity from WSe_2 on the patterned Au nanostructure and $I_{unpatterned}$ is the PL intensity from WSe_2 on flat Au film, A_0 represents the excitation area of the laser spot size, and A_{gap} represents the area of the trenches perpendicular to the polarization direction of the laser within the laser spot. Such a large effective PL enhancement factor hasn’t been reported in other works yet. Moreover, the curve shapes of simulation and experiment results agree with each other quite well for both 532nm and 633nm pump laser. For 633nm pumping, the abrupt increasing PL enhancement appears at smaller pitch samples in experiment, rather than that in simulation, due to the broader resonance caused by imperfection in fabrication. Overall, the simulation substantially explains the PL enhancement observed in experiment.

5.4 Summary

In conclusion, concentrating and manipulating the electromagnetic field in sub-20 nm trenches can achieve unprecedented PL enhancement of WSe2. Tuning the resonance of lateral gap plasmons to be aligned with the pump laser wavelength effectively boosts the light–matter interactions in WSe_2, and also enhances the light emission efficiency of WSe_2. A giant PL enhancement factor of about 20,000 was observed in WSe_2 on template with pitch size of 200nm when using the 633-nm pump laser. We have built up a simulation model to explain the giant PL enhancement observed experimentally in WSe_2-Au plasmonic hybrid nanostructures. The well-designed gap plasmon resonance can generate large enhancement for both absorption process (electric field enhanced absorption) and emission process (Purcell effect). The plasmonic nanostructures can manipulate the light absorption and emission of 2D materials like WSe_2, by the near-field interaction with incident pumping light and emitted light at PL wavelength. This work demonstrates an important method to enhance the PL of TMDCs since it could enable high-efficiency and high-quality photo-detectors and sensors, where photon absorption and emission dictate the device performance. The incorporation of Au nanostructures with sub-20nm trenches onto monolayer WSe_2 opens up a new platform for investigating novel electrical/optical properties in 2D materials, such as electroluminescence and second harmonic generation, speeding up the applications of novel optoelectronic devices.

Chapter 6 Conclusions

6.1 Summary of the thesis

This thesis has presents our works on manipulating light with subwavelength nanostructures. The interaction between light and subwavelength nanostructures is investigated, and several ways to engineer the resonances of nanostructures are reported. Our works presents optical applications realized by accurately controlled resonance and well-designed nanostructures and meta-surfaces.

The works can be generalized into two main parts. In the first part our works are manipulating far-field characteristics of light by meta-surfaces, including the spectra (intensity manipulation), phase and polarization of light. For the spectra manipulation, we have worked on the color nano-printing and imaging, controlling the spectra in visible light range. A comprehensive literature review was presented on the recent developments of ultra-high spatial resolution plasmonic colors. And then we reported our ultra-high spatial resolution non-plasmonic color printing with the color pixel made of ultra-narrow Si fin nanostructures in Chapter 2. Different from previous research works on Si colors, we didn’t use grating or waveguide mode scattering to manipulate light and generate colors. Our Si fin layer can be equivalent to an effective medium with a homogeneous refractive index, generating color by the Fabry-Perot resonance. And we also proposed an accurate quick and efficient TMM calculation to design the nanostructures for specific colors.

Another work to control far-field polarization of lights is the hybrid plasmonic QWPs. In Chapter 3 we present a design of actively reconfigurable plasmonic QWP working at multi-wavelength in visible and near-infrared light, which is hybrid meta-surface with a spacing layer of phase change material GST. The refractive index of GST layer between Au nano-cross and substrate can be controlled by switching the phase. The nanostructure works as a reflective QWP at 732nm with amorphous GST and at 781nm with crystalline GST. The polarization converting ratio is over 90% with corresponding phase state and very low with the other phase state at working wavelength. In addition, we have also reported two cooperative works on QWPs in THz range. Based on similar mechanism, the THz ultra-thin QWP can also enable active control of the optical functionalities. This switchable phase-change meta-surface provides a promising way for realization of polarization manipulating components, enabling novel applications with integrated optical devices.

The second main part is the fundamental resonance mechanism and local electromagnetic field related application research of subwavelength nanostructures. We have investigated in two aspects, one is the direct excited dark modes with normal incidence, and the other is the PL enhancement by WSe_2-Au hybrid nanostructures. In Chapter 4, we have proposed a new mechanism to directly excite dark modes by using an electrical shorting approach with a continuous metal cover on a periodic HSQ pillar template. The nanostructures can also achieve narrow-band perfect absorption under visible light, which is also with potential to manipulate far-field spectra, but the noble of the research is the mechanism to electrically induce dark plasmonic resonances on continuous metal structure without any asymmetry in geometry, environment and incidence. The local fields, electric charges, currents and Poynting vectors were also simulated and analyzed to improve the understanding of these special dark modes.

In Chapter 5, we presented a cooperative work on giant PL enhancement of WSe_2-Au plasmonic hybrid nanostructures. In simulation, we have explained how a squared trenched Au nanostructure with gap plasmon enhances the PL of monolayer WSe_2 on top of it. The enhancement was generated in both absorption process by strong local electric field and emission process with large Purcell effect. This work revealed that plasmonic nanostructures have paved an effective way to obtain giant PL in TMDC 2D materials with their characteristic resonances and enhanced local fields.

In this thesis, the optical constants of Si and all the metals are adopted from *Palik*, *Handbook of Optical Constants of Solids* [232]. And all the FDTD simulation is using commercial software *FDTD Solutions* from *Lumerical*.

6.2 Future research works

The future prospect of manipulation of light by subwavelength nanostructures is bright and promising. One of the valuable research aspects is to investigate multiple controlling of light by well-designed meta-surfaces, such as the five-dimensional hologram [59]. To enrich the information carried by the light, we could consider studying how to control the intensity, phase, polarization, spatial properties and multi-wavelength channels by meta-surface. In this field, the nanostructures need to be optimized to achieve high efficiency, high spatial resolution, excellent compatibility, low-cost fabrication, high wavelength and polarization sensitivity.

Another interesting work that can be done in the future is to design active and multi-functional optical devices with nanostructures. We can utilize the polarization and incident angle dependence, environment sensitivity of nanostructures, or we can employ the PCMs and semiconductors to enable active tuning of the characteristic of nanostructures, like the MMQWP we have designed in Chapter 3. Besides the MMQWP, we can still try to discover valuable optical applications with judiciously designed tunable nanostructures.

It is also interesting and important to combine plasmonic nanostructures with other materials and matters like 2D materials (graphene, monolayer TMDCs), bio-molecules, semiconductors, high index materials with magnetic modes, etc. The strong local field of SPR modes of plasmonic nanostructures could provide a way to enhance the optical performance or strengthen the characterization of their optical properties.

Bibliography

1. Pendry, J.B., *Negative refraction makes a perfect lens.* Physical Review Letters, 2000. **85**(18): p. 3966.
2. Shelby, R.A., D.R. Smith, and S. Schultz, *Experimental verification of a negative index of refraction.* Science, 2001. **292**(5514): p. 77.
3. Smith, D.R., et al., *Composite medium with simultaneously negative permeability and permittivity.* Physical Review Letters, 2000. **84**(18): p. 4184.
4. Xiao, S.M., et al., *Loss-free and active optical negative-index metamaterials.* Nature, 2010. **466**(7307): p. 735.
5. Ellenbogen, T., K. Seo, and K.B. Crozier, *Chromatic plasmonic polarizers for active visible color filtering and polarimetry.* Nano Lett, 2012. **12**(2): p. 1026.
6. Goh, X.M., et al., *Three-dimensional plasmonic stereoscopic prints in full colour.* Nature Communications, 2014. **5**: p. 5361.
7. Gu, Y.H., et al., *Color generation via subwavelength plasmonic nanostructures.* Nanoscale, 2015. **7**(15): p. 6409.
8. Kumar, K., et al., *Printing colour at the optical diffraction limit.* Nat Nanotechnol, 2012. **7**(9): p. 557.
9. Liu, Y.J., et al., *Optically tunable plasmonic color filters.* Applied Physics A, 2011. **107**(1): p. 49.
10. Roberts, A.S., et al., *Subwavelength plasmonic color printing protected for ambient use.* Nano Lett, 2014. **14**(2): p. 783.
11. Si, G., et al., *Annular aperture array based color filter.* Applied Physics Letters, 2011. **99**(3): p. 033105.
12. Si, G., et al., *Reflective plasmonic color filters based on lithographically patterned silver nanorod arrays.* Nanoscale, 2013. **5**(14): p. 6243.
13. Tan, S.J., et al., *Engineering Plasmonic Colors in Metal Nanostructures.* Journal of Molecular and Engineering Materials, 2014. **02**(02): p. 1440011.
14. Tan, S.J., et al., *Plasmonic color palettes for photorealistic printing with aluminum nanostructures.* Nano Lett, 2014. **14**(7): p. 4023.
15. Wu, Y.K., et al., *Angle-insensitive structural colours based on metallic nanocavities and coloured pixels beyond the diffraction limit.* Sci Rep, 2013. **3**: p. 1194.
16. Xu, T., et al., *Structural colors: from plasmonic to carbon nanostructures.* Small, 2011. **7**(22): p. 3128.
17. Xu, T., et al., *Plasmonic nanoresonators for high-resolution colour filtering and spectral imaging.* Nat Commun, 2010. **1**: p. 59.
18. Yoon, Y.-T., C.-H. Park, and S.-S. Lee, *Highly Efficient Color Filter Incorporating a Thin Metal–Dielectric Resonant Structure.* Applied Physics Express, 2012. **5**(2): p. 022501.
19. Yu, Y., et al., *Transmissive/Reflective Structural Color Filters: Theory and Applications.* Journal of Nanomaterials, 2014. **2014**: p. 1.
20. Zeng, B., Y. Gao, and F.J. Bartoli, *Ultrathin nanostructured metals for highly transmissive plasmonic subtractive color filters.* Sci Rep, 2013. **3**: p. 2840.
21. Fang, N., et al., *Sub-diffraction-limited optical imaging with a silver superlens.* Science, 2005. **308**(5721): p. 534.
22. Chen, Z.C., et al., *Terahertz achromatic quarter wave plate: Design, fabrication, and characterization.* Optics Communications, 2014. **311**: p. 1.

23. Cong, L.Q., et al., *Highly flexible broadband terahertz metamaterial quarter-wave plate.* Laser & Photonics Reviews, 2014. **8**(4): p. 626.
24. Masson, J.B. and G. Gallot, *Terahertz achromatic quarter-wave plate.* Optics Letters, 2006. **31**(2): p. 265.
25. Strikwerda, A.C., et al., *Comparison of birefringent electric split-ring resonator and meanderline structures as quarter-wave plates at terahertz frequencies.* Optics Express, 2009. **17**(1): p. 136.
26. Wang, D., et al., *An ultrathin terahertz quarter-wave plate using planar babinet-inverted metasurface.* Opt Express, 2015. **23**(9): p. 11114.
27. Wang, D., et al., *Switchable Ultrathin Quarter-wave Plate in Terahertz Using Active Phase-change Metasurface.* Sci Rep, 2015. **5**: p. 15020.
28. Yu, N., et al., *A broadband, background-free quarter-wave plate based on plasmonic metasurfaces.* Nano Lett, 2012. **12**(12): p. 6328.
29. Huang, L.L., et al., *Three-dimensional optical holography using a plasmonic metasurface.* Nat Commun, 2013. **4**: p. 2808.
30. Qiu, C.W., et al., *Spherical cloaking with homogeneous isotropic multilayered structures.* Physical Review E, 2009. **79**(4): p. 047602.
31. Schurig, D., et al., *Metamaterial electromagnetic cloak at microwave frequencies.* Science, 2006. **314**(5801): p. 977.
32. Cao, T., et al., *Rapid phase transition of a phase-change metamaterial perfect absorber.* Optical Materials Express, 2013. **3**(8): p. 1101.
33. Cao, T., et al., *Broadband polarization-independent perfect absorber using a phase-change metamaterial at visible frequencies.* Sci Rep, 2014. **4**: p. 3955.
34. Cao, T., et al., *Mid-infrared tunable polarization-independent perfect absorber using a phase-change metamaterial.* Journal of the Optical Society of America B, 2013. **30**(6): p. 1580.
35. Li, H., et al., *Ultrathin multiband gigahertz metamaterial absorbers.* Journal of Applied Physics, 2011. **110**(1): p. 014909.
36. Pu, M.B., et al., *Ultrathin broadband nearly perfect absorber with symmetrical coherent illumination.* Optics Express, 2012. **20**(3): p. 2246.
37. Shen, X.P. and T.J. Cui, *Photoexcited broadband redshift switch and strength modulation of terahertz metamaterial absorber.* Journal of Optics, 2012. **14**(11): p. 114012.
38. Cao, T., et al., *Strongly tunable circular dichroism in gammadion chiral phase-change metamaterials.* Optics Express, 2013. **21**(23): p. 27841.
39. Kenanakis, G., et al., *Optically controllable THz chiral metamaterials.* Optics Express, 2014. **22**(10): p. 12149.
40. Pu, M.B., et al., *Anisotropic meta-mirror for achromatic electromagnetic polarization manipulation.* Applied Physics Letters, 2013. **102**(13): p. 131906.
41. Singh, R., et al., *Terahertz metamaterial with asymmetric transmission.* Physical Review B, 2009. **80**(15): p. 153104.
42. Singh, R., et al., *Highly tunable optical activity in planar achiral terahertz metamaterials.* Optics Express, 2010. **18**(13): p. 13425.
43. Zalkovskij, M., et al., *Optically active Babinet planar metamaterial film for terahertz polarization manipulation.* Laser & Photonics Reviews, 2013. **7**(5): p. 810.
44. Zhang, S., et al., *Photoinduced handedness switching in terahertz chiral metamolecules.* Nat Commun, 2012. **3**: p. 942.
45. Ma, X.L., et al., *Dual-band asymmetry chiral metamaterial based on planar spiral structure.* Applied Physics Letters, 2012. **101**(16): p. 161901.

46. Kildishev, A.V., A. Boltasseva, and V.M. Shalaev, *Planar Photonics with Metasurfaces.* Science, 2013. **339**(6125): p. 1232009.
47. Lin, D.M., et al., *Dielectric gradient metasurface optical elements.* Science, 2014. **345**(6194): p. 298.
48. Liu, L., et al., *Broadband metasurfaces with simultaneous control of phase and amplitude.* Adv Mater, 2014. **26**(29): p. 5031.
49. Luo, X.G., *Principles of electromagnetic waves in metasurfaces.* Science China-Physics Mechanics & Astronomy, 2015. **58**(9): p. 594201.
50. Meinzer, N., W.L. Barnes, and I.R. Hooper, *Plasmonic meta-atoms and metasurfaces.* Nature Photonics, 2014. **8**(12): p. 889.
51. Pu, M.B., et al., *Broadband anomalous reflection based on gradient low-Q meta-surface.* Aip Advances, 2013. **3**(5): p. 052136.
52. Yu, N.F. and F. Capasso, *Flat optics with designer metasurfaces.* Nature Materials, 2014. **13**(2): p. 139.
53. Yu, N.F., et al., *Light Propagation with Phase Discontinuities: Generalized Laws of Reflection and Refraction.* Science, 2011. **334**(6054): p. 333.
54. Zhang, X.Q., et al., *Broadband Terahertz Wave Deflection Based on C-shape Complex Metamaterials with Phase Discontinuities.* Advanced Materials, 2013. **25**(33): p. 4567.
55. Minovich, A., et al., *Generation and Near-Field Imaging of Airy Surface Plasmons.* Physical Review Letters, 2011. **107**(11): p. 545.
56. Pfeiffer, C. and A. Grbic, *Generating stable tractor beams with dielectric metasurfaces.* Physical Review B, 2015. **91**(11): p. 115408.
57. Huang, Y.W., et al., *Aluminum plasmonic multicolor meta-hologram.* Nano Lett, 2015. **15**(5): p. 3122.
58. Wintz, D., et al., *Holographic metalens for switchable focusing of surface plasmons.* Nano Lett, 2015. **15**(5): p. 3585.
59. Zijlstra, P., J.W. Chon, and M. Gu, *Five-dimensional optical recording mediated by surface plasmons in gold nanorods.* Nature, 2009. **459**(7245): p. 410.
60. Ni, X., A.V. Kildishev, and V.M. Shalaev, *Metasurface holograms for visible light.* Nature Communications, 2013. **4**(4): p. 657.
61. Zheng, G., et al., *Metasurface holograms reaching 80% efficiency.* Nat Nanotechnol, 2015. **10**(4): p. 308.
62. Gu, Y., et al., *Direct excitation of dark plasmonic resonances under visible light at normal incidence.* Nanoscale, 2014. **6**(4): p. 2106.
63. Sancho-Parramon, J., et al., *Plasmonic dark modes excited by strongly focused illumination*, in *Proc. SPIE*. 2015. p. 954731.
64. Dobmann, S., et al., *Near-Field Analysis of Bright and Dark Modes on Plasmonic Metasurfaces Showing Extraordinary Suppressed Transmission.* Advanced Optical Materials, 2014. **2**(10): p. 990.
65. Gómez, D.E., et al., *The Dark Side of Plasmonics.* Nano Letters, 2013. **13**(8): p. 3722.
66. Maier, S.A., *Plasmonics: The benefits of darkness.* Nat Mater, 2009. **8**(9): p. 699.
67. Fano, U., *Effects of Configuration Interaction on Intensities and Phase Shifts.* Physical Review, 1961. **124**(6): p. 1866.
68. Luk'yanchuk, B., et al., *The Fano resonance in plasmonic nanostructures and metamaterials.* Nat Mater, 2010. **9**(9): p. 707.
69. Jung, J., T. Søndergaard, and S.I. Bozhevolnyi, *Gap plasmon-polariton nanoresonators: Scattering enhancement and launching of surface plasmon polaritons.* Physical Review B, 2009. **79**(3): p. 035401.

70. Lumdee, C., B. Yun, and P.G. Kik, *Gap-Plasmon Enhanced Gold Nanoparticle Photoluminescence.* ACS Photonics, 2014. **1**(11): p. 1224.
71. Jakovljević, M.M., et al., *Polarization-dependent optical excitation of gap plasmon polaritons through rectangular hole arrays.* Applied Physics Letters, 2015. **106**(14): p. 143106.
72. Pors, A., et al., *Gap plasmon-based metasurfaces for total control of reflected light.* Scientific Reports, 2013. **3**: p. 2155.
73. Staude, I., et al., *Shaping Photoluminescence Spectra with Magnetoelectric Resonances in All-Dielectric Nanoparticles.* ACS Photonics, 2015. **2**(2): p. 172.
74. Yan, J.H., et al., *Magnetically induced forward scattering at visible wavelengths in silicon nanosphere oligomers.* Nat Commun, 2015. **6**: p. 7042.
75. Staude, I., et al. *Merging Magnetic and Electric Resonances for All-Dielectric Nanoantenna Arrays*. in *CLEO: 2013*. 2013. San Jose, California: Optical Society of America. p. QF2A.2.
76. Decker, M., et al., *High-Efficiency Dielectric Huygens' Surfaces.* Advanced Optical Materials, 2015. **3**(6): p. 813.
77. Sautter, J., et al., *Active Tuning of All-Dielectric Metasurfaces.* ACS Nano, 2015. **9**(4): p. 4308.
78. Shahbazyan, T.V., *Theory of Plasmon-Enhanced Metal Photoluminescence.* Nano Letters, 2013. **13**(1): p. 194.
79. Lee, B., et al., *Fano Resonance and Spectrally Modified Photoluminescence Enhancement in Monolayer MoS2 Integrated with Plasmonic Nanoantenna Array.* Nano Letters, 2015. **15**(5): p. 3646.
80. Song, M., et al., *Photoluminescence Plasmonic Enhancement of Single Quantum Dots Coupled to Gold Microplates.* The Journal of Physical Chemistry C, 2014. **118**(16): p. 8514.
81. Anker, J.N., et al., *Biosensing with plasmonic nanosensors.* Nat Mater, 2008. **7**(6): p. 442.
82. Tittl, A., H. Giessen, and N. Liu, *Plasmonic gas and chemical sensing.* Nanophotonics, 2014. **3**(3): p. 157.
83. Wadell, C., S. Syrenova, and C. Langhammer, *Plasmonic Hydrogen Sensing with Nanostructured Metal Hydrides.* ACS Nano, 2014. **8**(12): p. 11925.
84. Stockman, M.I., *Nanoplasmonic sensing and detection.* Science, 2015. **348**(6232): p. 287.
85. Juan, M.L., M. Righini, and R. Quidant, *Plasmon nano-optical tweezers.* Nat Photon, 2011. **5**(6): p. 349.
86. Tsuboi, Y., *Plasmonic optical tweezers: A long arm and a tight grip.* Nat Nano, 2015. **11**(1): p. 5.
87. Shoji, T. and Y. Tsuboi, *Plasmonic Optical Tweezers toward Molecular Manipulation: Tailoring Plasmonic Nanostructure, Light Source, and Resonant Trapping.* The Journal of Physical Chemistry Letters, 2014. **5**(17): p. 2957.
88. Huo, Y., C.C. Fesenmaier, and P.B. Catrysse, *Microlens performance limits in sub-2mum pixel CMOS image sensors.* Opt Express, 2010. **18**(6): p. 5861.
89. Koo, H.-S., M. Chen, and P.-C. Pan, *LCD-based color filter films fabricated by a pigment-based colorant photo resist inks and printing technology.* Thin Solid Films, 2006. **515**(3): p. 896.
90. Abbe, E., *A Contribution to the Theory of the Microscope and the Nature of Microscopic Vision.* Proc. Bristol Nat. Soc, 1876. **1**: p. 200.
91. Ozbay, E., *Plasmonics: merging photonics and electronics at nanoscale dimensions.* Science, 2006. **311**(5758): p. 189.

92. Zayats, A.V., I.I. Smolyaninov, and A.A. Maradudin, *Nano-optics of surface plasmon polaritons.* Physics Reports, 2005. **408**(3-4): p. 131.
93. Laux, E., et al., *Plasmonic photon sorters for spectral and polarimetric imaging.* Nat Photon, 2008. **2**(3): p. 161.
94. Barnes, W.L., A. Dereux, and T.W. Ebbesen, *Surface plasmon subwavelength optics.* Nature, 2003. **424**(6950): p. 824.
95. H. Duan, H.H., K. Kumar, Z. Shen, J. K.W. Yang, *Direct and Reliable Patterning of Plasmonic Nanostructures with Sub-10-nm Gaps.* ACS Nano, 2011. **5**(9): p. 7593.
96. H. Duan, H.H., H. K. Hui, Z. Shen, J. K W Yang, *Free-standing sub-10 nm nanostencils for the definition of gaps in plasmonic antennas.* Nanotechnology, 2013. **24**(18): p. 185301.
97. Diest, K., et al., *Tunable Color Filters Based on Metal−Insulator−Metal Resonators.* Nano Letters, 2009. **9**(7): p. 2579.
98. Saeidi, C. and D. van der Weide, *Bandwidth-tunable optical spatial filters with nanoparticle arrays.* Opt Express, 2014. **22**(10): p. 12499.
99. Liu, Y.J., et al., *Light-driven plasmonic color filters by overlaying photoresponsive liquid crystals on gold annular aperture arrays.* Adv Mater, 2012. **24**(23): p. OP131.
100. Zijlstra, P., J.W.M. Chon, and M. Gu, *Five-dimensional optical recording mediated by surface plasmons in gold nanorods.* Nature, 2009. **459**(7245): p. 410.
101. Do, J., et al., *Two-color laser printing of individual gold nanorods.* Nano Lett, 2013. **13**(9): p. 4164.
102. Chen, W.T., et al., *High-Efficiency Broadband Meta-Hologram with Polarization-Controlled Dual Images.* Nano Letters, 2014. **14**(1): p. 225.
103. Shengli, Z. and C.S. George, *Theoretical studies of plasmon resonances in one-dimensional nanoparticle chains: narrow lineshapes with tunable widths.* Nanotechnology, 2006. **17**(11): p. 2813.
104. Auguié, B. and W.L. Barnes, *Collective Resonances in Gold Nanoparticle Arrays.* Physical Review Letters, 2008. **101**(14): p. 28.
105. García de Abajo, F.J., *Light scattering by particle and hole arrays.* Reviews of Modern Physics, 2007. **79**(4): p. 1267.
106. Kravets, V.G., F. Schedin, and A.N. Grigorenko, *Extremely Narrow Plasmon Resonances Based on Diffraction Coupling of Localized Plasmons in Arrays of Metallic Nanoparticles.* Physical Review Letters, 2008. **101**(8): p. 087403.
107. Sarrazin, M., J.-P. Vigneron, and J.-M. Vigoureux, *Role of Wood anomalies in optical properties of thin metallic films with a bidimensional array of subwavelength holes.* Physical Review B, 2003. **67**(8): p. 085415.
108. J. Strasswimmer, M.C.P., B. H. Park, V. Neel, J. F. de Boer, *Polarization-sensitive optical coherence tomography of invasive basal cell carcinoma.* J. Biomed. Opt., 2004. **9**(2): p. 292.
109. Kaplan, A.F., T. Xu, and L. Jay Guo, *High efficiency resonance-based spectrum filters with tunable transmission bandwidth fabricated using nanoimprint lithography.* Applied Physics Letters, 2011. **99**(14): p. 143111.
110. Genet, C. and T.W. Ebbesen, *Light in tiny holes.* Nature, 2007. **445**(7123): p. 39.
111. Bethe, H.A., *Theory of Diffraction by Small Holes.* Physical Review, 1944. **66**(7-8): p. 163.
112. Altewischer, E., M.P. van Exter, and J.P. Woerdman, *Plasmon-assisted transmission of entangled photons.* Nature, 2002. **418**(6895): p. 304.
113. Stefan, E., et al., *Enhanced light transmission by hole arrays.* Journal of Optics A: Pure and Applied Optics, 2002. **4**(5): p. S83.

114. Fan, W., et al., *Enhanced Infrared Transmission through Subwavelength Coaxial Metallic Arrays.* Physical Review Letters, 2005. **94**(3): p. 033902.
115. Koerkamp, K.J.K., et al., *Strong Influence of Hole Shape on Extraordinary Transmission through Periodic Arrays of Subwavelength Holes.* Physical Review Letters, 2004. **92**(18): p. 183901.
116. Prikulis, J., et al., *Optical Spectroscopy of Nanometric Holes in Thin Gold Films.* Nano Letters, 2004. **4**(6): p. 1003.
117. Barnes, W.L., et al., *Surface Plasmon Polaritons and Their Role in the Enhanced Transmission of Light through Periodic Arrays of Subwavelength Holes in a Metal Film.* Physical Review Letters, 2004. **92**(10): p. 107401.
118. Altewischer, E., M.P. van Exter, and J.P. Woerdman, *Polarization analysis of propagating surface plasmons in a subwavelength hole array.* Journal of the Optical Society of America B, 2003. **20**(9): p. 1927.
119. Garcia-Meca, C., et al., *Negative refractive index metamaterials aided by extraordinary optical transmission.* Optics Express, 2009. **17**(8): p. 6026.
120. Walls, K., et al., *Automated Design, Fabrication, and Characterization of Color Matching Plasmonic Filters.* Photonics Technology Letters, IEEE, 2012. **24**(7): p. 602.
121. Popov, E., et al., *Theory of light transmission through subwavelength periodic hole arrays.* Physical Review B, 2000. **62**(23): p. 16100.
122. Strelniker, Y.M. and D.J. Bergman, *Optical transmission through metal films with a subwavelength hole array in the presence of a magnetic field.* Physical Review B, 1999. **59**(20): p. R12763.
123. Lomakin, V. and E. Michielssen, *Enhanced transmission through metallic plates perforated by arrays of subwavelength holes and sandwiched between dielectric slabs.* Physical Review B, 2005. **71**(23): p. 235117.
124. Egorov, D., et al., *Two-dimensional control of surface plasmons and directional beaming from arrays of subwavelength apertures.* Physical Review B, 2004. **70**(3): p. 033404.
125. Fan, W., et al., *Enhanced infrared transmission through subwavelength coaxial metallic arrays.* Physical Review Letters, 2005. **94**(3): p. 033902.
126. Inoue, D., et al., *Polarization independent visible color filter comprising an aluminum film with surface-plasmon enhanced transmission through a subwavelength array of holes.* Applied Physics Letters, 2011. **98**(9): p. 093113.
127. Chen, Q. and D.R.S. Cumming, *High transmission and low color cross-talk plasmonic color filters using triangular-lattice hole arrays in aluminum films.* Optics Express, 2010. **18**(13): p. 14056.
128. Grady, N.K., et al., *Terahertz Metamaterials for Linear Polarization Conversion and Anomalous Refraction.* Science, 2013. **340**(6138): p. 1304.
129. Genet, C., M.P. van Exter, and J.P. Woerdman, *Fano-type interpretation of red shifts and red tails in hole array transmission spectra.* Optics Communications, 2003. **225**(4–6): p. 331.
130. Li, W.-D., J. Hu, and S.Y. Chou, *Extraordinary light transmission through opaque thin metal film with subwavelength holes blocked by metal disks.* Optics Express, 2011. **19**(21): p. 21098.
131. Li, W.-D., et al., *Three-dimensional cavity nanoantenna coupled plasmonic nanodots for ultrahigh and uniform surface-enhanced Raman scattering over large area.* Optics Express, 2011. **19**(5): p. 3925.
132. Vukusic, P. and J.R. Sambles, *Photonic structures in biology.* Nature, 2003. **424**(6950): p. 852.

133. Sinivasarao, M., *Nano-Optics in the Biological World: Beetles, Butterflies, Birds, and Moths.* Chem. Rev., 1999. **99**(7): p. 1935.
134. Huang, J., X. Wang, and Z.L. Wang, *Controlled Replication of Butterfly Wings for Achieving Tunable Photonic Properties.* Nano Letters, 2006. **6**(10): p. 2325.
135. Kustandi, T.S., et al., *Mimicking domino-like photonic nanostructures on butterfly wings.* Small, 2009. **5**(5): p. 574.
136. Vukusic, P., J.R. Sambles, and C.R. Lawrence, *Structural colour: Colour mixing in wing scales of a butterfly.* Nature, 2000. **404**(6777): p. 457.
137. Kinoshita, S., S. Yoshioka, and K. Kawagoe, *Mechanisms of structural colour in the Morpho butterfly: cooperation of regularity and irregularity in an iridescent scale.* Proceedings of the Royal Society of London B: Biological Sciences, 2002. **269**(1499): p. 1417.
138. Lawrence, C., P. Vukusic, and R. Sambles, *Grazing-incidence iridescence from a butterfly wing.* Applied Optics, 2002. **41**(3): p. 437.
139. Ghiradella, H., *Light and color on the wing: structural colors in butterflies and moths.* Applied Optics, 1991. **30**(24): p. 3492.
140. Cao, L., et al., *Tuning the color of silicon nanostructures.* Nano Lett, 2010. **10**(7): p. 2649.
141. Khorasaninejad, M., et al., *Color Matrix Refractive Index Sensors Using Coupled Vertical Silicon Nanowire Arrays.* Nano Letters, 2012. **12**(8): p. 4228.
142. Seo, K., et al., *Multicolored Vertical Silicon Nanowires.* Nano Letters, 2011. **11**(4): p. 1851.
143. Park, H., et al., *Filter-free image sensor pixels comprising silicon nanowires with selective color absorption.* Nano Lett, 2014. **14**(4): p. 1804.
144. Shrestha, V.R., et al., *Non-iridescent Transmissive Structural Color Filter Featuring Highly Efficient Transmission and High Excitation Purity.* Scientific Reports, 2014. **4**: p. 4921.
145. Yang, Y., et al., *All-dielectric metasurface analogue of electromagnetically induced transparency.* Nat Commun, 2014. **5**: p. 5753.
146. Kuznetsov, A.I., et al., *Magnetic light.* Scientific Reports, 2012. **2**: p. 492.
147. West, P.R., et al., *All-dielectric subwavelength metasurface focusing lens.* Optics Express, 2014. **22**(21): p. 26212.
148. Khorasaninejad, M. and K.B. Crozier, *Silicon nanofin grating as a miniature chirality-distinguishing beam-splitter.* Nat Commun, 2014. **5**(5): p. 5386.
149. Wu, A., et al., *Experimental Demonstration of In-Plane Negative-Angle Refraction with an Array of Silicon Nanoposts.* Nano Letters, 2015. **15**(3): p. 2055.
150. Park, H., K. Seo, and K.B. Crozier, *Adding colors to polydimethylsiloxane by embedding vertical silicon nanowires.* Applied Physics Letters, 2012. **101**(19): p. 193107.
151. Cao, L., P. Fan, and M.L. Brongersma, *Optical Coupling of Deep-Subwavelength Semiconductor Nanowires.* Nano Letters, 2011. **11**(4): p. 1463.
152. Park, H. and K.B. Crozier, *Multispectral imaging with vertical silicon nanowires.* Scientific Reports, 2013. **3**: p. 2460.
153. Goncharenko, A.V., V.Z. Lozovski, and E.F. Venger, *Lichtenecker's equation: applicability and limitations.* Optics Communications, 2000. **174**(1-4): p. 19.
154. Born, M.W., E., *Principles of optics: electromagnetic theory of propagation, interference and diffraction of light.* Oxford, Pergamon Press, 1964.
155. Wiesauer, K. and C. Jordens, *Recent Advances in Birefringence Studies at THz Frequencies.* Journal of Infrared Millimeter and Terahertz Waves, 2013. **34**(11): p. 663.
156. Hao, J.M., et al., *Manipulating electromagnetic wave polarizations by anisotropic metamaterials.* Physical Review Letters, 2007. **99**(6): p. 063908.

157. Ma, X.L., et al., *An Active Metamaterial for Polarization Manipulating.* Advanced Optical Materials, 2014. **2**(10): p. 945.

158. Zalden, P.E., *Phase-Change Materials: Structure, vibrational states and thermodynamics of crystallization.* RWTH Aachen University, PhD thesis, 2012.

159. Wuttig, M. and M. Salinga, *PHASE-CHANGE MATERIALS Fast transformers.* Nature Materials, 2012. **11**(4): p. 270.

160. Shportko, K., et al., *Resonant bonding in crystalline phase-change materials.* Nat Mater, 2008. **7**(8): p. 653.

161. Wuttig, M. and N. Yamada, *Phase-change materials for rewriteable data storage.* Nat Mater, 2007. **6**(11): p. 824.

162. Cao, T., C. Wei, and L. Mao, *Ultrafast tunable chirped phase-change metamaterial with a low power.* Opt Express, 2015. **23**(4): p. 4092.

163. Cao, T., et al., *Fast tuning of Fano resonance in metal/phase-change materials/metal metamaterials.* Optical Materials Express, 2014. **4**(9): p. 1775.

164. Cao, T., et al., *Fast tuning of double Fano resonance using a phase-change metamaterial under low power intensity.* Sci Rep, 2014. **4**: p. 4463.

165. Chen, Y.G., et al., *Engineering the Phase Front of Light with Phase-Change Material Based Planar lenses.* Scientific Reports, 2015. **5**: p. 8660.

166. Xu, T., et al., *Subwavelength imaging by metallic slab lens with nanoslits.* Applied Physics Letters, 2007. **91**(20): p. 201501.

167. Xu, T., et al., *Plasmonic beam deflector.* Optics Express, 2008. **16**(7): p. 4753.

168. Choe, J.-H., et al., *Slot antenna as a bound charge oscillator.* Optics Express, 2012. **20**(6): p. 6521.

169. Cavalleri, A., et al., *Femtosecond structural dynamics in VO2 during an ultrafast solid-solid phase transition.* Physical Review Letters, 2001. **87**(23): p. 1187.

170. Duan, H., et al., *Nanoplasmonics: Classical down to the Nanometer Scale.* Nano Letters, 2012. **12**(3): p. 1683.

171. Chu, M.-W., et al., *Probing Bright and Dark Surface-Plasmon Modes in Individual and Coupled Noble Metal Nanoparticles Using an Electron Beam.* Nano Letters, 2009. **9**(1): p. 399.

172. Wen, F., et al., *Plasmon Transmutation: Inducing New Modes in Nanoclusters by Adding Dielectric Nanoparticles.* Nano Letters, 2012. **12**(9): p. 5020.

173. Schmidt, F.-P., et al., *Dark Plasmonic Breathing Modes in Silver Nanodisks.* Nano Letters, 2012. **12**(11): p. 5780.

174. Hao, F., et al., *Shedding light on dark plasmons in gold nanorings.* Chemical Physics Letters, 2008. **458**(4–6): p. 262.

175. Hao, F., et al., *Symmetry Breaking in Plasmonic Nanocavities: Subradiant LSPR Sensing and a Tunable Fano Resonance.* Nano Letters, 2008. **8**(11): p. 3983.

176. Sonnefraud, Y., et al., *Experimental Realization of Subradiant, Superradiant, and Fano Resonances in Ring/Disk Plasmonic Nanocavities.* ACS Nano, 2010. **4**(3): p. 1664.

177. Dong, Z.-G., et al., *Role of asymmetric environment on the dark mode excitation in metamaterial analogue of electromagnetically-induced transparency.* Optics Express, 2010. **18**(21): p. 22412.

178. Rahmani, M., et al., *Subgroup Decomposition of Plasmonic Resonances in Hybrid Oligomers: Modeling the Resonance Lineshape.* Nano Letters, 2012. **12**(4): p. 2101.

179. Alonso-Gonzalez, P., et al., *Real-Space Mapping of Fano Interference in Plasmonic Metamolecules.* Nano Letters, 2011. **11**(9): p. 3922.

180. Fan, J.A., et al., *DNA-Enabled Self-Assembly of Plasmonic Nanoclusters.* Nano Letters, 2011. **11**(11): p. 4859.
181. Fan, J.A., et al., *Fano-like Interference in Self-Assembled Plasmonic Quadrumer Clusters.* Nano Letters, 2010. **10**(11): p. 4680.
182. Zhao, J., et al., *Large-Area Low-Cost Plasmonic Nanostructures in the NIR for Fano Resonant Sensing.* Advanced Materials, 2012. **24**(35): p. OP247.
183. Zhang, S., et al., *Plasmon-Induced Transparency in Metamaterials.* Physical Review Letters, 2008. **101**(4): p. 047401.
184. Verellen, N., et al., *Fano Resonances in Individual Coherent Plasmonic Nanocavities.* Nano Letters, 2009. **9**(4): p. 1663.
185. Wu, C., et al., *Fano-resonant asymmetric metamaterials for ultrasensitive spectroscopy and identification of molecular monolayers.* Nat Mater, 2012. **11**(1): p. 69.
186. Artar, A., A.A. Yanik, and H. Altug, *Multispectral Plasmon Induced Transparency in Coupled Meta-Atoms.* Nano Letters, 2011. **11**(4): p. 1685.
187. Taubert, R., et al., *Classical Analog of Electromagnetically Induced Absorption in Plasmonics.* Nano Letters, 2012. **12**(3): p. 1367.
188. Liu, N., et al., *Plasmonic analogue of electromagnetically induced transparency at the Drude damping limit.* Nat Mater, 2009. **8**(9): p. 758.
189. Abasahl, B., et al., *Coupling Strength Can Control the Polarization Twist of a Plasmonic Antenna.* Nano Letters, 2013. **13**(9): p. 4575.
190. Ye, F., M.J. Burns, and M.J. Naughton, *Plasmonic Halos—Optical Surface Plasmon Drumhead Modes.* Nano Letters, 2013. **13**(2): p. 519.
191. Kariniemi, M., et al., *Plasma-Enhanced Atomic Layer Deposition of Silver Thin Films.* Chemistry of Materials, 2011. **23**(11): p. 2901.
192. Niskanen, A., et al., *Radical-Enhanced Atomic Layer Deposition of Silver Thin Films Using Phosphine-Adducted Silver Carboxylates.* Chemical Vapor Deposition, 2007. **13**(8): p. 408.
193. Wang, K., et al., *Trapping and rotating nanoparticles using a plasmonic nano-tweezer with an integrated heat sink.* Nat Commun, 2011. **2**: p. 469.
194. Kinkhabwala, A., et al., *Large single-molecule fluorescence enhancements produced by a bowtie nanoantenna.* Nat Photon, 2009. **3**(11): p. 654.
195. Okamoto, K., et al., *Surface-plasmon-enhanced light emitters based on InGaN quantum wells.* Nat Mater, 2004. **3**(9): p. 601.
196. Lin, H.Y., et al., *Carrier transfer induced photoluminescence change in metal-semiconductor core-shell nanostructures.* Applied Physics Letters, 2006. **88**(16): p. 161911.
197. Jung, D.-R., et al., *Photoluminescence enhancement in CdS nanoparticles by surface-plasmon resonance.* Applied Physics Letters, 2011. **99**(4): p. 041906.
198. Hailong Hu, H.D., Joel K. W. Yang and Ze Xiang Shen, *Plasmon-Modulated Photoluminescence of Individual Gold Nanostructures.* ACS Nano, 2012. **6**(11): p. 10147.
199. N. E. Hecker, R.A.H., N. Sawaki, T. Maier, and G. Strasser, *Surface plasmon-enhanced photoluminescence from a single quantum well.* Applied Physics Express, 1999. **75**(11): p. 1577.
200. Kazunari Matsuda, Y.I., and Yoshihiko Kanemitsu, *Photoluminescence enhancement and quenching of single Cd Se /Zn S nanocrystals on metal surfaces dominated by plasmon resonant energy transfer.* Applied Physics Letters, 2008. **92**: p. 211911
201. Pierre Viste, J.r.P., Rodolphe Jaffiol, Alexandre Vial, Pierre Michel Adam, and Pascal Royer, *Enhancement and Quenching Regimes in Metal--Semiconductor Hybrid Optical Nanosources.* ACS Nano, 2010. **4**(2): p. 759.

202. D. Zhang, H.U., P. Wang, C. Park, R. Murakami, S. Yang and X. Song, *Photoluminescence modulation of ZnO via coupling with the surface plasmon resonance of gold nanoparticles.* Applied Physics Letters, 2013. **103**(9): p. 093114.
203. Hwang, S.W., et al., *Plasmon-Enhanced Ultraviolet Photoluminescence from Hybrid Structures of Graphene/ZnO Films.* Physical Review Letters, 2010. **105**(12): p. 127403.
204. Jung, D.-R., et al., *Surface-plasmon-enhanced photoluminescence of CdS nanoparticles with Au/SiO2 nanocomposites.* Materials Research Bulletin, 2012. **47**(2): p. 453.
205. Kim, J.I., et al., *Surface–plasmon-coupled photoluminescence from CdS nanoparticles with Au films.* Solid State Communications, 2012. **152**(18): p. 1767.
206. Zhou, K., et al., *Demonstration of Photoluminescence and Metal-Enhanced Fluorescence of Exfoliated MoS2.* ChemPhysChem, 2012. **13**(3): p. 699.
207. Butun, S., S. Tongay, and K. Aydin, *Enhanced Light Emission from Large-Area Monolayer MoS2 Using Plasmonic Nanodisc Arrays.* Nano Letters, 2015. **15**(4): p. 2700.
208. Goodfellow, K.M., et al., *Integrated nanophotonics based on nanowire plasmons and atomically thin material.* Optica, 2014. **1**(3): p. 149.
209. Lee, H.S., et al., *Efficient Exciton–Plasmon Conversion in Ag Nanowire/Monolayer MoS2 Hybrids: Direct Imaging and Quantitative Estimation of Plasmon Coupling and Propagation.* Advanced Optical Materials, 2015. **3**(7): p. 943.
210. Najmaei, S., et al., *Plasmonic Pumping of Excitonic Photoluminescence in Hybrid MoS2–Au Nanostructures.* ACS Nano, 2014. **8**(12): p. 12682.
211. Sobhani, A., et al., *Enhancing the photocurrent and photoluminescence of single crystal monolayer MoS2 with resonant plasmonic nanoshells.* Applied Physics Letters, 2014. **104**(3): p. 031112.
212. Geim, A.K., *Graphene: Status and Prospects.* Science, 2009. **324**(5934): p. 1530.
213. Mak, K.F., et al., *Atomically Thin MoS2: A New Direct-Gap Semiconductor.* Physical Review Letters, 2010. **105**(13): p. 136805.
214. Splendiani, A., et al., *Emerging Photoluminescence in Monolayer MoS2.* Nano Letters, 2010. **10**(4): p. 1271.
215. Tongay, S., et al., *Thermally Driven Crossover from Indirect toward Direct Bandgap in 2D Semiconductors: MoSe2 versus MoS2.* Nano Letters, 2012. **12**(11): p. 5576.
216. Tonndorf, P., et al., *Photoluminescence emission and Raman response of monolayer MoS2, MoSe2, and WSe2.* Optics Express, 2013. **21**(4): p. 4908.
217. Zeng, H., et al., *Optical signature of symmetry variations and spin-valley coupling in atomically thin tungsten dichalcogenides.* Scientific Reports, 2013. **3**: p. 1608.
218. Eda, G. and S.A. Maier, *Two-dimensional crystals: managing light for optoelectronics.* Acs Nano, 2013. **7**(7): p. 5660.
219. Akselrod, G.M., et al., *Leveraging Nanocavity Harmonics for Control of Optical Processes in 2D Semiconductors.* Nano Letters, 2015. **15**(5): p. 3578.
220. J. Miao , W.H., Y. Jing , W. Luo , L. Liao , A. Pan , S. Wu , J. Cheng , X. Chen , and W. Lu, *Surface Plasmon-Enhanced Photodetection in Few Layer MoS2 Phototransistors with Au Nanostructure Arrays.* Small, 2015. **11**(20): p. 2392.
221. O. Salehzadeh, N.H.T., X. Liu, I. Shih, and Z. Mi, *Exciton Kinetics, Quantum Efficiency, and Efficiency Droop of Monolayer MoS2 Light-Emitting Devices.* Nano Lett, 2014. **14**(7): p. 4125.
222. A. Castellanos-Gomez , R.R., E. Cappelluti, M. Buscema, F. Guinea, H. S. J. van der Zant, and G. A. Steele, *Local Strain Engineering in Atomically Thin MoS2.* Nano Lett, 2013. **13**(11): p. 5361.

223. Lee, H.S., et al., *Selective amplification of primary exciton in monolayer MoS2.* Physics, 2015.

224. W. Zhao, Z.G., L. Chu, M. Toh, C. Kloc, P. H. Tan, and G. Eda, *Evolution of Electronic Structure in Atomically Thin Sheets of WS2 and WSe2.* ACS Nano, 2013. **7**(1): p. 791.

225. Ross, J.S., et al., *Electrically tunable excitonic light-emitting diodes based on monolayer WSe2 p-n junctions.* Nature Nanotechnology, 2014. **9**(4): p. 268.

226. Yan, T., et al., *Photoluminescence properties and exciton dynamics in monolayer WSe 2.* Applied Physics Letters, 2014. **105**(10): p. 101901.

227. Wu, S., et al., *Monolayer semiconductor nanocavity lasers with ultralow thresholds.* Nature, 2015. **520**(7545): p. 141.

228. Jones, A.M., et al., *Optical generation of excitonic valley coherence in monolayer WSe2.* Nature Nanotechnology, 2013. **8**(9): p. 634.

229. Wu, S., et al., *Ultra-Low Threshold Monolayer Semiconductor Nanocavity Lasers.* Physics, 2015.

230. Chen, C.H., et al., *Hole mobility enhancement and p -doping in monolayer WSe2 by gold decoration.* 2d Materials, 2014. **1**(3).

231. Dong, Z., et al., *Second-Harmonic Generation from Sub-5 nm Gaps by Directed Self-Assembly of Nanoparticles onto Template-Stripped Gold Substrates.* Nano Letters, 2015. **15**(9): p. 5976.

232. Heavens, O.S., *Handbook of Optical Constants of Solids II*. 1985: Academic Press. 189.

List of Journal Publications

Yinghong Gu, Fei Qin, Joal K. W. Yang, Swee Ping Yeo and Cheng-Wei Qiu, *Direct Excitation of Dark Plasmonic Resonances under Visible Light at Normal Incidence*, Nanoscale, 2014, **6**: p.2106.

Yinghong Gu, Lei Zhang, Joal K. W. Yang, Swee Ping Yeo and Cheng-Wei Qiu, *Color generation via Subwavelength Plasmonic Nanostructures*, Nanoscale, 2015, **7**: p. 6409.

Dacheng Wang, **Yinghong Gu**, Yandong Gong, Cheng-Wei Qiu and Minghui Hong, *Au Ultrathin Terahertz Quarter-wave Plate Using Planar Babinet-Inverted Metasurface*, Opt. Express, 2015, **23**: p. 11114.

(As the 2nd author, I simulated the structure for the design of the device. Dacheng did the experiment and measurement.)

Dacheng Wang, Lingchao Zhang, **Yinghong Gu**, M. Q. Mehmood, Yandong Gong, Amar Srivastava, Linke Jian, T. Venkatesan, Cheng-Wei Qiu and Minghui Hong, *Switchable Ultrathin Quarter-wave Plate in Terahertz Using Active Phase-change Metasurface*, Sci Rep., 2015, **5**: p. 15020.

(As the 3rd author, I simulated the structure for the design of the device. Dacheng and Lingchao did the experiment and measurement.)

Zhuo Wang, Zhaogang Dong, **Yinghong Gu**, Yung-Huang Chang, Lei Zhang, Lain-Jong Li, Weijie Zhao, Goki Eda, Wenjing Zhang, Gustavo Grinblat**,** Stefan A. Maier, Joel K. W. Yang, Cheng-Wei Qiu and Andrew T. S. Wee, *Giant Photoluminescence Enhancement in WSe_2-Gold Plasmonic Hybrid Structures*, Nat. Commun., accepted.

(As the 3rd author,I simulated the gold nanostructure for enhancement of absorption and calculated the Purcell factor, and explained the PL enhancement in excitation and emission process. Zhuo and Zhaogang did the experiment and measurement.)

Yinghong Gu, Rui Feng, Joal K. W. Yang, Haibin Zhu, Swee Ping Yeo, Zhixiang Tang and Cheng-Wei Qiu, *Actively reconfigurable Gold-Ge2Sb2Te5 hybrid metasuface: Ultrathin multi-wavelength quarter wave plate*, Nanoscale, submited.

Zhaogang Dong*, **Yinghong Gu***, Cheng-wei Qiu and Joel K. W. Yang, *Vertical Fabry-Perot Resonance in 10-nm Silicon Nanostructures for Color Display*, in progress. (*Contributed equally to 1st author, I simulated the structure for the color and built up the TMM to theoretically explain and simplify the problem. Zhaogang did the experiment and measurement.)